

Path Optimization of a Pumping Kite System

M. S. Jerez Venegas

Technische Universiteit Delft



PATH OPTIMIZATION OF A PUMPING KITE SYSTEM

by

M. S. Jerez Venegas

in partial fulfillment of the requirements for the degree of

Master of Science

in Aerospace Engineering

at the Delft University of Technology

&

Master of Science

in Engineering in Wind Energy

at the Technical University of Denmark

within the **European Wind Energy Master - EWEM**

Rotor Design Track (Aerodynamics)

Faculty of Aerospace Engineering Delft · University of Technology

Department of Wind Energy · Technical University of Denmark

Supervisors: Dr.-Ing. R. Schmehl

Dr. M. Gaunaa

Committee: Dr.ir. E.R.G. Quaeghebeur

P. Faggiani

SUMMARY

Nowadays, wind energy is cost-competitive with traditional fossil fuels. Better technologies, policies, and access to finance are some of the reasons that have decreased the overall costs of wind turbines and wind farms. However, traditional wind turbines cannot compete with other generation systems if the wind resource close to the ground is scarce, as in inland countries. Airborne wind energy aims to reduce costs by harvesting winds at high altitudes. The concept uses two fundamental premises: i) airborne wind has more energy than turbines close to the surface and ii) the outer third of the wind turbine blades is responsible for more than half the power produced by a wind turbine. The pumping kite concept investigated at the Delft University of Technology (TU Delft) is based on leading edge inflatable (LEI) kites that divide a generation cycle into three phases: traction, retraction and transition. During traction phase the kite drives a generator, producing electricity. When the kite line is entirely reeled out, the retraction phase starts, using a fraction of the harvested power to reel in the cable. Finally, the transition phase locates the wing at its original position, where the cycle can start again. This research project aimed to optimise the trajectory flown by the kite such as to increase the cost-competitiveness of the system.

To determine the optimal trajectory, the complete system was simulated using an aerodynamic model, a tether model, a kite controller and a path planning strategy. The quasi-steady model was chosen for the aerodynamic modelling due to its low computational requirements. A validation of the model was conducted, demonstrating that if by providing the trajectory, tether ground force and aerodynamic coefficients, the model can predict the velocities, aerodynamic forces and the power production of the system. Three kite line models are presented: the high fidelity model, the low fidelity model and the lumped model. It was determined that the discretized low fidelity model is the most suitable for the optimisation since it provides accurate results with low computational costs. A hierarchical control was used to guide the kite. The controller was divided into three main loops that calculate first the desired heading, second the required course rate, and finally the steering input. Three waypoints are used to describe the whole trajectory, two waypoints are used for the traction phase, and one waypoint is used for the retraction. Moreover, a new description of the figure of eight was provided, using the heading and the azimuth position of the kite.

Using the developed system model, the average power during traction and the average power per cycle was mapped. It was determined that there is an area that maximises the power production during reel out and the cycle power during reel in. This area is determined by the wind speed, the shape of the figure, and the reel in/out force. However, it is not possible to know a priori the optimal parameters since the exact wind conditions at the kite are unknown. Moreover, it was proven that narrower figures and down loops during traction phase present several advantages, such as fewer power fluctuations and higher manoeuvrability. Thus, the steering capabilities of the system determine the minimum size of the traction trajectory. Hence, the reel in/out force, the centre of the figure of eight and the retraction waypoint were used to develop an online optimizer that maximises the average power of the cycle.

Finally, the online optimizer was used in a case study, comparing its results to a flight test. The optimal trajectory led to a 100% increase in cycle power and a 16% increase in the average traction power. The final increase in the power per cycle was a combination of a faster retraction phase and a higher power production during reel out.

ACKNOWLEDGMENTS

I wouldn't have been able to complete this thesis without the help of so many people. I would like to first thank my supervisors: Roland Schmehl and Mac Gaunaa. Your patience and guidance made this project possible. I would also like to thank all my colleagues from Kitepower: Johannes, Joep, Pietro, Bert, Bruno, Anna, Bart, David, Roland, Roger, Marius, Marc, Marcello, and Astrid. From lengthy discussions to a good laugh during a coffee break, I would not have been able to do this without you. I hope this thesis may help you to one day say "this house is powered by Kitepower". I would also like to thank the PhD candidates: Sebastian, and Mikko. In the most stressful moments, you were always there to give me a hand.

To the room 6.08 and my friends: Bas, Jo, Maarten, Pranav, Matteo, Ivan, Adri, Greeshma, Clara, Roberto, Julia, and Luca. I can't imagine a better place to have written my thesis.

To Bizetstraat 55 and Mahlerstraat 26. You didn't give me a house but a home. I can't thank you enough for all the jokes, the dinners, the adventures, and time we spent together. Special thanks to Lucia and Philippa for all the morning coffees, for proofreading my thesis, and the encouragement in the final days.

To my friends and colleagues from the EWEM program and DTU Wind Energy, especially to Nikos, Qasim, Mariana, Niels, Irene, Luis, Constantin, Marijn, Leo, Mareen, and Roberto. The Master wouldn't have been half as fun without you.

Finally, to my parents, sisters, and family. I wouldn't have gotten this far without your advice, love, and support.

To all of you, from the bottom of my heart, thank you.

*Marcos S. Jerez Venegas
Delft, July 2017*

CONTENTS

List of Figures	ix
List of Tables	xiii
1 Introduction	1
2 Literature Study	3
2.1 Renewable Energy Market	3
2.2 Airborne Wind Energy	4
2.3 Pumping Kite	6
2.4 Computational Models	8
2.4.1 Kite Models	8
2.4.2 Tether Models.	9
2.5 Control	10
2.6 Path Optimization	12
2.7 Conclusions, Research Question and Methodology	13
3 System Modelling	15
3.1 Atmospheric Modeling.	15
3.2 Reference Systems	15
3.3 Tether Models	16
3.3.1 High Fidelity Tether Model.	17
3.3.2 Low Fidelity Tether Model	19
3.3.3 Lumped Tether	20
3.4 System Modeling	21
3.4.1 Extended One-Point Model	23
3.4.2 Quasi-Steady Model	23
3.4.3 Iterative solution with variable AoA	25
3.5 Chapter Conclusions.	26
4 Quasi-Steady Model Validation	27
4.1 Flight Test.	27
4.2 Data Processing	28
4.3 Experiment vs Quasi Steady Model	30

4.4	Chapter Conclusions.	37
5	Control and Path Planning	39
5.1	Control Strategies	39
5.1.1	Turn Rate Law.	39
5.1.2	Hierarchy Control	40
5.2	Path Planning.	42
5.2.1	Phase Start	42
5.2.2	Transition Characteristics	43
5.2.3	Figure of Eight	44
5.3	Kite Properties and Simulation Results	45
5.4	Chapter Conclusions.	51
6	Path Optimization	53
6.1	Traction Phase Mapping.	53
6.1.1	Unidirectional Traction Mapping	54
6.1.2	Lissajous Trajectory Power Mapping	54
6.1.3	Lissajous Trajectory Loop Analysis	56
6.1.4	Traction Force Optimization.	62
6.1.5	Conclusions of the Offline Traction Mapping	62
6.2	Retraction Phase Mapping.	63
6.2.1	Unidirectional Retraction Mapping.	63
6.2.2	Retraction Force Dependence	64
6.2.3	Retraction Mapping	64
6.2.4	Conclusions of the Offline Retraction Mapping	66
6.3	Online Optimizer.	67
6.3.1	Traction Optimization	67
6.3.2	Retraction Optimization	69
6.3.3	Final Optimization Algorithm	70
6.4	Chapter Conclusions.	73
7	Case Study	75
7.1	Results.	75
7.2	Chapter Conclusions.	80
8	Conclusions and Recommendations	81
A	Optimization Parameters	85
	Bibliography	87

LIST OF FIGURES

2.1	Global primary energy consumption by fuel in 2015 [7]	3
2.2	Global levelized cost of energy from different sources. PV solar is photovoltaic and CSP is concentrated solar power [30]	4
2.3	Horizontal axis wind turbine and airborne wind energy comparison [15]	5
2.4	Airborne wind energy systems and concepts	5
2.5	Wind window concept for an AWE system	6
2.6	Working principle of the pumping kite power system [49]	6
2.7	2D representation of a pumping cycle, the points P1, P2, and P3 show the limits of each cycle. Adapted from [49]	7
2.8	KCU and kite connections for the TUDelft AWE system [15]	7
2.9	System components, sensor locations (circles) and wireless connections [49]	7
2.10	Different kite system models. From left to right multi-body, multi-plate and four particle system, adapted from [22, 25, 53]	8
2.11	Heading PID controller with NDI, adapted from [21]	10
2.12	Hierarchy controller proposed by [20]	11
2.13	Pumping trajectory with five loops per cycle, adapted from [26]	12
3.1	Spherical and ECEF reference system, adapted from [21]	16
3.2	Tether nodes, forces and velocities	17
3.3	a) Apparent wind speed along the tether at t=20s during retraction phase, b) Tether drag during a cycle. Both cases show the discretized and approximated cases.	19
3.4	Kite and tether drag direction	21
4.1	Sketch of the installed apparent wind speed sensor, adapted from [43]	27
4.2	Dynamic pressure before and after filtering	28
4.3	a) Lift coefficient and b) drag coefficient for the kite, adapted from [21]	30
4.4	a) Trajectory flown and b) tether length during the 7th cycle. The gray area shows the transition phase.	31
4.5	a) Side and b) front views of the trajectory	31
4.6	a) Tether force at the ground, b) relative depower and c) density at the kite	32
4.7	a) Lift coefficient, b) drag coefficient and c) inflow angle	33
4.8	Components of the kite ground and apparent speed w.r.t the ground station in spherical coordinates	34

4.9	a) Kite ground speed, b) apparent wind speed and c) mechanical power	35
4.10	a) Kite ground speed, b) apparent wind speed and c) mechanical power for the case 2*	36
4.11	Apparent wind speed in a) radial and b) tangential direction during the cycle for case 2*	37
5.1	Turning rate law sketch	40
5.2	Hierarchical kite course control, adapted from [32]	41
5.3	Path planning of the pumping kite	43
5.4	Force and reel speed at v_R^w a) 6 m/s and b) 8 m/s. The transition phase is shown in gray.	43
5.5	a) Waypoints and description of the figure of eight and b) problems of the simple description	44
5.6	a) Down and b) up loop description for the figure of eight	44
5.7	Sketch of the final model	45
5.8	Trajectory of the kite	46
5.9	a) Tether length vs time, b) X vs Z, and c) elevation vs time. Transition phase in gray	47
5.10	a) Apparent, b) tangential and c) reeling velocity over time	48
5.11	a) Force, b) mechanical power and c) angle of attack over time	49
5.12	a) Lift to Drag, b) steering input and c) depower input over time	50
6.1	Instantaneous power production at a) 250 m and b) 400 m , the triangle shows the position of maximum power	54
6.2	Quasi steady traction phase with Lissajous trajectory	55
6.3	Traction phase average power using the Lissajous figure, $(A_\beta, A_\phi) = (3.5^\circ, 20^\circ)$	55
6.4	Variation of the average power along power centre in a) elevation and b) azimuth	56
6.5	Normalized average power for $A_\phi =$ a) 20, b) 15, c) 10, and d) 5°	57
6.6	Variation of the average power along power centre in a) elevation and b) azimuth for different A_ϕ	57
6.7	Normalized average power for $A_\beta =$ a) 10, b) 7.5, c) 5, and d) 3.5°	58
6.8	Variation of the average power along power centre in a) elevation and b) azimuth for different A_β	59
6.9	a) Elevation and b) angle of attack for up and down loops	59
6.10	a) Apparent wind speed and b) reel speed for up and down loops	60
6.11	Mechanical power for up and down loops	60
6.12	Constant azimuth angle and length for the traction trajectory	61
6.13	Normalized average power for a constant a) width and b) angle	61
6.14	Variation of the average power along power centre in a) elevation and b) azimuth for different constant angle and width. $A_\beta = 3.5^\circ$ for all cases	62
6.15	Normalized mean mechanical power over a) force and b) reel out speed. The dashed line is the optimal solution from eq. (6.3)	62
6.16	Power required for retraction at a) 180 and b) 90° at 400 m (left)	63

6.17	Normalized power per cycle for three reference speed. The retraction has been done from the zenith	64
6.18	Retraction trajectory at different way-points $P_R = (\beta_R, \phi_R)$	65
6.19	Normalized average power per cycle for different retraction way-points P_R . The reference wind speed is a) 8, b) 9 and c) 10 m/s	66
6.20	Traction to retraction path, the centered path is favourable for retraction	66
6.21	Retraction waypoint sketch	69
7.1	Trajectory of the optimized, and reference cases	76
7.2	a) Azimuth centre, b) reel out force, and c) elevation centre over loop number	77
7.3	a) Reel in force, b) retraction azimuth and c) retraction elevation over the cycle number	78
7.4	a) Instantaneous power over time, b) mean mechanical power over cycle number, and c) average power per cycle over cycle number. The transition phase is shown as a gray area in a). Short spaced dashes: optimized trajectory. Long space dashes: flight test.	79

LIST OF TABLES

4.1	Kite, KCU and sensor properties	28
4.2	Tether Properties	28
4.3	Wind profile during the flight test	30
5.1	Start, depower input and initial way-point for each phase	43
5.2	Description of the figure of eight	45
5.3	Environmental Conditions	45
5.4	Kite Properties	45
5.5	Tether Properties	45
5.6	KCU Properties	46
5.7	Control Properties	46
5.8	Mechanical power, duration and energy produced during the each phase	50
6.1	Flight conditions for the traction and retraction mapping	53
7.1	Wind profile test case	75
7.2	Flight parameters for the flight test and initial conditions for the optimization	75
7.3	Final parameters from the optimization and mapping	79
A.1	Wind profile test case	85

NOMENCLATURE

Abbreviations

ABL	Atmospheric boundary layer
AWE	Airborne wind energy
BEM	Blade element momentum
CFD	Computational fluid dynamics
FEM	Finite element model
GPS	Global position system
IMU	Inertial measurement units
KCU	Kite control unit
LCoE	Levelized Cost of Energy
LEI	Leading edge inflatable
NMPC	Non-linear model predictive controller
PID	Proportionalintegralderivative
SEC	Small earth centred
toe	Tonnes of oil equivalent
WRF	Weather research and forecasting

Subscripts

\perp	Perpendicular component
ϕ	Azimuth direction
θ	Polar direction
r	Radial direction
t	Tangential

Greek Symbols

α	Effective angle of attack
α_0	Geometric angle of attack
α_d	Depowering angle of attack

β	Elevation angle in a spherical coordinate system
β_{set}	Desired elevation angle
χ	Course angle
χ_{set}	Desired heading angle
$\Delta\alpha$	Inflow angle of attack
$\Delta\alpha_{pitch}$	Inflow angle component in the pitch plane
$\Delta\alpha_{yaw}$	Inflow angle component in the yaw plane
$\dot{\chi}$	Turn rate
$\dot{\psi}_{set}$	Set turning rate for traction phase
κ	Kinematic ratio
λ	Tangential velocity factor
ϕ	Azimuth position in a spherical coordinate system
ϕ_w	Wind direction
$\phi_{+,-}$	Azimuth width of the P_+ and P_- points
ϕ_{set}	Desired azimuth angle
ϕ_{turn}	Turning angle correction
Ψ	Heading angle
ρ	Density
θ	Polar angle in a spherical coordinate system
Θ_R	Path description during retraction
Θ_T	Path description during traction

Latin Symbols

β_c	Lissajous' curve elevation centre
$\Delta\dot{r}$	Difference between the optimal and average reel out speed
$\Delta\dot{r}_{min}$	Traction force optimization criterion
$\Delta\bar{P}$	Power difference between the left and right of the figure
$\Delta\bar{P}_{min}$	Azimuth optimization criterion
Δt	Time step
Δp	Dynamic pressure
\dot{r}	Tether reel out/in speed

\bar{P}_{cycle}	Average power per cycle
\bar{r}	Average reel out speed
\bar{r}_{opt}	Optimal reel out speed
\bar{P}_{Left}	Power at the left side of the figure
\bar{P}_{Right}	Power at the right side of the figure
ϕ_c	Lissajous' curve azimuth centre
σ_0	Mass per length of the non-deformed tether
σ_i	Mass per length of the deformed tether element
\vec{a}	acceleration
\vec{e}_0	Perpendicular direction to $\vec{e}_{k,app}$ and \vec{e}_r
\vec{e}_D	Drag direction
\vec{e}_L	Lift direction
$\vec{e}_{k,app}$	Kite apparent speed direction
\vec{p}	Position vector
\vec{v}	Velocity vector
A_β	Lissajous' curve elevation angle
A_ϕ	Lissajous' curve azimuth angle
c_0	Damping constant of the non-deformed tether element
C_D	Drag coefficient
c_i	Damping constant of the deformed tether
C_L	Lift coefficient
C_R	Resultant coefficient
d	Diameter
f	Reel-out factor
G	Lift-over-Drag coefficient
G_{calc}	Lift-over-Drag coefficient
k_0	Elastic constant of the non-deformed tether element
k_i	Elastic constant of the deformed tether
$K_{d,s}$	Depower effect on the steering
l_s	Length of each undeformed tether element

P_R	Retraction way-point
q_t	Distributed mass in radial direction
r	Radial position in a spherical coordinate system
S	Projected area of the kite
S_{side}/S	Relative side projected area of the kite
S_{tot}	Total area of the kite
u_d	Depower input
u'_d	Relative depower input
$u_{s,0}$	Asymmetrical bridal consideration for steering
u_s	Steering input
u'_s	Relative steering input
v^w	Wind speed
v_R^w	Reference wind speed
v_k	Kite speed
v_w	Wind speed
V_{pitch}	Voltage of the pitch direction vane
V_{yaw}	Voltage of the yaw direction vane
w	Angle of attack due to sagging of the tether
x	X position in a Cartesian coordinate system
y	Y position in a Cartesian coordinate system
z	Z position in a Cartesian coordinate system, height
z_0	Roughness length
z_R	Reference height
AoA	Angle of Attack
g	Gravitational constant
H	Altitude
L	Length of the total undeformed tether
lat	Latitude
lon	Longitude
m	Mass

N Number of discretized tether elements

$P_{+,-}$ Way points for traction phase

Superscripts

w Wind

aer Aerodynamic

app Apparent

c Damping

D Drag

e Elastic,Effective

ext External

g Gravitational

GS Ground station

k Kite

L Lift

s Steering

t Tether

1

INTRODUCTION

In 2015 renewable energies generated 364.9 toe¹, increasing 15.6% with respect to the previous year [7]. Better and more reliable technologies, dedicated policy initiatives, better access to finance, energy security and environmental concerns, growing demand for energy in developing and emerging economies, and the need for access to modern energy have significantly reduced the costs for renewable energies [45]. In particular, wind energy is currently able to compete with traditional fossil fuels. The cost-competitiveness of wind harvesting systems has decreased by capturing steadier, more constant and stronger winds located far from the ground, increasing the energy production of the wind farms. However, traditional horizontal axis wind turbines are far from ideal: i) the cost of the turbine rapidly increases with size; ii) the wind resource at low heights is mainly located offshore or at the coast, restricting its use in inland countries; and iii) turbines require an extensive amount of space and affect the landscape [23, 37]. These problems do not mean that wind harvesting systems should not be adopted, but that alternative technologies are required to compensate their limitations and expand the locations where the wind is an economically viable solution to energy needs.

Airborne wind energy aims to reduce costs by harvesting winds at high altitudes. The concept is based on two fundamental premises: i) airborne wind has more energy than turbines close to the surface and ii) the outer third of the blades is responsible for more than half the power produced by a wind turbine. The tower, foundation, hub, and large portion of the blades are only used for structural integrity, yet they account for up to 40% of the cost of a wind turbine. Furthermore, it is widely accepted that only a fraction of the available wind power far from the ground could supply enough energy for the entire planet [31, 40]. In 1980, Miles Lloyd proposed the use of tethered wings as generators, estimating that an aircraft of 500 m² could produce 5MW. Since then, many different airborne systems have been proposed. The pumping kite concept investigated at the Delft University of Technology (TU Delft) is based on leading edge inflatable (LEI) kites that divide a generation cycle into three phases: traction, retraction and transition. During traction phase the kite drives a generator, producing electricity. When the kite line is completely reeled out, the retraction phase starts, using a fraction of the harvested power to reel in the cable. Finally, the transition phase locates the wing at its original position, where the cycle can start again.

To increase the cost-competitiveness of the system, this research project aims to optimise the trajectory flown by the kite during the pumping cycle. The project has been developed in collaboration with the Technical University of Denmark, TU Delft and the company Kitepower. The report

¹tonnes of oil equivalent

is organised as follows: Chapter two presents the literature study, describing the current state of the art for i) control strategies, ii) computational models, iii) optimisation approach and iv) the research questions and objectives. Chapter three presents the environmental, tether and aerodynamic models. Chapter four presents a validation of the quasi-steady model. Chapter five presents the control strategy and path planning of the kite. v) Chapter six presents the offline mapping of the trajectory and the online optimizer derived from it. vi) Chapter seven presents a case study of the final optimizer. Finally, chapter eight presents the conclusions and recommendations for further research.

2

LITERATURE STUDY

The present chapter intends to introduce the motivation for the research. The chapter starts briefly depicting the current renewable market situation, specifically the current costs of wind energy. Then, the concept of airborne wind is introduced, along with the type of generation that will be considered, i.e. the pumping kite. A wide range of high to low fidelity models are then presented for the kite and the tether, explaining its advantages and drawbacks. The control of the kite is also discussed, presenting the most traditional and relevant control strategies that can be used for the system. The offline and online path optimisation methods, which the thesis aims for, that different authors have used to maximise the energy production are presented and discussed in Section 2.6. The chapter finishes presenting the conclusions, research questions, objectives and methodology that will be followed along the project.

2.1. RENEWABLE ENERGY MARKET

In 2015 renewable energies generated a total of 364.9 toe¹, increasing 15.6% with respect to the previous year [7]. Nevertheless, this represented only 3% of the total electric generation worldwide; as it can be observed in Fig. 2.1. Fossil fuels, like oil and coal, are, by far, the most widely used resource to produce energy, accounting for over 50% of the total.

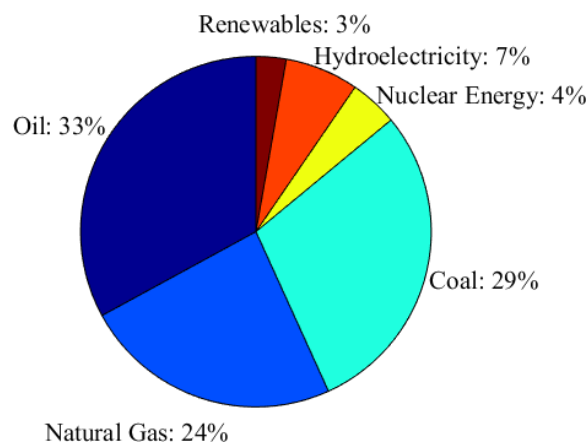


Figure 2.1: Global primary energy consumption by fuel in 2015 [7]

¹without considering hydro- nor nuclear power

In recent years the costs of renewable generators have decreased considerably, becoming substantially more competitive than they were a few years ago, with even lower prices than fossil fuels [45]. To compare different generation sources the levelized cost of electricity (LCoE) is used, given by

$$LCoE = \frac{\text{Total costs}}{\text{Annual Energy Production} \cdot \text{Lifetime}}, \quad (2.1)$$

where the total costs include the capital costs, operation, maintenance, and decommissioning. Historically, fossil fuel costs are at the low range of USD 0.045 to USD 0.14/kWh². Nevertheless, if the health costs produced by pollution and contamination are included in the LCoE, the price increases to between USD 0.07 to USD 0.19/kWh. Until a few years ago, renewable energies were not able to compete with this low price; however, nowadays with new technologies and better logistics, wind and solar energies are capable of competing directly with fossil fuels, even without financial support [45]. The LCoE of different renewable energies is shown in Fig. 2.2 for the year 2014. In particular, it can be observed that for onshore wind energy the LCoE is in the range of USD 0.06/kWh to USD 0.12/kWh worldwide [30].

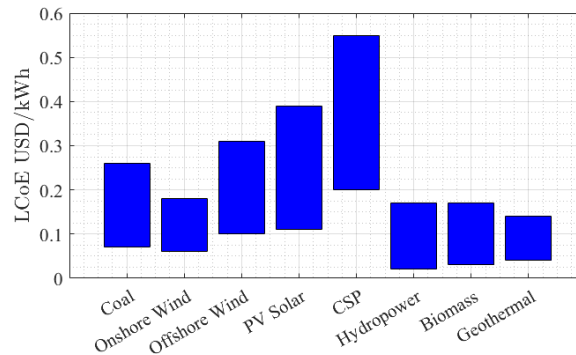


Figure 2.2: Global levelized cost of energy from different sources. PV solar is photovoltaic and CSP is concentrated solar power [30]

The use of renewable energies has quadruplicated from 2005 to 2015, installing a combined global capacity of 153 GW [28]. Traditionally, the transition has been led by Europe, yet, during 2015, other countries such as China, USA, Brazil, India, and Japan have invested heavily in renewables [28]. Improving cost-competitiveness of renewable technologies, dedicated policy initiatives, better access to financing, energy security and environmental concerns, growing demand for energy in developing and emerging economies, and the need for access to modern energy are the main drivers for the transition [45]. Moreover, the Paris agreement, signed during the 21st Conference of the Parties in December 2015, set a commitment to increase the use of renewable energies, seeking to reduce the green gas emissions and a climate-resilient development [9]. For the agreement to be met, new developments and technologies are required to decrease the final costs equally between countries.

2.2. AIRBORNE WIND ENERGY

During the last few years, wind turbines have become bigger and bigger. Towers of up to 140 meters have been specially designed for wind turbines of 3, 6 and even 8MW, aiming to capture winds at higher altitudes. The availability of wind resource is relatively small at low heights, particularly for inland countries where the wind has been substantially affected by buildings, forests, and mountains. Airborne winds are not disturbed by orography nor roughness. Thus, they possess higher

²USD prices at the value of the year 2014

intensity, constancy, and steadiness, allowing higher energy productions. Nevertheless, the cost of current horizontal axis wind turbines rapidly increases due to the extra material that is required to reach higher altitudes [23]. Moreover, when installed together, wind turbines require sizable amounts of space between each other to avoid wake effect interference; producing, as well, undesirable landscape impacts in forests and natural parks [37]. The use of kites or aeroplanes for energy production could, eventually, overcome both drawbacks.

Different authors have studied the available wind power far from the ground. Jacobson and Archer estimated a total power of 380 TW at the jet streams, i.e. air currents far from the earth surface, and 250 TW close to it [31]. Moreover, Marvel et al. [40] used a climate model to estimate the available power in the whole atmosphere and close to the ground, obtaining 1800 and 400 TW, respectively. In 2015 the global primary energy consumption was 13147.3 toe [7], equivalent to 17.5 TW. Hence, just a fraction of the potentially available energy would be required to supply the global needs.

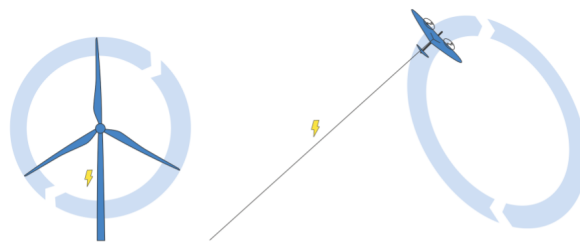
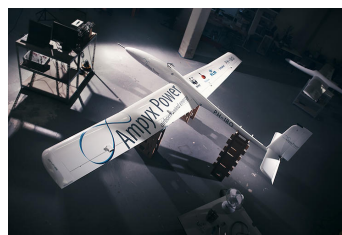


Figure 2.3: Horizontal axis wind turbine and airborne wind energy comparison [15]

Originally proposed by Loyd, airborne wind energy (AWE) aims to harvest these winds using tethered kites [38]. Loyd estimated that a wing with the size of an aircraft C-5A (576 m^2) would produce 6.7 MW at 10 m/s, an estimation that has reduced to 5.0 MW with current models [4, 27]. Fig. 2.3 shows, side by side, a horizontal axis wind turbine and an airborne wind energy system. It is observed that, as it has been explained before, AWE systems aim to harvest the wind at the tip of the blades.



(a) E-kite [17] leading edge inflatable kite



(b) Ampyx-Power [1] rigid wing aircraft



(c) Makani [39] fly generator



(d) Twingtec [47] ground generator

Figure 2.4: Airborne wind energy systems and concepts

Different concepts of AWE systems are currently under development (see Fig. 2.4), yet most of them can be decomposed in a wing, a control system and a ground station. Due to the novelty of the technology, different categories exist for each component. For example, the generator can be located at the ground or at the air, and the wing can be soft or rigid. If the generator is located along with the ground station, the tether must drive a generator; on the contrary, if the generators are located in the air, airborne wind turbines are used to produce electricity. Furthermore, a soft wing would be a kite in its different forms, e.g. leading edge inflatable or ram air, while the latter would resemble an airplane. In general, a rigid wing has a better aerodynamic performance, lifetime, and it is easier to simulate than a soft wing, but has a higher cost.

To finalize this introduction to airborne wind energy, the wind window has to be presented. The concept, originally used in kite surfing, refers to a quarter sphere located downwind from the ground control where all the maneuvers and trajectories are performed. Fig. 2.5 shows the wind window with the locations of the maximum/minimum power, plus the downwind and crosswind definitions, i.e. the wind that is behind the ground station and 90° from the wind direction, respectively.

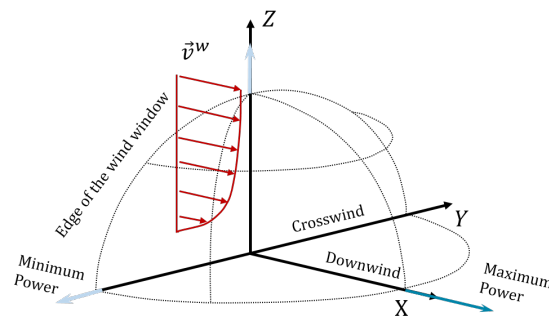


Figure 2.5: Wind window concept for an AWE system

2.3. PUMPING KITE

For this project, the pumping kite system developed by TUDelft has been considered [49]. The system is composed by a leading edge inflatable (LEI) kite and a kite control unit (KCU) connected by a single line tether to the drum/generator module at the ground. Specifically, the Hydra and V3 kites with the KCU 1.0 will be used as a basis for the computational models, whose characteristics have been obtained in [21].

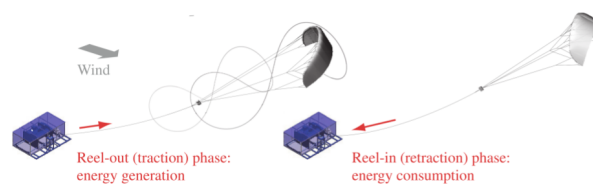


Figure 2.6: Working principle of the pumping kite power system [49]

As it has been previously explained, electricity is produced by the traction of the kite over the drum that drives the generator. Once the kite line is reeled out, the kite must be manoeuvred out of the wind windows such as to reel in the cable, consuming a fraction of the produced electricity (see Fig. 2.6). Thus, the cycles are divided into three phases: traction, retraction, and transition. The first two phases are the reel out and reel in of the tether, while the last phase positions the kite at the desired location to restart the cycle. Fig. 2.7 shows a 2D representation of the trajectory seen from the side.

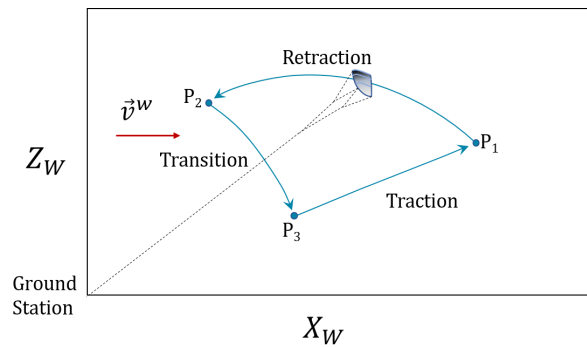


Figure 2.7: 2D representation of a pumping cycle, the points P1, P2, and P3 show the limits of each cycle. Adapted from [49]

The path followed by the kite is controlled by the KCU that, through the steering and power lines, manoeuvres the wing to predefined waypoints. The power lines change the angle of attack by moving the trailing edge of the kite, while the steering lines deform the sides producing a yaw motion [14]. The bridle connection between the kite control unit and the wing is shown in Fig. 2.8. As it can be seen, the connection also includes a weak link and a safety line that protects the kite from extreme loads.

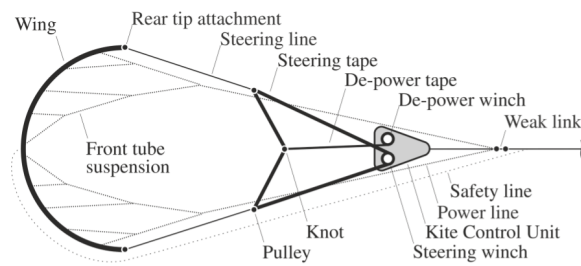


Figure 2.8: KCU and kite connections for the TUDelft AWE system [15]

Additionally, the system possesses a series of sensors, whose locations are shown as numbered red dots in Fig. 2.9. The sensors track the position and velocity of the kite (1-2), the position of the KCU controls (3), the tether force and angles (4), the wind speed and direction (5), and the temperature (3-4).

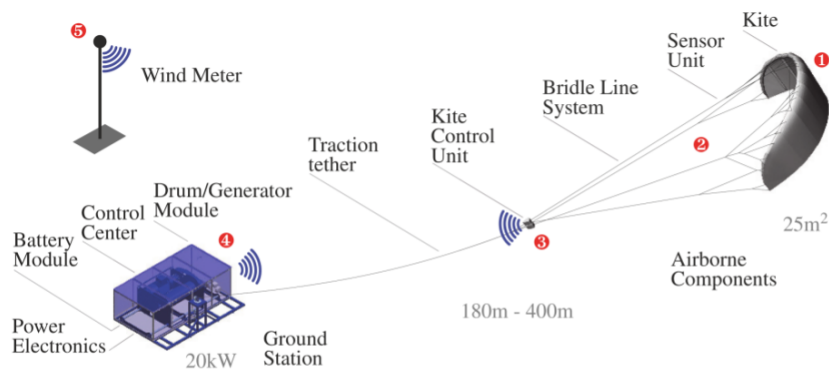


Figure 2.9: System components, sensor locations (circles) and wireless connections [49]

2.4. COMPUTATIONAL MODELS

2.4.1. KITE MODELS

To simulate the behaviour and energy production of AWE systems different models have been developed. The first analytical model to quantify the potential of a kite system was proposed in 1980 by Miles Loyd, who considered a massless kite with a straight tether [38]. Loyd established two main flight modes: perfect crosswind flight and simple non-maneuvring flight. In the former, the kite line is parallel to the wind direction, while in the latter the kite flies as high as possible without steering inputs. According to Loyd, real flight occurs between these two modes. Since then, several models with different fidelity have been developed. The more complex models aim to represent the full flow around the kite, frequently used to capture aeroelastic effects and non-linear deformations, while the simplest models are commonly used for optimisation purposes. The structural representation can be separated as flexible and rigid models. Examples of the first are finite element (FEM), multi-body, multi-plate, and particle system models; while for the former are some particle system, rigid body and point mass models. Additionally, different models are used to simulate the aerodynamic behaviour of the wings; the most common being CFD, strip theory and vortex-lattice.

FEM and multi-body aim to simulate the complete behaviour of the kite coupling sophisticated structural and aerodynamic models. As the name indicates, the former discretizes the structure into small finite elements where strains and stresses are calculated. Thus, it can accurately capture all the dynamic effects of the kite. The latter, on the other hand, represents the wing as a series of interconnected rigid bodies, capturing only global deformations. Bosch [6] and Breukels [8] used the same finite strip aerodynamic model along with a FEM and multi-body structural representation, respectively. Bosch's model captured fairly well the highly non-linear behaviour of the kite, including an asymmetric twist while cornering and a jellyfish (harmonic arc shape bending) motion when subjected to a force disturbance. Moreover, Breukels' results showed remarkable similarity with real-flight manoeuvres. Geschiere [25] expanded Bosch's model, such as to consider a more elaborate kite, bridle connection, and an extendable tether. Nevertheless, only qualitatively good results were obtained.

Williams et al. [54] used plate theory to model the structural behaviour of the kite, hence, some flexibility was accounted by simulating the kite as a series of plates connected through hinges. Additionally, the aerodynamic forces at the kite were calculated using a vortex-lattice method, i.e. modelling the flow around each plate. The results showed that the model was able to capture the primary deformations of the kite, proving to be useful for the design and testing of new controllers.

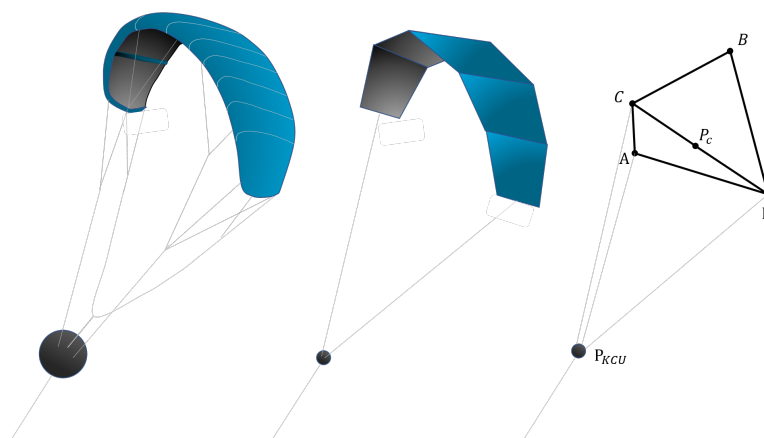


Figure 2.10: Different kite system models. From left to right multi-body, multi-plate and four particle system, adapted from [22, 25, 53]

Both Furey and Harvey [24] and Fechner et al. [22] used a particle approach to represent each section/airfoil of the kite. Furey and Harvey [24] considered a wing with many flexible particles connected through springs that moved with Newton's second law of motion. Although the simulations seemed reasonable, no validation of the model was performed. On the contrary, Fechner et al. [22] only used four rigid particles: three to represent the kite and one for the centre of gravity. In both cases, a look-up table was used to obtain the aerodynamic coefficients for each particle/airfoil. The dynamic response of the modelled kite and the response measured during flight correlated fairly well, accurately predicting the power production, trajectory, duty cycle, and efficiency. The main advantage of particle models is their capability to represent side forces and inertia, allowing a good description of the steering capabilities of the wing while being computationally light.

If deformations are not taken into account, a rigid body model is obtained. These kinds of models are widely used for aircraft simulations. De Groot et al. [13] reduced the states of the multi-body structural model developed by Breukels [8] to a rigid body, using a vortex-lattice method to calculate the aerodynamic forces. The results accurately fitted the aerodynamic forces and moments response curves for a large part of the investigated domain. Moreover, the model agreed fairly well with the results from the multi-body simulation, yet unstable situations were encountered in some regions of the flight domain.

Finally, the simplest models to simulate the aerodynamic behaviour of a kite are the point mass models. On them, all the aerodynamic, inertia and mass properties are concentrated/calculated in a single point kite. Thus, translational dynamics are considered, yet attitude changes are instant and no flexibility is taken into account [8]. No structural model is required, while a look-up table obtained from experiments or simulations is used to calculate the aerodynamic forces. Argatov et al. [4], Fechner et al. [22], van der Vlugt et al. [50] and Fagiano [19] developed similar point mass models, differing in the way that the kite and tether properties (i.e. mass, inertia and aerodynamic coefficients) are considered and how the problem formulation is solved (approximation or exact solution). Validations of the different models show, in general, good agreement between the cycle characteristics, aerodynamic forces, and power production; nevertheless, a calibration of the model is usually required.

2.4.2. TETHER MODELS

As explained in Section 2.3, the tether connects the kite and the ground station, affecting the dynamics of the kite system. Similar to the kite, the tether is affected by gravitational, aerodynamic, and inertial forces.

Fechner et al. [22] proposes to model the kite tether as a fixed number of lumped masses, connected with n spring-damper elements. The model extends the tether by lengthening the elements, allowing a more accurate description of the kite line deformation and sagging. Although the simulations resembled fairly well the experiments, the method must be calibrated for the particular AWE system before using. The same approach is taken by Rancourt [44], who developed a high fidelity model based on extensible lumped masses. The simulations showed good agreement with analytical solutions; which allowed him to formulate a fast low fidelity model under a straight tether approximation with less than 1% error. Finally, [52] also uses a dynamic model based on lumped masses, yet, to simulate the extensible line, inelastic elements are added and subtracted to the line. Although the simulations obtained accurate results, stability issues were encountered if the simulation was not properly tuned.

Straight tether models aim to capture the forces due to the kite line, normally considering the aerodynamic and gravitational force. Williams et al. [53], Fagiano [19], van der Vlugt et al. [50], Argatov et al. [4], and Bosch [6] all use a straight tether. Depending on the author, the forces are

explicitly considered during the sum of forces or added to the kite properties, i.e. increasing the equivalent mass and drag of the kite. An extensive revision has been presented by Argatov et al. [5], obtaining a better description for the drag force, sagging, and the effect of the tether on the angle of attack of the kite.

Finally, a simple approximation can be obtained if the aerodynamic effects are neglected since the line will take the form of a catenary. A catenary is a parabolic-like shape that a tether forms due to its own weight when supported in the extremes [42]. The advantage of assuming a catenary deformation is that the shape and the forces can be easily calculated, yet it is not physically correct.

2.5. CONTROL

To manoeuvre the kite in the desired trajectory, fast controllers and sensors are required; especially, since a kite can reach up to 25 m/s during a normal flight [48]. Overall, three main tendencies exist to control the kite: PID, optimal control (mainly NMPC) and hierarchical control. PID are control loop feedback mechanisms that calculate the error with the expected trajectory and react accordingly. The name comes from the control strategy, i.e. proportional, integral and derivative. Hence, the controller responds proportionally with the current error value, with the accumulated value and the rate of change of it. Nevertheless, AWE systems are highly non-linear, and appropriate strategies must be adopted when using PIDs. A more advanced and sophisticated approach is given by optimal control, aiming to model the near future and optimise/find the required inputs such as to obtain a reference path or trajectory. Finally, the third type of control aims to relate the steering capabilities of the wing with the steering input using a cascade of inputs and outputs for control.

PID controllers have been used in Williams et al. [52] and Fechner [21]. Williams et al. [52] developed a unified kite-winch controller based on the rate of change of the angle of attack, roll angle, and tether length to control the position and trajectory of the wing. The simulations included steady and unsteady wind conditions, showing good control of the three desired parameters, yet no consideration for non-linear behaviour is taken and, practically speaking, precise measures of the rate of change of the angle of attack are difficult to obtain. Fechner [21] proposes a PID controller with non-linear dynamic inversion (NDI), controlling only the heading angle (the physical orientation of the kite w.r.t a reference system, see Section 3.2) as depicted in Fig. 2.11. The NDI aims to compensate the non-linear behaviour of the system by re-stating and linearizing the problem. The simulations showed that the controller formed slightly asymmetrical figures of eight, yet it performed fairly well even including extreme gusts and sensor errors. An improved version of the controller included the consideration of the course angle (the angle of the apparent speed w.r.t a reference system, see Section 3.2) obtaining a better performance at high turbulence. Finally, PID controllers require a reference or attraction point that is used to indicate to the kite where to fly. The higher the number of attraction points, the higher the constraints (see Section 5.2).

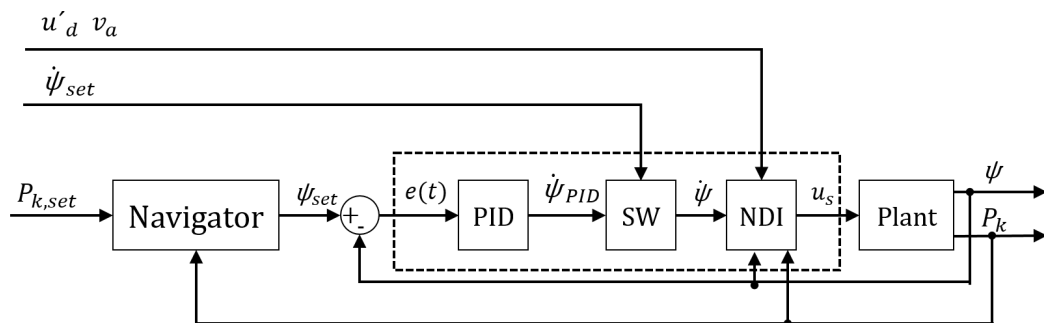


Figure 2.11: Heading PID controller with NDI, adapted from [21]

Another widely used control strategy is optimal control, mainly non-linear model predictive control (NMPC). The use of NMPC in airborne wind energy system was originally proposed by Diehl et al. [16]. The idea behind the controller is to find the required inputs such a reference path is obtained. Thus, a complete description of the reference path must be given and not only attraction points as in PID or hierarchical control. The discretize inputs are obtained solving a short term optimisation problem, frequently using the least square error between the system state and the reference state as a cost function. Different discretization schemes exists, such as, *Hamilton-Jacobi-Bellman equation*, *indirect methods* and *direct methods*; where, due to its flexibility and robustness, the latter is the most widely used [36]. Fast optimal control solvers must be implemented to solve each time step, such as the real-time iterative algorithm presented in [16], or the sequential constrained GaussNewton quadratic programming algorithm used in [19]. For NMPC, different inputs have been considered, for example, Diehl et al. [16] and Canale et al. [10] used the roll angle of the kite, Fagiano [19] used the yaw and sideslip angle, while Lago Garcia [36] used the reeling velocity, roll angle, and roll speed. In general, the simulations and experiments seem promising, yet a fast and accurate implementation is required to obtain a good performance of the system [16, 29, 32].

Finally, a hierarchical control has been developed by Fagiano and Novara [20] and Jehle and Schmehl [32]. The main idea is to separate the control in different hierarchies that are only connected to the adjacent levels. Jehle and Schmehl [32], based on the turn rate law, developed a hierarchical control for yaw controlled kites. The controller has three embedded loops, calculating the desired course angle (high level), the required course rate (middle level) and, finally, the needed steering input (low level). Despite the relatively simple description, a good behaviour was obtained during flight test. Fagiano and Novara [20] divides the control strategies in traction and retraction phase for roll control kites. For the former it is proposed to use three embedded loops (see Fig. 2.12) to control the kite positions (top level), heading (middle level) and steering (low level). Similar to PID, two reference points are used to control the width and the elevation of the traction phase, alternating between them according to the position of the kite. Additionally, a bang-bang like manoeuvring is used for the turning, i.e. the steering rate or input is constant during turning. The validation of the controller showed good agreement with the flying path of the simulation, yet quantitative differences were encountered in the traction force. For the retraction phase, Zraggen et al. [58] proposes two strategies: control the velocity angle or the elevation angle. The former uses three embedded loops (position, velocity angle, and steering), while the latter only requires two levels (position and steering). Both ideas place the kite at an equilibrium point given by a reference elevation angle that is obtained from the linearization of the equations of the motion. The simulations and experiments showed that both strategies successfully controlled the kite, yet the latter approach is more promising since it only relies on measured variables.

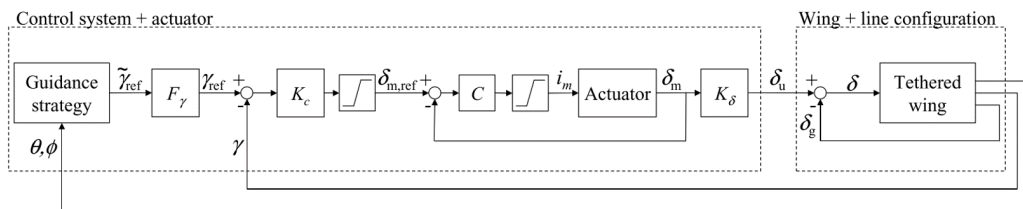


Figure 2.12: Hierarchy controller proposed by [20]

2.6. PATH OPTIMIZATION

Contrary to wind turbines, where the trajectory is given by the physical constraints of the rotor, AWE systems require a path optimisation to maximise the energy production. Loyd originally calculated a circular path, since its modelling and control is relatively straightforward. In this case, the power production depends on the diameter of the circular path, the elevation, and the reel in/out of the tether. Makani [39], E-kite [17], Kitemill [34], Twingtec [47] still use this simple concept. Williams et al. [53] used a free path optimisation for towing kites and power generation kites considering a cost function with periodic constraints and using the Legendre pseudospectral method to solve the stated problem. In optimisation, a cost function represents the main characteristic, or cost, of the process, which must be maximised/minimised to obtain the optimal result of the system. For the optimisation, Williams et al. [53] took into consideration the position and velocity of the kite, in addition to the total cycle time, i.e. reel in/out velocity. For power production, his results showed that the path had an elliptical shape with low elevation that increased the diameter with higher cycle times and it was heavily dependent on the constraints of the problem, especially the reel in/out and minimum elevation angle.

Similarly, Costello et al. [12] formulated the problem as a real-time optimisation, using the traction force of a towing kite as the cost function. Costello considered a circular path without time constraints and periodic boundary conditions. Interestingly, their uncertainty analysis showed that the turning rate, wind speed, glide ratio and kite angle with respect to the boat direction are the main uncertainties in the system, with the turning rate being the most sensitive one. The results showed an optimal shape with an elliptical path, similar to Williams et al. [53], which increased the traction force up to 25%, nevertheless, no validation of the results was performed.

Different results were obtained by Horn et al. [26] who optimised a pumping kite system. Horn et al. [26] considered the average power over time as a cost function, penalising the steering input and using altitude and angle of attack constraints. The optimisation was solved using the IPOPT [2] solver provided by the optimisation environment CasADi [51]. The results showed that the maximum power output was given by four circular loops per cycle with a retraction on the side (see Fig. 2.13).

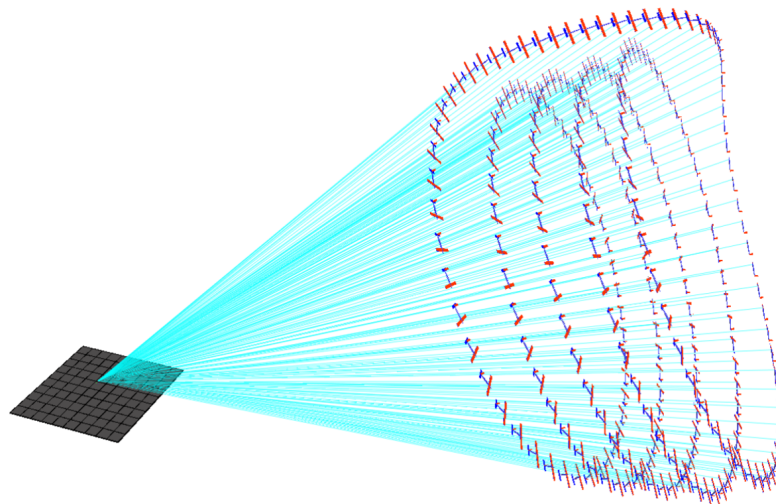


Figure 2.13: Pumping trajectory with five loops per cycle, adapted from [26]

The main disadvantage of a circular path is that, if multiple tethers are used, the circular path will produce entangling of the tether, while, if one tether is used, the path will twist the line; increasing fatigue damage. Although a special device can be employed between the KCU and the tether

or even the direction of the circle can be changed after each cycle to untangle the kite line, different projects are using an infinity or eight shapes to avoid this problem. The optimisation of the eight shape, however, is more complicated since, in the worst case scenario, an asymmetric infinity path would need to specify the height and width of each side; the angle at which the aircraft starts forming the new circle; the elevation and the reel in/out of the tether. Windlift [55], Kitegen [33], Kitepower [35], Enerkite [18], Ampyx-Power [1] are some of the companies that currently use the latter concept.

Houska and Diehl [27] formulated the optimal trajectory using the mean power in the cycle as the cost function, considering just one eight-figure with free cycle time and periodic boundary conditions. The problem was discretized using a direct multiple shooting method. As control, the algorithm uses the kites roll angle, lift coefficient and the length of the tether. The results showed that an asymmetric figure of eight was the optimum, in which the last part of the figure was the retraction phase [27].

The methods explained so far can be considered offline methods, since the controller just reproduces the trajectory optimised previous to the flight. A unique approach has been taken by Zraggen et al. [57], who maximised the tether force during the flight by aligning the kite trajectory with the wind window. Zraggen et al. [57] argues that an optimal path computed offline would be subject to model-plant mismatches due to the wind speed and AWE system modelling, leading to a sub-optimal power production. Moreover, they indicate that “the location of the path with respect to the wind direction and vertical profile has much greater importance than its shape”. Hence, they parametrized the trajectory in symmetric figures of eight, in which the width and height of the figure are pre-set, and the algorithm only seeks to centre the figure with the wind window. The presented algorithm works as an extension that can be included in any AWE controller with periodic trajectories. The simulations and experimental results showed good performance, increasing the tether force up to 2.5 times from an unoptimized trajectory [57]. Nevertheless, the algorithm does not optimise the retraction phase and does not take the reel speed into account.

2.7. CONCLUSIONS, RESEARCH QUESTION AND METHODOLOGY

The different optimisation methods, models and control strategies have been addressed during the literature study. The results show that i) the online optimisation technique presented by Zraggen et al. [57] seems suitable for the path optimisation since a) the optimisation is done during the flight, b) it is computationally light, and c) does not require the wind direction at the kite. Thus, the aim of the project is to enhance the algorithm, such as to support traction and retraction phases. ii) The quasi-steady model is a good choice to simulate the kite behaviour and test the optimizer; however, the model has not been yet validated. Thus, before using it, the model will be validated against the experimental results from Oehler [43]. If the quasi-steady model does not suffice the required accuracy, the extended point-mass model from [22] will be used. iii) Three possible models will be considered for the tether: a) the high fidelity model from Fechner et al. [22], b) the low fidelity model from Rancourt [44] and c) the lumped model by Noom [42]. Depending on the preliminary results, one of them will be chosen for the simulations. iv) No structural model will be used since the two chosen point mass model do not include any structural deformation. v) A perfect winch and generator will be considered. Thus, the winch is capable of reeling in/out the cable instantly, while the generator has no losses. vi) Finally, due to its proven performance during flight, the hierarchical control developed by [32] will be used.

Hence, the main goal and sub-objectives that will be carried out throughout the thesis are:

Main Objective: The objective of the research is to maximise the energy production of an airborne wind energy system by creating an online optimisation algorithm that maximises the power

production of the cycle.

- Sub-Objective 1: Model the path of the kite by using a quasi-steady or a dynamic model.
- Sub-Objective 2: Compare the tether models and chose one to be used throughout the project.
- Sub-Objective 3: Validate the quasi-steady model.
- Sub-Objective 4: Develop a controller and a path planning strategies for the simulations.
- Sub-Objective 5: Identify the most important parameters that need to be optimised during each phase.
- Sub-Objective 6: Use the optimizer in a test case.

Additionally, the research questions have been classified into two groups. First, the thesis aims to solve the optimisation problem by using an online algorithm, and second, the thesis seeks to validate the quasi-steady model by using experimental flight data.

- **Main Question 1:** What is the optimal path to fly a kite?
 - **Sub-Question 1.1:** What are the main parameters that have to be optimised during traction and retraction?
 - **Sub-Question 1.2:** What is the sensitivity of each parameter?
 - **Sub-Question 1.3:** How should the trajectory be described?
 - **Sub-Question 1.4:** When should each phase start?
 - **Sub-Question 1.5:** What effect does the figure have on the power production and manoeuvrability?
- **Main Question 2:** Is the quasi-steady formulation able to model the velocities, the forces and the power production of the system?
 - **Sub-Question 2.1:** What are the assumptions of the quasi-steady model?
 - **Sub-Question 2.2:** What are the required inputs from the model?
 - **Sub-Question 2.3:** What are the most sensitive parameters that affect the model?

3

SYSTEM MODELLING

The present chapter describes i) the atmospheric model in use, ii) the reference systems, iii) the tether and iv) the kite models. In turn, the tether model is divided into three subsections that present the high fidelity, low fidelity and lumped models. Finally, two kite models are presented, namely the point mass dynamic and quasi-steady models.

3.1. ATMOSPHERIC MODELING

The troposphere is the layer where most of the meteorological events take place, extending up to 12-20 km height. It is constituted by the free atmosphere and the atmospheric boundary layer (ABL). The free atmosphere is governed by the geostrophic balance, i.e. the Coriolis forces and pressure gradient are the dominant forces, while the latter is driven by shear forces and convection. Depending on the temperature gradient, the ABL can vary from 1 to 2 km. Moreover, in the lowest zone of the ABL - where the vertical moment and heat flux are almost constant - a new layer is located: the surface layer. In this layer, the wind intensity is driven by surface friction and the vertical gradient of temperature, typically defined as 10% of the atmospheric boundary layer. Conventional engineering approaches to simulate the mean wind speed at the ABL, regularly used for wind turbines, are the power law and the logarithmic law. Airborne wind energy systems, however, may fly outside this region, commonly between 0.25 and 1 km. Ideally, simulations of the entire atmospheric boundary layer should be used with programs such as the Weather Research and Forecasting (WRF), yet this is not computationally feasible. To overcome this, Archer and Jacobson [3] proposed to use a modified version of the log law given by

$$v^w(z) = v_R^w \frac{\ln(\frac{z}{z_0})}{\ln(\frac{z_R}{z_0})}, \quad (3.1)$$

where $v^w(z)$ is the wind speed at the height z , v_R^w the reference velocity, and z_0 the roughness length at the reference height z_R . Moreover, due to the working height of the system, the density cannot be assumed constant and must be calculated at each position according to

$$\rho = \rho_0 e^{-z/8550}. \quad (3.2)$$

3.2. REFERENCE SYSTEMS

Depending on the aerodynamic model, two different reference system will be used to describe the position and orientation of the kite: i) an ECEF (earth-centered, earth-fixed) and ii) a spherical co-

ordinate system. ECEF is used mainly for the point mass model of Section 3.4.1, while the spherical coordinates are used for the quasi-steady model of Section 3.4.2.

Fig. 3.1 shows the kite in spherical coordinates on the left and in ECEF on the right. Notice that the ECEF system uses the denominated small earth centred (SEC), locating the centre of the sphere at the ground station and not at the centre of the earth as in GPS systems.

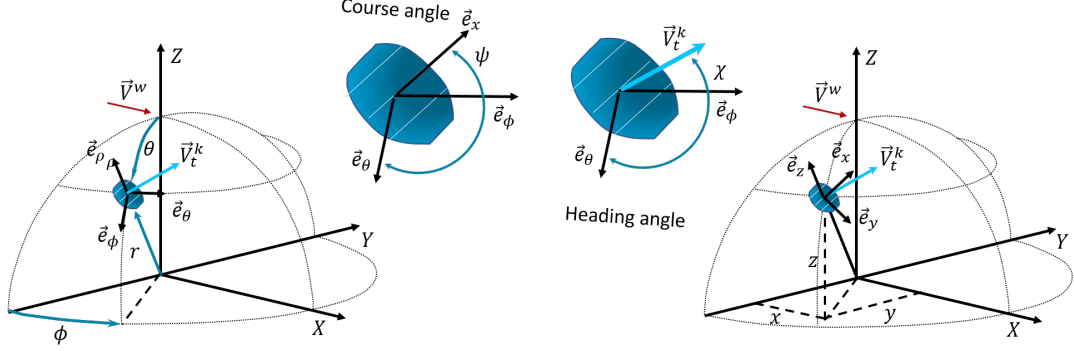


Figure 3.1: Spherical and ECEF reference system, adapted from [21]

Following the nomenclature in the figure, \vec{e}_x, \vec{e}_y and \vec{e}_z ($\vec{e}_r, \vec{e}_\theta$ and \vec{e}_ϕ) are the non-inertial, or body-fixed, coordinate system. Two additional angles are used to define the orientation of the kite in the tangential plane: the heading angle ψ , and the course angle χ . The heading ψ is defined as the physical orientation of the kite with respect to the south, i.e. the angle between \vec{e}_θ and \vec{e}_x , while the course angle χ is defined as the kite velocity with respect to the south, i.e. the angle between the \vec{e}_θ and \vec{v}_k . The two middle figures between the wind windows represent both cases. The difference between the heading angle and the course angle, denominated side slip angle, will be neglected under the assumption that the kite always moves in the direction to where is pointing.

The transformation between global coordinate systems is given by

$$\vec{p} = \begin{bmatrix} r \\ \theta \\ \phi \end{bmatrix} = \begin{bmatrix} \sqrt{X^2 + Y^2 + Z^2} \\ \frac{\sqrt{X^2 + Y^2}}{Z} \\ \arctan \frac{Y}{X} \end{bmatrix}, \quad (3.3)$$

while the transformation between local coordinate systems is given by

$$\begin{bmatrix} \vec{e}_r \\ \vec{e}_\theta \\ \vec{e}_\phi \end{bmatrix} = \begin{pmatrix} \sin \theta \cos \phi & \sin \theta \sin \phi & \cos \theta \\ \cos \theta \cos \phi & \cos \theta \sin \phi & -\sin \theta \\ -\sin \phi & \cos \phi & 0 \end{pmatrix} \begin{bmatrix} \vec{e}_x \\ \vec{e}_y \\ \vec{e}_z \end{bmatrix}. \quad (3.4)$$

3.3. TETHER MODELS

This section presents three models to describe the forces at the tether: i) the high fidelity model, ii) the low fidelity model, and iii) the lumped mass model. The first model discretizes the tether as a series of masses connected through springs and dampers, allowing to sag and deform. The second model assumes that the tether is straight during flight, yet the aerodynamic forces are still calculated in discretized elements. Finally, the lumped model calculates an equivalent mass and drag coefficient that combines the forces of the kite and the tether.

3.3.1. HIGH FIDELITY TETHER MODEL

The full behaviour of the tether-kite interaction can be modelled using a series of masses interconnected with springs and dampers. The approach explained in this section follows the guidelines given by Fechner et al. [22] and Rancourt [44] using the ECEF coordinate system explained in Section 3.2. The tether has been divided into N lumped masses (denominated nodes) and $N+1$ tether elements. According to Newton's second law of motion, a node of the line will be affected by

$$\sum \vec{F}_j^t = \vec{F}_j^{t,g} + \vec{F}_j^{t,aer} + \vec{F}_j^{t,e} + \vec{F}_j^{t,c} + \vec{F}_j^{ext} = m_j^t \vec{a}_j^t, \quad (3.5)$$

where $\vec{F}^{t,g}$ are the gravitational forces, $\vec{F}^{t,aer}$ the aerodynamic forces, $\vec{F}^{t,e}$ the elastic forces, $\vec{F}^{t,c}$ the damping forces, \vec{F}_j^{ext} are the external forces, m_j^t is the mass of the node and \vec{a}_j^t the acceleration of the node. The sub-index j indicates the mass nodes where the forces are considered. The forces acting in one node are displayed in Fig. 3.2. During the rest of the section the super-index t has been dropped for simplicity; additionally, unless explicitly indicated, all the coefficient refer to tether properties.

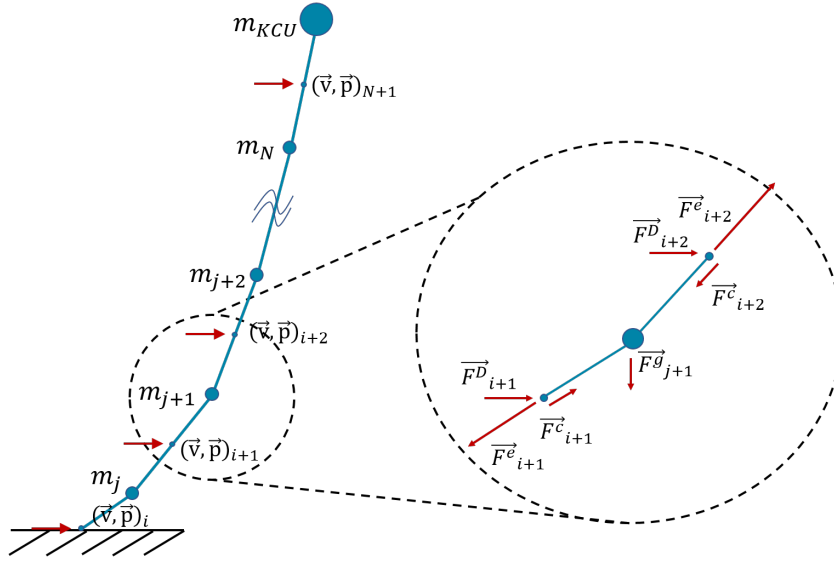


Figure 3.2: Tether nodes, forces and velocities

Notably, the centre of the element p , and the location of the mass nodes m is not the same. In fact, the mass is located between two elements using the sub-index j , while the centre and the velocity of the element use the sub-index i .

Eq. (3.5) is used to describe the forces and accelerations of each element of the tether at each instant of the flight. At the beginning of each time step, the tether is discretized evenly and the tether properties adjusted, such as to maintain the equivalency between the deformed and the non-deformed states. This means, for example, that the length per mass of the tether is decreased to maintain the mass of the deformed tether constant. Hence, the discretization of the tether and the elastic and damping coefficients are given by

$$l_s = \frac{L}{N} + \frac{\dot{r} \Delta t}{N}, \quad (3.6)$$

$$k_i = k_0 \frac{l_s}{l_i}, \quad c_i = c_0 \frac{l_s}{l_i}, \quad \text{and} \quad \sigma_i = \sigma_0 \frac{l_s}{l_i}, \quad (3.7)$$

with

$$\sigma_0 = \rho^t \pi / 4 d^2, \quad (3.8)$$

where L is the non-deformed length of the tether in the last time step, \dot{r} is the reel out/in velocity, Δt the time step, N the number of elements, l_s the non-deformed length of the elements, l_i the deformed length of each element, ρ^t the tether density, σ_0 the mass per length, d the diameter and k_0 , c_0 and σ_0 the elastic, damping and mass per length constants of the undeformed tether.

Furthermore, it can be observe in Fig. 3.2 that the mass of each node is given by half the mass of the adjacent tether elements, as

$$\vec{m}_j = \frac{\sigma_{i+1}l_{i+1} + \sigma_i l_i}{2}. \quad (3.9)$$

Notice that the last tether element $N+1$ must be included in the kite.

As Rancourt [44], the system has been written and solved using the space-state approach. The ground and the kite forces have been included in the first and last element as external forces. Although the results seem reasonable, stability issues and the required computational power make the model unsuitable for the path optimisation. The following subsection detail each force acting on eq. (3.5).

GRAVITATIONAL FORCE

The gravitational force of each node is given by

$$\vec{F}_j^g = m_j \vec{g} = m_j \begin{bmatrix} 0 \\ 0 \\ -g \end{bmatrix}. \quad (3.10)$$

AERODYNAMIC FORCES

As recommended by [44], the aerodynamic forces are calculated at the centre of each element since less elements are required to obtain a good approximation. As such, the aerodynamic forces are given by the average between the left and the right node, as

$$\vec{F}_j^{aer} = \frac{\vec{F}_i^L + \vec{F}_{i+1}^L}{2} + \frac{\vec{F}_i^D + \vec{F}_{i+1}^D}{2}. \quad (3.11)$$

In practice, the lift contribution of the tether can be neglected, due to its low lift coefficient; and the drag component can be calculated with

$$\vec{F}_i^D = \frac{1}{2} \rho_i C_D d \left(\vec{v}_{i,\perp}^{app} \right)^2 \frac{\vec{v}_{i,\perp}^a}{v_{i,\perp}^a} l_i, \quad (3.12)$$

where $\vec{v}_{i,\perp}^{app}$ is the perpendicular component of the apparent speed at each element. $\vec{v}_{i,\perp}^{app}$ is given by the difference between the wind velocity \vec{v}_i^w and the tether velocity \vec{v}_i at each element as

$$\vec{v}_i^{app} = \vec{v}_i^w - \vec{v}_i \quad (3.13)$$

$$\vec{v}_{i,\perp}^{app} = \vec{v}_i^{app} - \left(\vec{v}_i^{app} \cdot \frac{\vec{l}_i}{l_i} \right) \frac{\vec{l}_i}{l_i}. \quad (3.14)$$

ELASTIC AND DAMPING FORCES

Finally, the elastic and damping forces at each element are given by the difference between the deformation of the left and right element multiplied by the respective constant, given by

$$\vec{F}_j^e = \vec{F}_{i+1}^e - \vec{F}_i^e = k_{i+1} (l_{i+1} - l_s) \frac{\vec{l}_{i+1}}{l_{i+1}} - k_i (l_i - l_s) \frac{\vec{l}_i}{l_i} \quad (3.15)$$

$$\vec{F}_j^c = \vec{F}_{i+1}^c - \vec{F}_i^c = c_{i+1} \left(\frac{\vec{l}_{i+1}}{l_{i+1}} \cdot \Delta \vec{v}_{i+1} \right) \frac{\vec{l}_{i+1}}{l_{i+1}} - c_i \left(\frac{\vec{l}_i}{l_i} \cdot \Delta \vec{v}_i \right) \frac{\vec{l}_i}{l_i}. \quad (3.16)$$

3.3.2. LOW FIDELITY TETHER MODEL

If enough tension exists during the whole flight, the sagging can be neglected, and the forces can be calculated explicitly, significantly reducing the computational costs [44]. Thus, the drag force at each element is given by

$$\vec{F}_i^D = \frac{1}{2} \rho_i C_D d \left(v_{i,\perp}^{app} \right)^2 \frac{\vec{v}_{i,\perp}^a}{v_{i,\perp}^a} l_i \quad (3.17)$$

The total drag can be obtained either by i) modelling a discretized tether or by ii) integrating the equation along the kite line. For the first case the apparent wind speed must be calculated at each element with eq. (3.14), while for the integration the apparent speed can be approximated as

$$\vec{v}_{i,\perp}^{t,app} = \vec{v}_{\perp}^{k,app} \frac{r}{L}. \quad (3.18)$$

Hence, for the approximation, the total drag is located at 3/4 the tether length and it is given by

$$\vec{F}^D = \int_0^{l_t} \frac{1}{2} \rho C_D d \left(\vec{v}_{\perp}^{k,app} \frac{r}{L} \right)^2 \frac{\vec{v}_{\perp}^{k,app}}{v_{\perp}^{k,app}} dr = \frac{1}{6} \rho C_D d L \left(\vec{v}_{\perp}^{k,app} \right)^2 \frac{\vec{v}_{\perp}^{k,app}}{v_{\perp}^{k,app}}, \quad (3.19)$$

where C_D is the tether drag, ρ the air density, d the diameter of the tether, and L the total length of the tether.

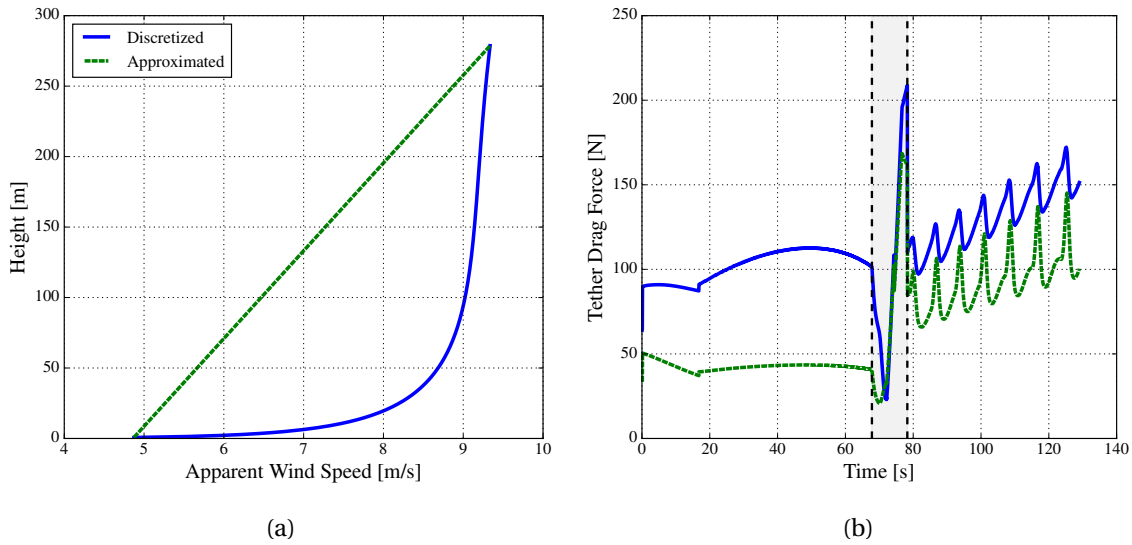


Figure 3.3: a) Apparent wind speed along the tether at $t=20s$ during retraction phase, b) Tether drag during a cycle. Both cases show the discretized and approximated cases.

Fig. 3.3 shows a) the apparent wind speed along the tether during a time step of the retraction phase and b) the drag force during the cycle. In Fig. b), it is observed that the approximated solution underestimates the tether drag during the entire circuit. The reason is seen in Fig. a), due to the profile of the wind speed, the apparent speed along the kite line is not linear. Even further, the difference is increased depending on the ratio between the kite speed and the wind speed. Thus, a higher discrepancy is obtained during retraction.

Finally, the gravitational force is given by the mass of the total tether multiplied by the gravity vector and is located at half the line, as

$$\vec{F}^{t,g} = m_t \vec{g} = \frac{1}{4} \rho^t \pi d^2 L \vec{g} = \frac{1}{4} \rho^t \pi d^2 L g \begin{bmatrix} -\cos(\theta) \\ \sin(\theta) \\ 0 \end{bmatrix}. \quad (3.20)$$

3.3.3. LUMPED TETHER

The low fidelity model assumes that the tether behaves as a straight rod that can not sag or extend, only adding weight and drag to the system. Thus, both forces can be included as kite properties, increasing the effective weight and drag of the kite. As proposed by Noom [42], to obtain the weight contribution at the kite, the gravitational force must be decomposed in radial and tangential forces

$$\vec{F}^{t,g} = \vec{F}_r^{t,g} + \vec{F}_t^{t,g}, \quad (3.21)$$

where the radial and tangential components are obtained by

$$\vec{F}_r^{t,g} = \int_0^L \vec{q}_r(r) dr, \quad (3.22)$$

$$\vec{M}^{t,g} = \vec{L} \times \vec{F}_t^{t,g} = \int_0^L \vec{r} \times \vec{q}_t(r) dr \Rightarrow \vec{F}_t^{g,t} = \frac{1}{L} \int_0^L \vec{r} \times \vec{q}_t(r) dr, \quad (3.23)$$

and q is the distributed mass in the radial and tangential direction, given by

$$\vec{q} = \vec{g} dm = \frac{\rho^t \pi d^2}{4L} dr \begin{bmatrix} -\sin \beta \\ \cos \beta \\ 0 \end{bmatrix}. \quad (3.24)$$

Finally, the weight contribution from the tether is

$$\vec{F}^{t,g} = \frac{\rho^t \pi d^2 L g}{4} \begin{bmatrix} -\sin \beta \\ \frac{1}{2} \cos \beta \\ 0 \end{bmatrix}. \quad (3.25)$$

In a similar manner, the aerodynamic drag can be approximated by the total moment at the ground station, given by

$$\vec{M}^{t,D} = \vec{L} \times \vec{F}^{t,D} = \int_0^L \left(\vec{r} \times -\frac{\rho C_d d \cos \epsilon}{2} \left(\frac{r \vec{v}^{w,app}}{L} \right)^2 \right) dr = \vec{L} \times -\frac{\rho C_d L d \cos \epsilon (\vec{v}^{w,app})^2}{8} \quad (3.26)$$

$$\Rightarrow \vec{F}^{t,D} = -\frac{\rho C_d L d \cos \epsilon (\vec{v}^{w,app})^2}{8}, \quad (3.27)$$

with

$$L \cos \epsilon = \left\| \frac{\vec{v}_t^{w,app}}{v_t^{w,app}} \times \vec{L} \right\|. \quad (3.28)$$

Then, an effective drag coefficient of the system is given by

$$C_D^e = C_D^k + C_D^t \frac{d^t L \cos \epsilon}{4S^k}. \quad (3.29)$$

Notice that, while eq. (3.19) used the velocity component that is perpendicular to the tether, eq. (3.26) uses the projection of the tether that is perpendicular to the apparent velocity; originally derived by [19]. The result of both equations is the same, yet the latter has the advantage that can be directly included to the kite drag coefficient.

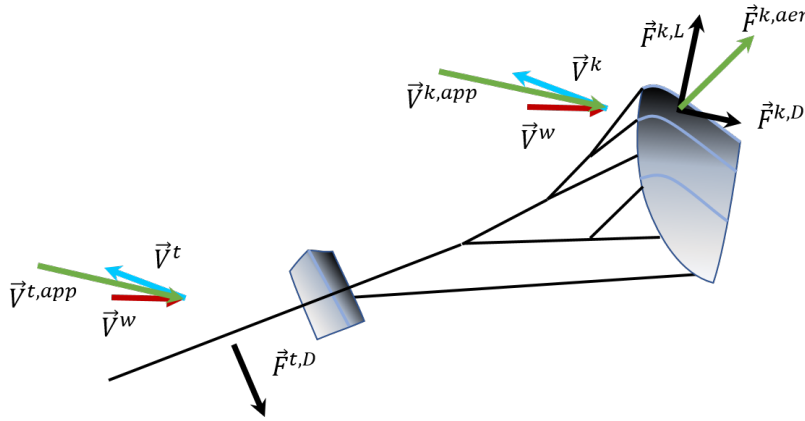


Figure 3.4: Kite and tether drag direction

The main disadvantage of the model is that by assuming that the kite and tether drag act in the same direction, the tether incorrectly increases the radial component of kite drag force. Fig. 3.4 shows a side view of the kite when flying to the zenith. By definition, the direction of the kite drag force is parallel to the apparent velocity, yet this is not the case for the tether drag. In fact, the direction of the tether drag is perpendicular to the tether; hence, it does not possess a radial component.

3.4. SYSTEM MODELING

To model the system two general approaches can be taken: i) a quasi-steady or ii) a dynamic modeling. The quasi-steady formulation assumes that the trajectory of the wing is composed by a series of equilibrium states. Thus, the model aims to seek the forces and velocities that fulfill this condition. The dynamic model, on the other hand, take into account the accelerations of the system, making the simulation more accurate and realistic. However, the computational cost for this second model rises exponentially compared to that of the quasi-steady formulation. Thus, the quasi steady model is a special case of a dynamic model. The present section starts with i) the equations of motion for a point mass dynamic model, continuing with an ii) extension to empirically include the steering capabilities and, finally, iii) the quasi-steady model.

According to Newton's second law of motion the sum of forces at the kite is

$$\sum \vec{F} = \vec{F}^{k,aer} + \vec{F}^{k,g} + \vec{F}^t = m\vec{a}^k, \quad (3.30)$$

where $\vec{F}^{k,aer}$ are the kite aerodynamic forces, $\vec{F}^{k,g}$ the kite gravitational forces, and \vec{F}^t the tether forces [46]. The first two are given by

$$\vec{F}^{k,aer} = \vec{F}^{k,L} + \vec{F}^{k,D}, \quad \text{and} \quad (3.31)$$

$$\vec{F}^{k,g} = (m_k + m_{kcu})\vec{g} \quad (3.32)$$

with

$$\vec{F}^{k,L} = \frac{1}{2} \rho (v^{w,app})^2 S C_L(\alpha) \vec{e}_L, \text{ and} \quad (3.33)$$

$$\vec{F}^{k,D} = \frac{1}{2} \rho (v^{w,app})^2 S C_D(\alpha) \vec{e}_D \quad (3.34)$$

where C_L is the lift coefficient, C_D is the drag coefficient, S the projected area of the kite, $v^{w,app}$ is the apparent wind speed, \vec{e}_L the direction of the lift force and \vec{e}_D the direction of the drag force. The two last can be calculated with

$$\vec{e}_D = \frac{\vec{v}^{w,app}}{v^{w,app}}, \quad (3.35)$$

$$\vec{e}_0 = \vec{e}_r \times \vec{e}_{D,t}, \text{ and} \quad (3.36)$$

$$\vec{e}_L = \vec{e}_D \times \vec{e}_0, \quad (3.37)$$

where \vec{e}_r is the radial direction, $\vec{e}_{D,t}$ the polar and azimuth components of the drag direction, and \vec{e}_0 the vector perpendicular to \vec{e}_r and $\vec{e}_{D,t}$ [19].

Moreover, the accelerations of the system can be written as apparent forces $\vec{F}^{k,app}$, given in spherical coordinates by

$$\vec{F}^{k,app} = -(m_k + m_{kcu}) \begin{bmatrix} \ddot{r} - r\dot{\theta}^2 - r\dot{\phi}^2 \sin^2 \theta \\ r\ddot{\theta} + 2\dot{r}\dot{\theta} - r\dot{\phi}^2 \sin \theta \cos \theta \\ r\ddot{\phi} \sin \theta + 2\dot{r}\dot{\phi} \sin \theta + 2r\dot{\theta}\dot{\phi} \cos \theta \end{bmatrix}, \quad (3.38)$$

where the $(\ddot{r}, \ddot{\theta}, \ddot{\phi})$ and $(\dot{r}, \dot{\theta}, \dot{\phi})$ are the kite accelerations and velocities.

The previous set of equations can be rewritten in spherical coordinates as

$$\vec{F}_r = \vec{F}_r^{k,aer} + \vec{F}_r^{k,g} + \vec{F}_r^{k,app} + \vec{F}_r^{t,g} + \vec{F}_r^{t,aer} - \vec{F}_r^{t,trc} = 0, \quad (3.39)$$

$$\vec{F}_\theta = \vec{F}_\theta^{k,aer} + \vec{F}_\theta^{k,g} + \vec{F}_\theta^{k,app} + \vec{F}_\theta^{t,g} + \vec{F}_\theta^{t,aer} = 0, \text{ and} \quad (3.40)$$

$$\vec{F}_\phi = \vec{F}_\phi^{k,aer} + \vec{F}_\phi^{k,g} + \vec{F}_\phi^{k,app} + \vec{F}_\phi^{t,g} + \vec{F}_\phi^{t,aer} = 0, \quad (3.41)$$

where the tether forces have been also decomposed in aerodynamic, gravitational, and traction forces. Notice that the tether traction force can only acts in the radial direction.

Finally, both aerodynamic forces depend on the apparent wind speed $\vec{v}^{w,app}$ given by the relative speed between the wind and the kite,

$$\vec{v}^{w,app} = \vec{v}^w - \vec{v}^k = \begin{bmatrix} \sin \theta \cos \phi \\ \cos \theta \cos \phi \\ -\sin \phi \end{bmatrix} v^w - \begin{bmatrix} v_r^k \\ v_t^k \cos \chi \\ v_t^k \sin \chi \end{bmatrix}, \quad (3.42)$$

where v_r^k and v_t^k are the radial and tangential components of kite velocity and χ is the course angle. Furthermore, the velocity and acceleration components of the kite can be expressed as

$$\dot{r} = v_r^k, \quad \ddot{r} = 0, \quad (3.43)$$

$$\dot{\theta} = \frac{v_t^k}{r} \cos \chi, \quad \ddot{\theta} = -\dot{\theta} \left(\frac{\dot{r}}{L} + \dot{\chi} \tan \chi \right), \quad (3.44)$$

$$\dot{\phi} = \frac{v_t^k \sin \chi}{r \sin \theta}, \quad \text{and} \quad \ddot{\phi} = -\dot{\phi} \left(\frac{\dot{r}}{L} - \dot{\chi} \frac{1}{\tan \chi} + \dot{\theta} \frac{1}{\tan \theta} \right). \quad (3.45)$$

Notice that the radial acceleration has been neglected, since the variation of the reel in/out \dot{r} is small compared with the other velocities. Finally, the mechanical power of the system is given by

$$P = F_r^{t,trc} \dot{r}. \quad (3.46)$$

3.4.1. EXTENDED ONE-POINT MODEL

The aerodynamic model presented in the previous section does not provide an accurate description for the kite to turn or account for the increase in drag due to steering. The extended one-point mass model presented by Fechner et al. [22] aims to improve this limitations by decomposing the aerodynamic forces in lift, drag and steering, as

$$\vec{F}^{k,app} = \vec{F}^{k,L} + \vec{F}^{k,D} + \vec{F}^{k,s}, \quad (3.47)$$

$$\vec{F}^{k,L} = \frac{1}{2} \rho (v^{w,app})^2 SC_L(\alpha) \frac{\vec{v}^{w,app} \times \vec{e}_y}{\|\vec{v}^{w,app} \times \vec{e}_y\|}, \quad (3.48)$$

$$\vec{F}^{k,D} = \frac{1}{2} \rho (v^{w,app})^2 SC_D(\alpha) (1 + K_{s,D} |u_s|) \frac{\vec{v}^{w,app}}{v^{w,app}}, \text{ and} \quad (3.49)$$

$$\vec{F}^{k,s} = \frac{1}{2} \rho (v^{w,app})^2 S \frac{S_{side}}{S} c_s (u_s + u_{s,c}) \vec{e}_y \text{ with} \quad (3.50)$$

$$u_{s,c} = \frac{c_{2,c}}{v^{w,app}} \sin(\psi) \cos(\beta), \quad (3.51)$$

where u_s is the steering input varying from -1 to 1, $K_{s,D}$ a constant that accounts for the drag increase due to steering, c_s is the steering sensitivity of the kite, $u_{s,c}$ is the correction term due to gravitational effects, and $c_{2,c}$ the constant that represents its influence. The coefficients must be determined experimentally by fitting the coefficients to flight data, hence, they are specific for each kite [22]. Finally, the direction of the aerodynamic forces is given by

$$\vec{e}_z = -\frac{\vec{l}_{n-1}^t}{l_{n-1}^t}, \quad (3.52)$$

$$\vec{e}_y = \frac{\vec{v}^{w,app} \times \vec{e}_z}{\|\vec{v}^{w,app} \times \vec{e}_z\|}, \text{ and} \quad (3.53)$$

$$\vec{e}_x = \vec{e}_y \times \vec{e}_z. \quad (3.54)$$

where l_{n-1}^t is the last element of the discretized tether.

3.4.2. QUASI-STEADY MODEL

The quasi-steady formulation is based on the general model presented in Section 3.4, yet, instead of calculating the accelerations as in a dynamic model, the kite radial and tangential velocities are seek such as to reach an equilibrium state. This equilibrium is obtained by iterating over the kinematic ratio κ until the correct Lift-to-Drag coefficient is encountered. Then, the kite velocities are used to calculate the new position, where the model is run again. The model uses three assumptions: i) the kite surface to mass ratio is relatively large, ii) the accelerations of the system are low, and iii) the flight is dominated by the aerodynamic and tether forces. The following subsection are divided into i) the reformulation to non-dimensional parameters, ii) the iterative solution with constant angle of attack and iii) the iterative solution with variable angle of attack. It is worth mentioning that the way in which the forces and the effective angle of attack have been address is different from the the original formulation presented by Noom [42] and van der Vlugt et al. [50].

NON-DIMENSIONAL FORMULATION

The non-dimensional parameters used in the formulation are

$$f = \frac{v_r^k}{v^w} = \frac{v_r^t}{v^w}, \quad \lambda = \frac{v_t^k}{v^w}, \quad \text{and} \quad \kappa = \frac{v_r^{w,app}}{v_t^{w,app}}, \quad (3.55)$$

where the f is the reel-out factor, λ the tangential velocity factor and κ the kinematic ratio. Under the straight tether approximation, the tether velocity v_t is equal to the kite radial velocity $v_{k,r}$. Thus, the apparent wind velocity can be expressed as

$$\vec{v}^{w,app} = \begin{bmatrix} \sin\theta \cos\phi - f \\ \cos\theta \cos\phi - \lambda \cos\chi \\ -\sin\phi - \lambda \sin\chi \end{bmatrix} v^w, \quad (3.56)$$

Then, the norm of the apparent wind speed and the kinematic ratio κ are related due to the apparent radial component $v_r^{w,app}$, as

$$\begin{aligned} v^{w,app} &= \sqrt{(v_r^{w,app})^2 + (v_t^{w,app})^2} = v_r^{w,app} \sqrt{1 + \left(\frac{v_t^{w,app}}{v_r^{w,app}}\right)^2} \\ v^{w,app} &= (\sin\theta \cos\phi - f) \sqrt{1 + \kappa^2} v^w. \end{aligned} \quad (3.57)$$

In a similar manner, a relation for the tangential velocity factor λ is obtained by combining the norm of the tangential kite apparent velocity, the radial kite apparent velocity, and the kinematic ratio κ . Thus,

$$\begin{aligned} v_t^{w,app} &= \sqrt{(v_\theta^{w,app})^2 + (v_\phi^{w,app})^2} = v^w \sqrt{(\cos\theta \cos\phi - \lambda \cos\chi)^2 + (\sin\phi + \lambda \sin\chi)^2} \\ v_t^{w,app} &= (\sin\theta \cos\phi - f) v^w \kappa \\ \Rightarrow \lambda &= a + \sqrt{a^2 + b^2 - 1 + \kappa^2(b-f)^2}, \end{aligned} \quad (3.58)$$

with

$$a = \cos\theta \cos\phi \cos\chi - \sin\phi \sin\chi \quad \text{and} \quad b = \sin\theta \cos\phi. \quad (3.59)$$

Then, according to eq. (3.30), the components of the aerodynamic force are given by

$$F_r^{k,aer} = F_r^{t,trc} - F_r^{k,g} - F_r^{k,app} - F_r^{t,g} - F_r^{t,aer}, \quad (3.60)$$

$$F_\theta^{k,aer} = -F_\theta^{k,g} - F_\theta^{k,app} - F_\theta^{t,g} - F_\theta^{t,aer}, \quad (3.61)$$

$$F_\phi^{k,aer} = -F_\phi^{k,g} - F_\phi^{k,app} - F_\phi^{t,g} - F_\phi^{t,aer}, \quad \text{and} \quad (3.62)$$

$$F^{k,aer} = \sqrt{(F_r^{k,aer})^2 + (F_\theta^{k,aer})^2 + (F_\phi^{k,aer})^2}. \quad (3.63)$$

Notice that the desired traction force $F_r^{t,trc}$ is used to calculate the equilibrium state. Finally, the reel-out factor is stated as a function of the kinematic ratio κ by using the definition of the norm of the aerodynamic force and eq. (3.57),

$$\begin{aligned} F^{k,aer} &= \sqrt{(F^{k,L})^2 + (F^{k,D})^2} = \frac{1}{2} \rho \sqrt{C_L^2 + C_D^2} S (v^{w,app})^2 \\ F^{k,aer} &= \frac{1}{2} \rho C_R S ((\sin\theta \cos\phi - f) v^w \kappa)^2 \\ \Rightarrow f &= \sin\theta \cos\phi - \sqrt{\frac{2F^{k,aer}}{\rho (v^w)^2 C_R S (1 + \kappa^2)}}. \end{aligned} \quad (3.64)$$

ITERATIVE SOLUTION WITH CONSTANT α

If the angle of attack remains constant through the flight, the velocities and forces that satisfy the requirements at each position are obtained when the calculated Lift-over-Drag G^* , given by

$$\begin{aligned} (F^{k,aer})^2 &= (F^{k,L})^2 + (F^{k,D})^2 \Rightarrow G^* = \sqrt{\left(\frac{F^{k,aer}}{F^{k,D}}\right)^2 - 1} \\ \vec{F}^{k,D} &= \frac{\vec{F}^{k,aer} \cdot \vec{v}^{k,app}}{(v^{w,app})^2} \vec{v}^{k,app} \Rightarrow F^{k,D} = \frac{\vec{F}^{k,aer} \cdot \vec{v}^{k,app}}{v^{k,app}} \\ \Rightarrow G^* &= \sqrt{\left(\frac{F^{k,aer} v^{w,app}}{\vec{F}^{k,aer} \cdot \vec{v}^{k,app}}\right)^2 - 1}, \end{aligned} \quad (3.65)$$

is equal to a predefined G . Thus, the model can be summarized as:

1. Provide a first guess of κ and f ,
2. Calculate λ ,
3. Calculate the apparent wind speed and the required aerodynamic force at the kite,
4. Calculate G^* , and
5. Iterate until ΔG is below a threshold.

3.4.3. ITERATIVE SOLUTION WITH VARIABLE AOA

The previous section explained the iterative solution under the assumption that G does not change with the flight path. Nevertheless, the apparent velocity, the depowering, and the tether sagging affect the effective angle of attack α while flying. Thus, α is given by

$$\alpha = \alpha_0 - \alpha_d + \Delta\alpha - w, \quad (3.66)$$

where α_0 is the geometrical angle of attack at zero depower, α_d is the depowering contribution, $\Delta\alpha$ is the inflow angle of the apparent wind speed and w is the tether sagging contribution. The geometric angle of attack and the depowering are kite specific and must be experimentally determined. According to Fechner [21], the depowering angle can be calculated with

$$\alpha_d = u'_d \alpha_{d,max} = \frac{u_d - u_{d,0}}{u_{d,max} - u_{d,0}} \alpha_{d,max}, \quad (3.67)$$

where u'_d is the relative depower composed by the current state u_d and the limits $u_{d,max} - u_{d,0}$, and $\alpha_{d,max}$ the maximum depowered angle. Notably, the relative depower u'_d varies between 0 and 1, and can be seen as a depower percentage.

Further, the inflow angle is given by

$$\Delta\alpha = \arcsin\left(\frac{v_r^{w,app}}{v^{w,app}}\right). \quad (3.68)$$

If the straight or low fidelity tether models are used, the sag effect can be taken into account by

$$w = \arctan \frac{d^t C_D^t L \cos \epsilon}{4SC_L}. \quad (3.69)$$

The previous equation has been originally derived by Argatov et al. [5] in a slightly different form, since i) the full length of the tether has been considered, and not only the projection of it (see the end of Section 3.3.3); and ii) the kite presented in the study is roll controlled, while the one presented here is yaw controlled. The last point will be discussed further in chapter 5.

Finally, the iterative solution with variable angle of attack can be summarized as:

1. Provide a first guess of κ , α and f ,
2. Calculate λ and the aerodynamic coefficients,
3. Calculate the apparent wind speed and the required aerodynamic force at the kite,
4. Calculate G^* ,
5. With the new kite apparent velocities recalculate α and G , and
6. Iterate until ΔG is below a threshold.

3.5. CHAPTER CONCLUSIONS

The chapter described the reference systems, environmental models, tether models and kite models. Three different models for the tether were described; namely, i) the high fidelity model, ii) the low fidelity model and iii) the lumped model. Of the three models, the discretized low fidelity model is the best option for the project. The high fidelity model, despite being the most accurate of the three, has high computational costs that makes it unsuitable for the optimisation. The lumped model creates a fictional radial component since it assumes that the tether and kite drag act in the same direction. Hence, the discretized low fidelity model and its approximation are feasible options for the optimisation. Nevertheless, due to the profile of the apparent wind speed, the approximation underestimate the tether drag.

Two kite models were presented: i) a dynamic and ii) a quasi-steady. The former model has already been proven to be a fair representation of the system [21], however, the quasi-steady model presents several advantages due to its versatility and low computational costs. To decide which model to use, the next chapter aims to validate the quasi-steady model with the experimental data obtained by Oehler [43].

4

QUASI-STEADY MODEL VALIDATION

The present chapter aims to validate the quasi-steady model presented in Section 3.4.2; to do so, the experimental data obtained by Oehler [43] will be used. The aim of the validation is to assess if the quasi-steady model can predict the velocities and power generation when the path, wind profile and force are provided. On the first part of the chapter, the description of the flight and data acquisition systems are described. The second section presents the processing of the raw data. In the third section, two different sets of aerodynamic coefficients will be used for the models and compared with the experimental results. Finally, at the end of the chapter, the conclusions are given regarding the validity of the model.

4.1. FLIGHT TEST

On April 24th, 2017, and with the objective to measure the apparent wind speed, a flight test was conducted by Kitepower [35] in cooperation with the Delft University of Technology and the University of Stuttgart. The flight consisted of a total of ten cycles with the V3 kite of 25 m² total area; each cycle was composed by, roughly, two figures and a retraction from the zenith of the wind window. During the flight, Oehler [43] measured the pitch and yaw components of the inflow angle plus the apparent wind speed. A pitot tube was used to measure the apparent wind speed, while the angles were measured using wind vanes. The airborne wind energy system of Kitepower [35], in addition, contains a series of sensors to measure the pressure, temperature, position (GPS), and attitude (IMU) of the kite plus the tether force, reel out speed, and wind speed/direction at the ground station (see Section 2.3). Fig. 4.1 shows a sketch of the installed sensor.

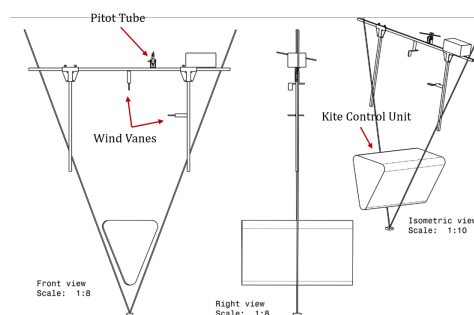


Figure 4.1: Sketch of the installed apparent wind speed sensor, adapted from [43]

In Fig. 4.1 it can be seen that the device is mounted on the power lines, roughly, nine meters

below the kite and one meter above the KCU. The decision was taken since the front lines sustain most of the tension forces, diminishing vibration or misalignment problems. Moreover, the measurements are taken far enough from the kite and the KCU such as to avoid perturbations on the flow. Notice that the pitch angle is measured perpendicular to the bridles under the assumption that the lines are aligned with the radial direction during flight.

Finally, the calibration of the sensors has been obtained from [43], while the kite and tether properties are shown in the following tables:

Property	Value	Property	Value	Property	Value
Total area	25 m ²	Projected area	19.17 m ²	Kite mass	11 kg
KCU mass	8.4 kg	Sensors mass	3.4 kg		

Table 4.1: Kite, KCU and sensor properties

Property	Value	Property	Value	Property	Value
Diameter	4 mm	Mass per length	0.013 kg/m	k_0	614600 N
c_0	473 Ns	L_{min}	250 m	L_{max}	400 m

Table 4.2: Tether Properties

4.2. DATA PROCESSING

Using the definition of forces, velocities, and the measured quantities, the flight properties can be obtained. However, previous to the processing, the data was assessed and filtered. After removing the waiting period previous and after the flight test, a total of 68692 data points were collected during the experiment, at a frequency of 20 Hz. Additionally, some missing data was encountered on the data logs, yet, since no more that five missing values were clustered together, they were reconstructed with spline curves. For the experiments, a Blackman window filter was used. The filter converts the signal to the frequency domain, filters the unwanted frequencies according to the desired window, and then converts the signal back to time domain. Fig. 4.2 shows the measured dynamic pressure ΔP before and after the filtering. Notice that the values become negative at 47.2 and 48.8 min, an explanation of this is given at the end of the next section.

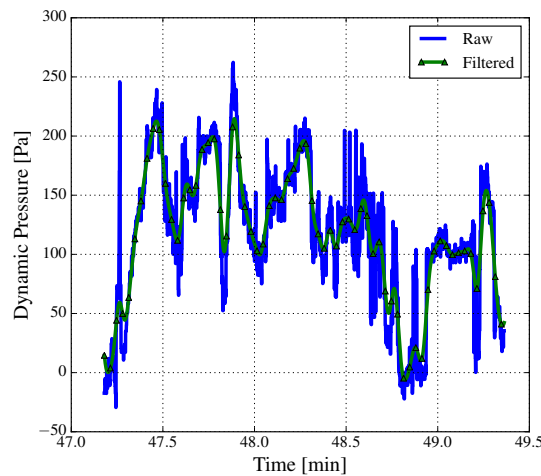


Figure 4.2: Dynamic pressure before and after filtering

After the data was filtered, eq. (3.60) to (3.63) was used to calculate the aerodynamic force at the kite, with the components of the apparent wind speed and wind speed given by

$$v_r^{w,app} = v^{w,app} \sin \alpha_{pitch}, \quad (4.1)$$

$$v_\theta^{w,app} = -v^{w,app} \cos \alpha_{pitch} \cos(\chi + \alpha_{yaw}), \quad (4.2)$$

$$v_\phi^{w,app} = -v^{w,app} \cos \alpha_{pitch} \sin(\chi + \alpha_{yaw}), \quad \text{and} \quad (4.3)$$

$$\vec{v}^w = \vec{v}^{w,app} + \vec{v}^k. \quad (4.4)$$

Then, the resultant aerodynamic coefficient, the drag force, and the lift force were calculated with

$$C_R = \frac{2F^{k,aer}}{\rho S (v^{w,app})^2}, \quad (4.5)$$

$$\vec{F}^{k,D} = \frac{\vec{F}^{k,aer} \cdot \vec{v}^{w,app}}{(v^{w,app})^2} \vec{v}^{w,app}, \quad \text{and} \quad (4.6)$$

$$\vec{F}^{k,L} = \vec{F}^{k,aer} - \vec{F}^{k,D}. \quad (4.7)$$

Further, the velocity of the kite was obtained as the gradient of the position over time, using the WGS84 model to transform from latitude, longitude, and altitude to X, Y, and Z (Earth-centered, EC) with

$$X_{EC} = (C + H) \cos(\text{lat}) \cos(\text{lon}), \quad (4.8)$$

$$Y_{EC} = (C + H) \cos(\text{lat}) \sin(\text{lon}), \quad (4.9)$$

$$Z_{EC} = \left(\left(1.0 - \frac{1}{298.3} \right)^2 + H \right) \sin(\text{lat}), \quad \text{and} \quad (4.10)$$

$$C = \frac{6378137.0}{\sqrt{\cos(\text{lat})^2 + \left(1.0 - \frac{1}{298.3} \right)^2 \sin(\text{lat})^2}}. \quad (4.11)$$

Additionally, the final inertial reference system has been located at the ground station (Small-earth centered, SEC) by subtracting the global position of the kite and the ground station. Hence,

$$X_{SEC} = X_{EC}^k - X_{EC}^{GS}, \quad (4.12)$$

$$Y_{SEC} = Y_{EC}^k - Y_{EC}^{GS}, \quad \text{and} \quad (4.13)$$

$$Z_{SEC} = Z_{EC}^k - Z_{EC}^{GS} \quad (4.14)$$

As explained in Section 3.2, no difference between the course and heading angle has been taken into account. Hence, the course angle can be obtained by

$$\chi = \begin{cases} \arctan\left(\frac{d\theta}{d\phi}\right) + \frac{\pi}{2}, & \frac{d\theta}{dt} \geq 0 \quad \& \quad \frac{d\phi}{dt} \geq 0, \\ \arctan\left(\frac{d\theta}{d\phi}\right) - \frac{\pi}{2}, & \frac{d\theta}{dt} > 0 \quad \& \quad \frac{d\phi}{dt} < 0, \\ \arctan\left(\frac{d\theta}{d\phi}\right) + \frac{\pi}{2}, & \frac{d\theta}{dt} < 0 \quad \& \quad \frac{d\phi}{dt} > 0, \quad \text{and} \\ \arctan\left(\frac{d\theta}{d\phi}\right) - \frac{\pi}{2}, & \frac{d\theta}{dt} < 0 \quad \& \quad \frac{d\phi}{dt} > 0. \end{cases} \quad (4.15)$$

Finally, although the wind speed at the kite is derived from the apparent and kite speed, the discretized tether model requires a wind profile to calculate the apparent wind velocity at each element. Hence, the wind speed during the flight test was averaged at each height and fitted through a least square method to the wind profile presented in Section 3.1. The obtained roughness length and reference height of the location are given in Tab. 4.3. Furthermore, to account for the instantaneous wind speed, the reference velocity is adapted at each time step to fit the wind speed at the kite. Thus,

although it is assumed that the shape of the profile remains constant over time, its intensity varies at each time step.

Property	Value	Property	Value
Reference height	6 m	Roughness length	0.0058 m

Table 4.3: Wind profile during the flight test

4.3. EXPERIMENT VS QUASI STEADY MODEL

As it has been explained at the beginning of the chapter, the aim of the validation is to assess if the quasi steady model is able to predict the velocities and the power generation when the trajectory, environmental conditions, and ground force are provided as inputs. As such, two cases have been considered: case 1 that uses the generic aerodynamic coefficients from [21] (see Fig. 4.3) and case 2 that uses the coefficients derived from the previous analysis.

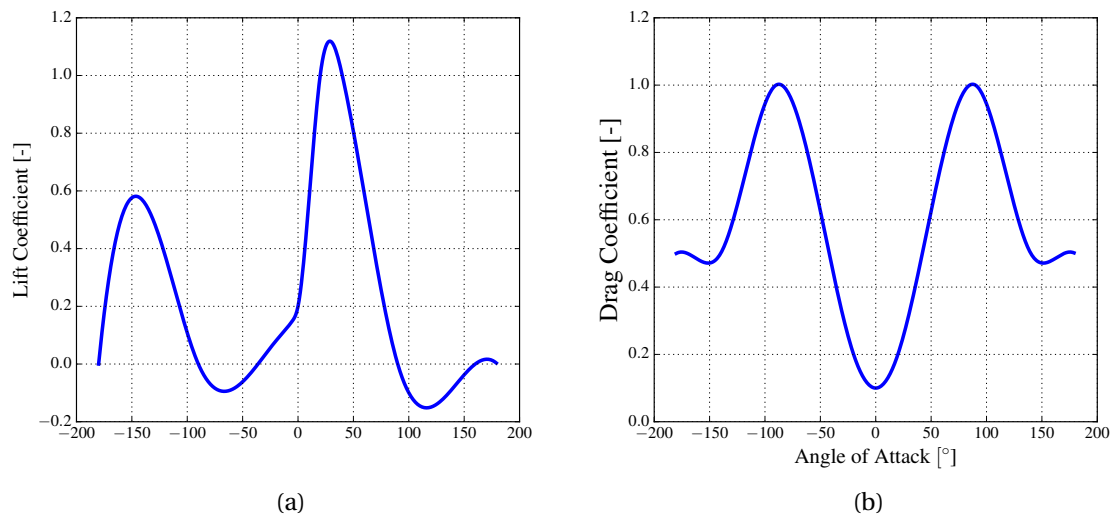


Figure 4.3: a) Lift coefficient and b) drag coefficient for the kite, adapted from [21]

Fig. 4.4 shows a) the 3D trajectory in Cartesian coordinates and b) the length of the tether over time. The data has been displayed with triangles spaced two seconds from each other. The flight starts from transition phase at roughly 200 m height and 100 m from the ground station in the X coordinate. Traction start at the first loop and last two figures, it can be seen that the figures form more an ellipsis than a figure of eight. At the end of the cycle, the course angle χ changes to 180° aiming to the zenith of the wind window. In b) the three phases have been delimited by vertical dashed lines that represent i) the end of the retraction ii) the end of the transition (grey background), and iii) the end of the traction. Notice that the tether continues to reel out after the retraction start since the aerodynamic forces are over the reel out force.

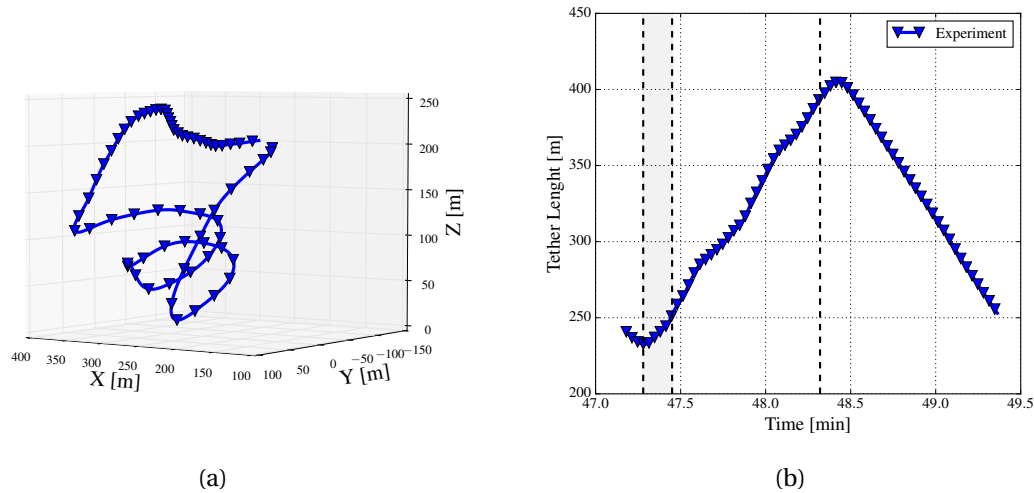


Figure 4.4: a) Trajectory flow and b) tether length during the 7th cycle. The gray area shows the transition phase.

Fig. 4.5 shows a) the side and b) the front view of the cycle. For the path planning, four points were used to indicate the heading to the controller, aiming to produce a figure of eight. However, figure b) shows that this is not achieved. Moreover, up loops have been flown in the corners of the figure, as it will be explained in Section 6.1.3 this is detrimental for the manoeuvrability of the wing. Additionally, it can be seen that the retraction is performed at the side of the figure aiming for the zenith position. Notice that the Y axis on the front view has been inverted to resemble the 3D view.

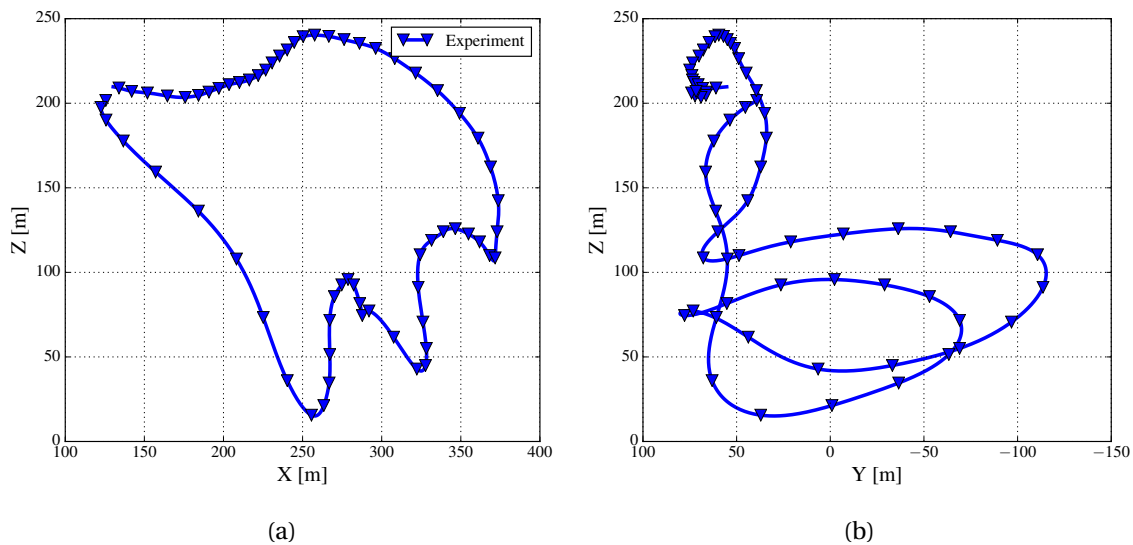


Figure 4.5: a) Side and b) front views of the trajectory

Fig. 4.6 shows the common conditions between the flight and the cases, i.e. a) the tether ground force, b) relative depower and c) density at the kite. It is important to mention that case 2 does not use the relative depower since the aerodynamic coefficients are given as inputs.

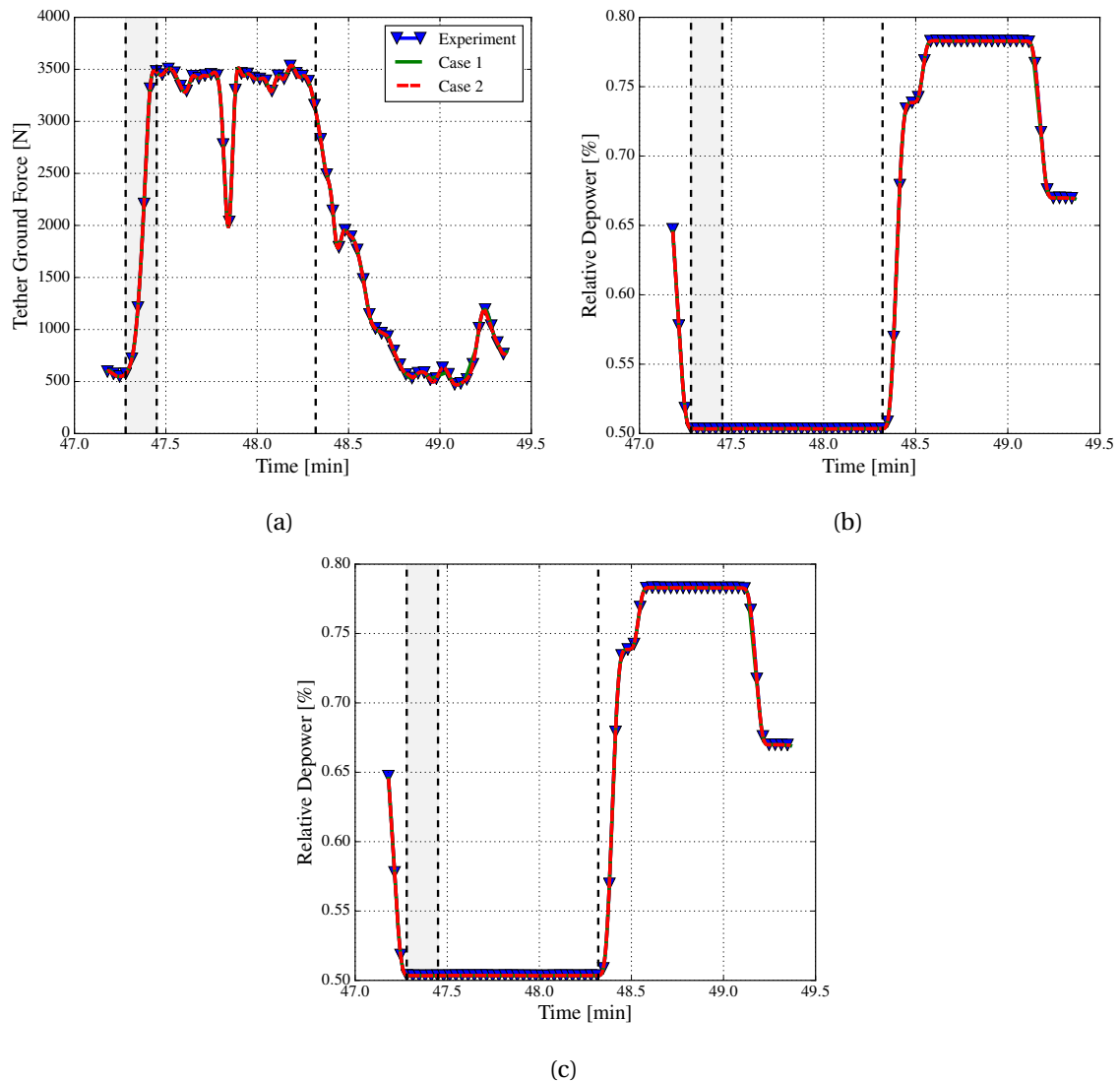


Figure 4.6: a) Tether force at the ground, b) relative depower and c) density at the kite

Fig. 4.7 shows a) the lift coefficient, b) the drag coefficient and c) the inflow angle of the experiment and the cases. As it can be seen, case 2 uses the same aerodynamic coefficients as the flight test, while case 1 uses the generic ones from Fig. 4.3. It can be concluded that i) the aerodynamic coefficients are high during traction and decrease during retraction phase. ii) The lift and drag coefficients from the generic curves are almost constant during the flight, yet far from the experimental results. iii) Despite the difference, both cases can predict fairly well the inflow angle during the traction phase. Furthermore, iv) an almost exact match is obtained if the aerodynamic coefficients of the experiment are used. Nevertheless, v) the predictions become less accurate during transition and retraction; especially case two that predicts an inflow 2.5 times higher than the one measured. A more detailed description of the problem will be given at the end of the section. In addition to the generic aerodynamic curves, vi) the exact geometry of the kite during flight is also unknown, yet it plays a major role for the steering, depower and aerodynamic coefficients. Notice that the experiment aerodynamic coefficients miss some data during transition and retraction, this is due to problems in the measurements that do not allow the aerodynamic coefficients to be calculated; hence, this time steps have not been considered for case 2.

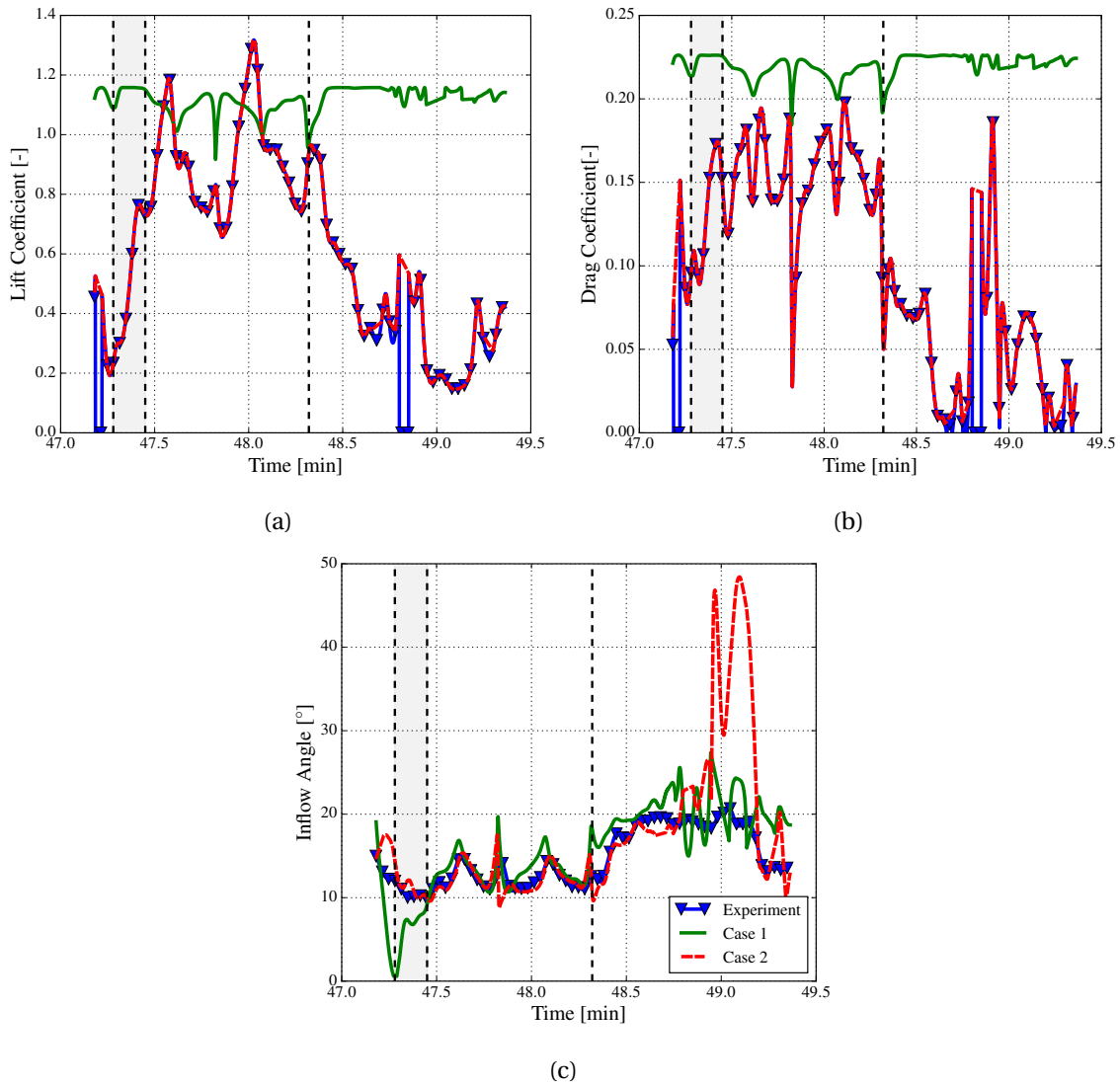


Figure 4.7: a) Lift coefficient, b) drag coefficient and c) inflow angle

Fig. 4.8 shows the three components of the kite ground and apparent velocity with respect to the ground station in spherical coordinates. Similar results are obtained as with the inflow angle, i.e. both cases can predict fairly well the traction and transition phase with an almost exact match from case 2, yet a considerable difference is observed during the retraction phase. Notice that Fig. a) v_r^k is the reel speed under the straight tether approximation.

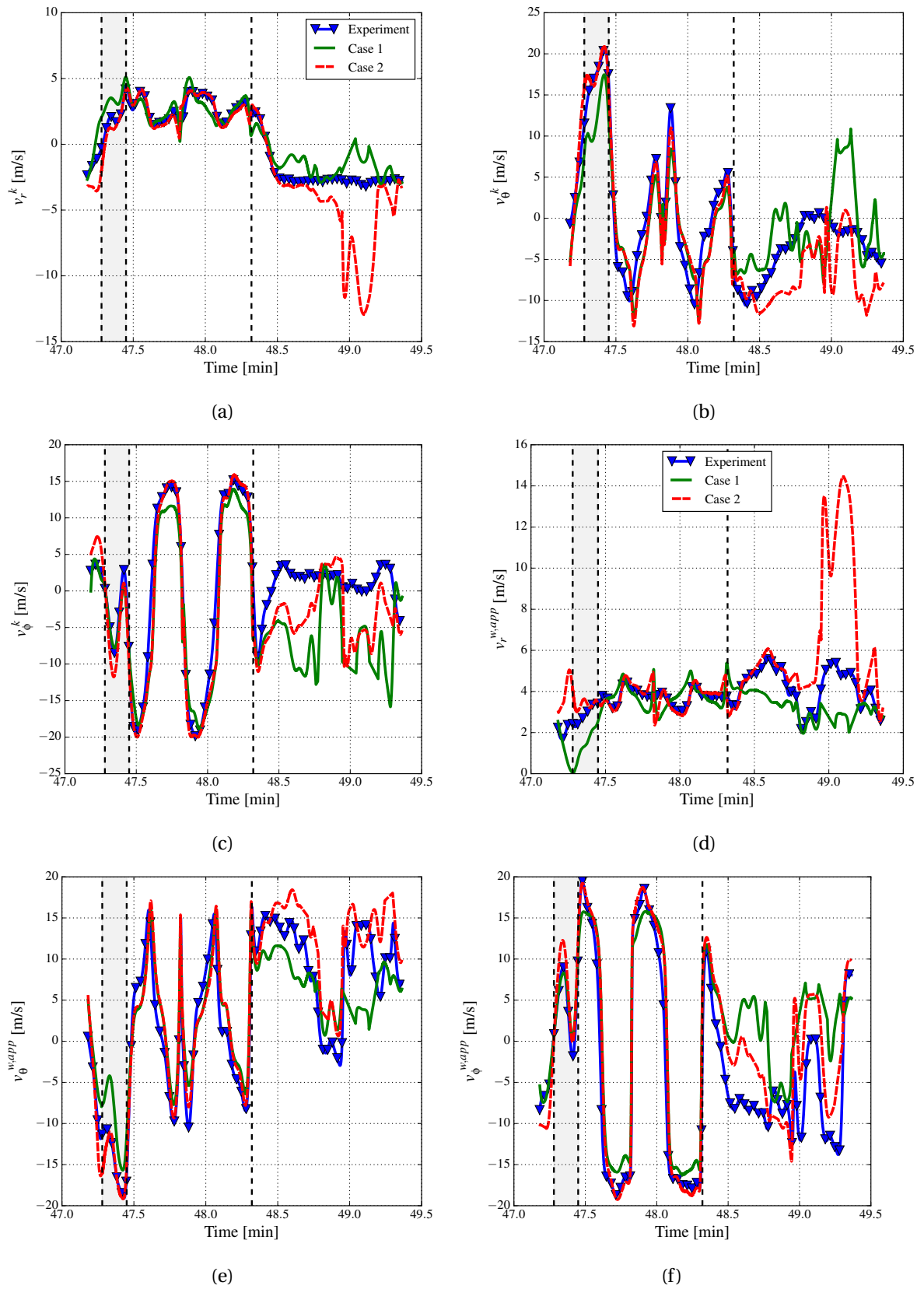


Figure 4.8: Components of the kite ground and apparent speed w.r.t the ground station in spherical coordinates

Fig. 4.9 shows a) the norm of the kite ground speed, b) apparent wind speed, and c) the mechanical power of the cycle. As expected, the ground and apparent speeds are close to the experimental values during traction phase, obtaining more accurate results from the case two than with the generic aerodynamic coefficients. Furthermore, none of the cases can predict the apparent wind speed during retraction, yet case two can follow the trend of the kite speed during the same phase. Overall, the power during transition and traction phase matches fairly well, following the same tendency as the experimental results.

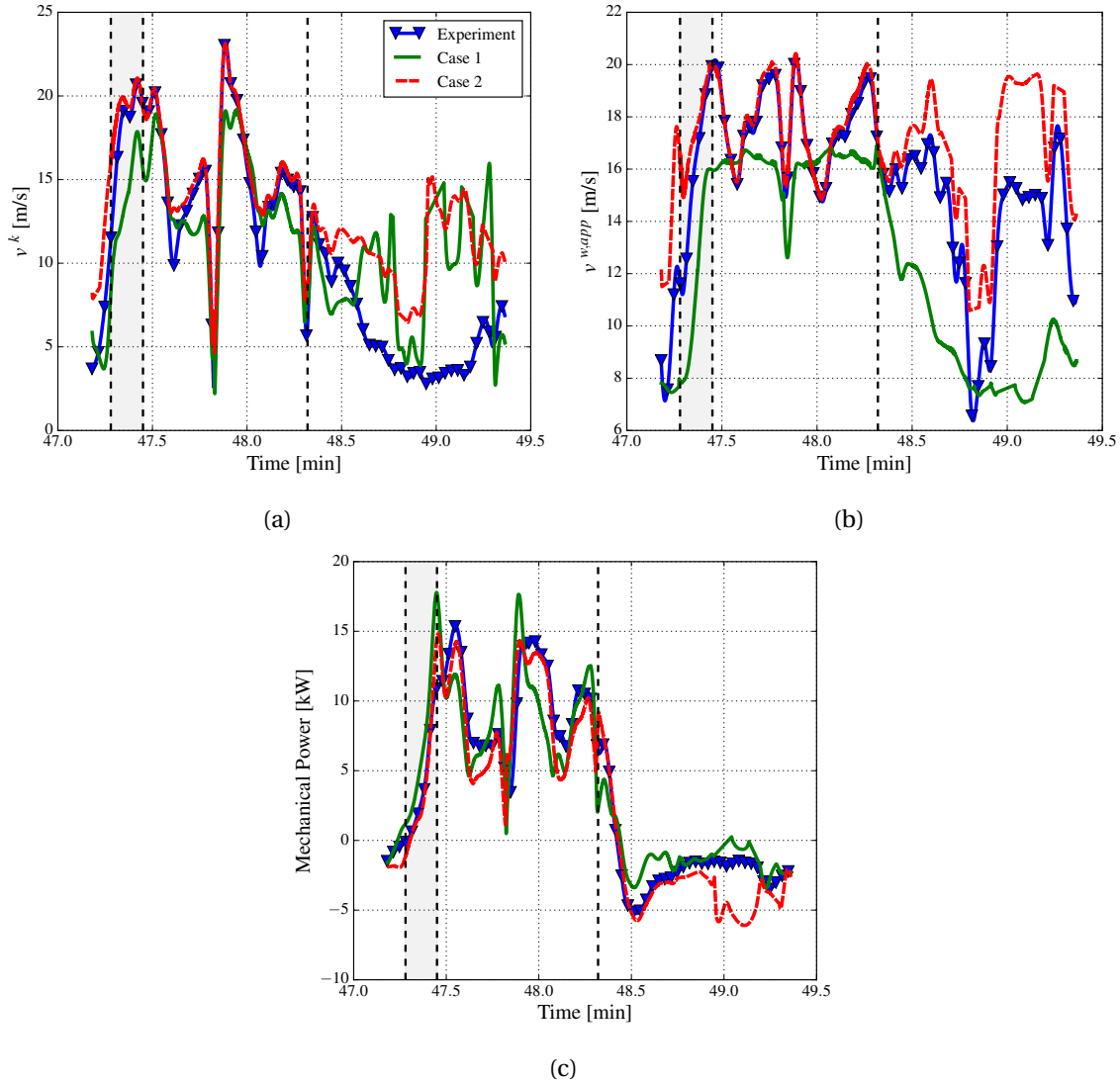


Figure 4.9: a) Kite ground speed, b) apparent wind speed and c) mechanical power

In the previous figures it has been consistently observed that, even if the derived aerodynamic coefficients are used, the retraction phase does not resemble the experiment. The reason for this is twofold: i) on the one hand the low apparent velocities during retraction tampered with the alignment between the pitot tube and the incoming flow, affecting the measurements of the dynamic pressure and, hence, the apparent velocity. On the other hand, ii) the low tension force during retraction allowed vibrations in the unit that distorted the angle and apparent speed measurements [43]. Thus, the derived quantities at low apparent speed and tether force - such as the aerodynamic coefficients and the wind speed - have a sizable uncertainty. The last reliable measurement during retraction phase has been obtained at 48.6 min with $C_L = 0.33$ and $C_D = 0.001$. Fig. 4.10 shows a) the

apparent wind speed, b) the kite speed and c) the mechanical power using the derived aerodynamic coefficients before 48.6 min and constant C_L and C_D after. It can be observed that just by using a good estimated constant value, the quasi-steady model can predict a more accurate retraction phase. Nevertheless, quantitative differences are still observed for the velocities.

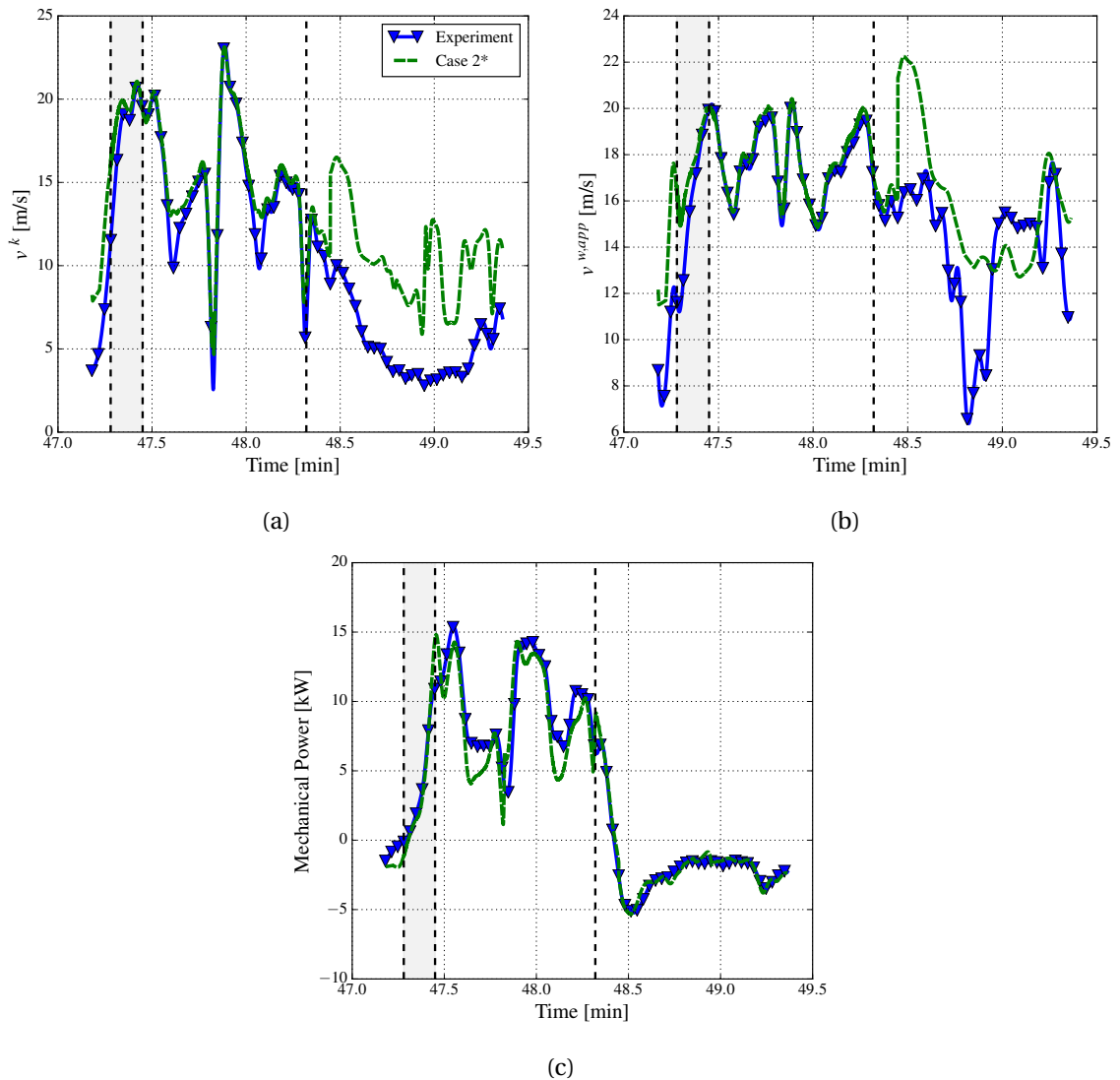


Figure 4.10: a) Kite ground speed, b) apparent wind speed and c) mechanical power for the case 2*

The velocity difference is explained with Fig. 4.11, which shows in Fig. a) the radial components of the apparent wind speed and in Fig. b) the tangential component. i) It can be seen that the radial apparent wind speed of case 2* matches fairly well with the flight data during the whole cycle. This explains the results of the mechanical power. However, ii) the tangential apparent wind speed in Fig b) does not match during retraction. The latter depends on the kite ground speed and the wind speed, yet only the second is an input in the model. Hence, the wind speed provided to the model does not represent the environmental conditions at this moment, produced by the measuring problems encountered during retraction.

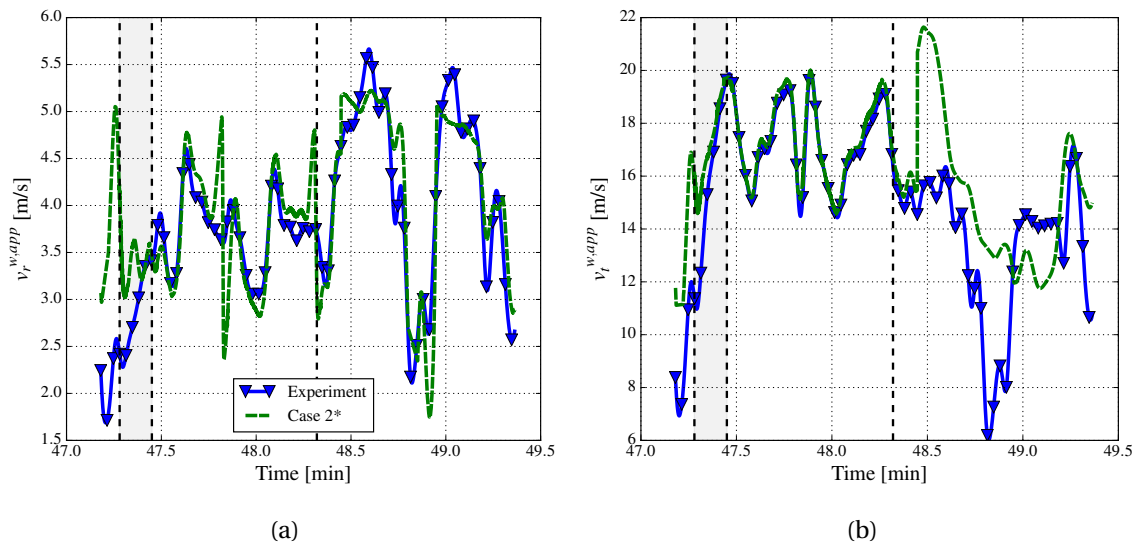


Figure 4.11: Apparent wind speed in a) radial and b) tangential direction during the cycle for case 2*

4.4. CHAPTER CONCLUSIONS

A validation of the quasi-steady model was conducted using the experimental data from Oehler [43]. The trajectory, environmental conditions and tether ground force were used as inputs to assess the predicted mechanical power, and kite velocities. Two different set of aerodynamic coefficients were used to evaluate their sensitivity on the desired quantities. From the results, it can be concluded that i) the quasi-steady model can accurately predict the transition, traction, and retraction phases if the correct geometry, aerodynamic coefficients, and wind conditions are provided. Moreover, ii) if the exact aerodynamic coefficients are not known, the use of generic coefficients can still provide a reasonable estimate of the performance of the system. iii) The aerodynamic coefficients and the angle of attack of the kite are the most sensitive parameters and should be studied in depth in future research. Finally, due to the positive results of the validation, the quasi-steady model will be used in the following chapters.

5

CONTROL AND PATH PLANNING

Suitable control and path planning strategies are required for the kite to fly smoothly and stable. The present chapter is intended to detail both approaches. Broadly speaking, the kite is commanded using the course angle calculated with a hierarchical control, while the trajectory is defined by three points that, depending on the phase, indicate the heading to the controller.

5.1. CONTROL STRATEGIES

A normal kite can be controlled using a) roll, b) yaw or c) pitch movements. a) Roll is usually used in two line kites, where one side is pulled to produce a rotation on the kite. b) Yaw control is typically used in four line kites, where the back lines are increased/decreased. The deformation produces a change in the angle of attack plus a misalignment of the resultant aerodynamic forces, forcing the kite to yaw. c) Finally, the pitch control is used to change the angle of attack of the kite, used to decrease the force during retraction or increase the aerodynamic forces during traction. Fagiano [19], Houska and Diehl [27], Wood et al. [56], among others, use roll controlled kites, while Jehle and Schmehl [32], Michael and Hans [41] use yaw controlled wings. Since Kitepower B.V. uses the second strategy, a proper yaw control must be employed in the simulations. The following subsections first derive the turn rate law and later describe the chosen controller.

5.1.1. TURN RATE LAW

The manoeuvrability of a yaw controlled kite is given by its capacity to change the heading χ , calculated as the summatory of the side aerodynamic forces $\vec{F}^{k,aer} \cdot \vec{e}_y$ and the gravitational force contribution $\vec{F}^{k,g} \cdot \vec{e}_y$. Hence,

$$\sum \vec{F} = \vec{F}^{k,aer} \cdot \vec{e}_y + \vec{F}^{k,g} \cdot \vec{e}_y = mR\dot{\chi}^2, \quad (5.1)$$

where R is the radius of the turning circle, and $\dot{\chi}$ is the turn rate. Both are sketch in Fig. 5.1.

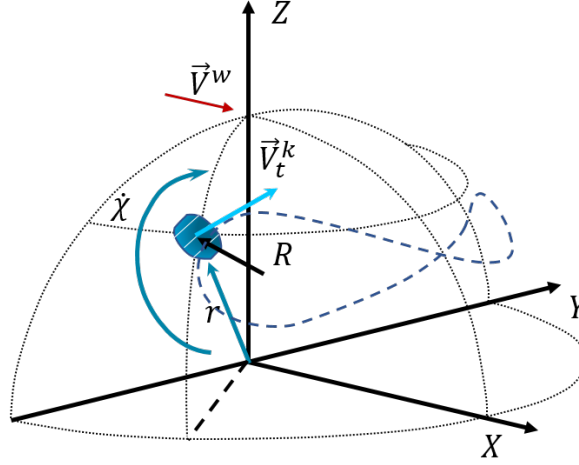


Figure 5.1: Turning rate law sketch

As described by Michael and Hans [41], the side aerodynamic force can be assumed linearly dependent on the steering input u'_s , as

$$\vec{F}^{k,aer} \cdot \vec{e}_y = (\vec{F}_{left}^{k,L} + \vec{F}_{left}^{k,D} + \vec{F}_{right}^{k,L} + \vec{F}_{right}^{k,D}) \cdot \vec{e}_y = c v_a^2 u'_s, \quad (5.2)$$

where c is a constant that relates the steering with the side aerodynamic forces. Furthermore, the gravitational component in \vec{e}_y is dependent on the elevation and heading of the kite, as

$$\vec{F}^{k,g} \cdot \vec{e}_y = m \vec{g} \cdot \vec{e}_y = mg \cos \beta \sin \psi. \quad (5.3)$$

Even further, the definition of the kite tangential velocity can be used $v_t^k = \dot{\chi} R$. Thus, eq. (5.1) becomes

$$\begin{aligned} m v_t^k \dot{\chi} &= c (v^{w,app})^2 u'_s + mg \cos \beta \sin \psi, \quad \text{and} \\ \dot{\chi} &= C_1 \frac{(v^{w,app})^2}{v_t^k} u'_s + \frac{g}{v_t^k} \cos \beta \sin \psi \end{aligned} \quad (5.4)$$

Finally, it can be assumed that the kite velocity is much greater than the wind speed, $v^k \gg v^w$, and that the kite radial component is much smaller than the tangential components, $v_t^k \gg v_r^k$. Then, the apparent speed is approximately equal to the kite tangential speed, $v_t^k = v^{w,app}$. Hence, the final turn rate law is given by

$$\dot{\chi} = C_1 v^{w,app} u'_s + \frac{C_2}{v^{w,app}} \cos \beta \sin \psi, \quad (5.5)$$

where the constants C_1 and C_2 are unique for each kite and need to be experimentally determined. It can be inferred that, for the controller to have good performance, the apparent wind speed must be accurately measured during flight. Eq. (5.5) is equivalent to the steering force used by the extended point-mass model of eq. (3.50) and can be utilized directly in the quasi-steady model.

5.1.2. HIERARCHY CONTROL

The selected controller has been originally proposed by Jehle and Schmehl [32], aiming to control the heading of the wing. To predict the required turn rate $\dot{\chi}$, the error between the desired χ_{set} and the current course angle χ is used. Then, a modified version of the turn rate law relates the course rate with the required steering input.

At each time step, the desired bearing is calculated using great circle navigation, i.e. the shortest path between two points in a sphere, with

$$x = \beta_{set} - \beta, \quad (5.6)$$

$$y = (\phi_{set} - \phi) \cos \beta, \quad \text{and} \quad (5.7)$$

$$\chi_{set} = \arctan \frac{y}{x}, \quad (5.8)$$

where β_{set} and ϕ_{set} are the components of the desired waypoint. Then, the attitude is calculated as

$$\dot{\chi} = \chi_{set} - \chi. \quad (5.9)$$

Finally, the required steering input is obtained by linearizing the turn rate law derived in the previous section. Hence,

$$\dot{\chi} = C_1 v^{w,app} u'_s + \frac{C_2}{v^{w,app}} \cos \beta \sin \psi \quad \text{and} \quad (5.10)$$

$$u_s = K_p \frac{1 + K_{d,s} u'_d}{C_1 v^{w,app}} \left(\dot{\chi} - \frac{C_2}{v^{w,app}} \cos \beta \sin \psi \right) + u_{s,0} \quad (5.11)$$

with

$$u'_s = \frac{u_s - u_{s,0}}{1 + K_{d,s} u'_d}. \quad (5.12)$$

This formulation of the turn rate law has been presented in Fechner et al. [22] to account for imperfections in the bridles and deformations due to the depower input. The coefficient $u_{s,0}$ takes into account miss-matches between both sides of the bridle, while, $K_{d,s}$ accounts for the coupling effect of the depower and the steering (see Fig. 2.8). Furthermore, K_p is the proportionality constant used in each phase.

Limits for the heading rate $\dot{\chi}$, the steering input u_s , and the apparent wind speed $v_{w,app}$ have been included to avoid non-physical behaviour or mathematical inconsistencies. The limits have been taken from [21].

Finally, to model the KCU, the rate of change of the steering inputs \dot{u}_s and depower inputs \dot{u}_d have been limited to 0.3 s^{-1} and 0.2 s^{-1} , according to the results obtained by [21]. The final controller is shown in Fig. 5.2.

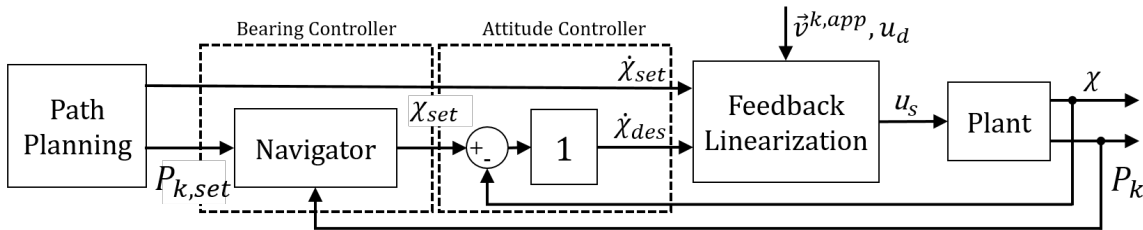


Figure 5.2: Hierarchical kite course control, adapted from [32]

5.2. PATH PLANNING

The trajectory of the kite, as previously mentioned, is divided into three phases: traction, retraction, and transition. In general, each stage is composed by a start condition; a depower input; a desired ground tether force; and at least one way-point used by the controller to calculate the set heading. The online optimizer that will be discussed in the next chapter aims to address the last two. Hence, the start and depower conditions must be selected appropriately to allow a soft transition between the phases. In order to obtain a stable and reliable flight during the whole trajectory the present section describes i) the start of each stage, ii) the transition phase and iii) the definition of the figure of eight. The set ground tether force will not be dealt in this section since, as part of the optimisation, it will be discussed in chapter 6.

5.2.1. PHASE START

The possible options, advantages and disadvantages for the start of each phase are the following:

- **Retraction:** the reel in phase should start when the desired maximum tether length is reached; however, this does not guarantee an optimal transition between phases. The orientation of the kite during traction phase plays a crucial role. If the heading is aligned with the retraction way-point, the retraction will be faster since the kite does not need to adapt to the new trajectory. Further, if the retraction starts as soon as the tether length is reached, the forces at the kite will still be high, forcing the winch to continue reeling out and producing overshoots of the tether length. Thus, the retraction is allowed to start when i) the tether length is above 98% of the maximum tether length and ii) the heading angle is pointing between $\pm 10^\circ$ to the way-point. As safety, if these conditions are not met when the maximum tether is reeled out, the retraction phase is forced to occur.

To decrease the aerodynamic forces, as soon as the retraction starts the depower input is increased to the pre-defined levels. The speed at which the kite is depowered is given by the properties of the KCU, specifically the communication time of the signals and the speed of the motors. The depowering time provides two additional advantages: a) the system can still produce energy during retraction and b) the speed is used to move the kite out of the centre of the wind window, decreasing the overall retraction time. Finally, one waypoint is used during retraction to indicate the heading to the controller. The waypoint is constantly updated during retraction, aiming to the closest side. Hence, the retraction can start aiming to (θ_R, ϕ_R) , yet if during the retraction the nearest waypoint is $(\theta_R, -\phi_R)$, the point is updated.

- **Transition:** when the tether is i) completely reeled in, the transition phase begins to redirect the kite to the centre of the wind window. As soon as the transition starts, the depower input is decreased, increasing the angle of attack and, thus, the aerodynamic forces. Additionally, the desired waypoint is updated to the centre of the figure of eight.
- **Traction:** to correctly start the traction without producing deformed figures, the orientation of the wing has to be controlled slightly before the transition waypoint is reached. Hence, i) the traction start when the kite is located inside a circle formed by P_{centre} and the radius ϕ_∞ . The depower is maintained at the same minimum level set during the transition phase and is constant throughout the entire phase.

Fig. 5.3 shows a sketch of a trajectory, where P_R is the retraction waypoint, and P_+ and P_- are the traction waypoints. Tab. 5.1 shows a summary of the start conditions for each phase.

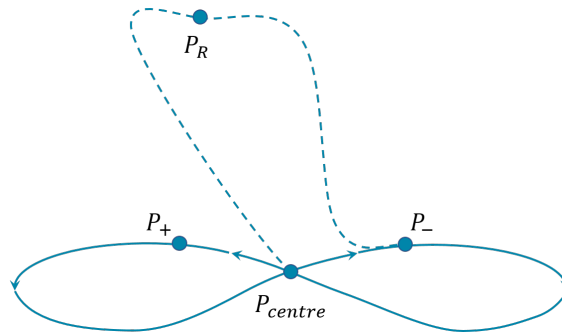


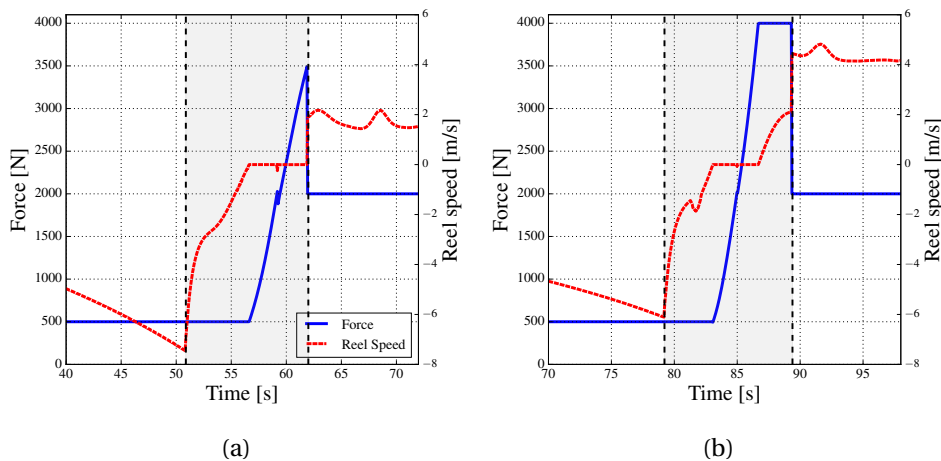
Figure 5.3: Path planning of the pumping kite

Phase	Start	Depower Input	Initial Way-point
Retraction	$r > 0.98r_{max}$ and $\chi \approx \chi_{des,P_1}$	$u_{d,max}$	$P_{set} = (\theta_R, \pm\phi_R)$
Transition	$r < r_{min}$	$u_{d,min}$	$P_{set} = P_{centre}$
Traction	If $ P^k - P_{centre} < \phi_\infty$	$u_{d,min}$	$P_{set} = \begin{cases} P_-, & \phi > 0 \\ P_+, & \phi < 0 \end{cases}$

Table 5.1: Start, depower input and initial way-point for each phase

5.2.2. TRANSITION CHARACTERISTICS

In addition to positioning the wing at the desired location, the transition is used to increase the tether force. During retraction phase, the ground force is set at a minimum to manoeuvre the kite. When the retraction finishes, the apparent wind speed responsible for the aerodynamic forces comes, mainly, from the reeling speed. Thus, to decrease the reel speed, the aerodynamic coefficient of the aircraft is increased by increasing the angle of attack while keeping the ground tether force constant. When the reel in speed is zero, the ground force is allowed to increase up to the maximum design force, maintaining the length of the tether constant. If the ground force is above the maximum design force, the winch reels out the tether, producing a slight amount of electricity and maintaining the force at its maximum.

Figure 5.4: Force and reel speed at v_R^w a) 6 m/s and b) 8 m/s. The transition phase is shown in gray.

As an example, Fig. 5.4 shows the ground force and reeling speed before, during and after the transition phase for v_R^w equal to a) 6 m/s and b) 8 m/s. Both cases start at the minimum force of 500 N at retraction, reaching high reeling speeds just before the transition phase. At the transition,

the tether force is maintained constant, while the reel speed decreases by increasing the aerodynamic forces. When the reel speed is zero, the ground forces start to increase up to the maximum design force, reached only by Fig. b). When transition finishes, the force is set equal to the desired traction force, in this case, 2000 N.

5.2.3. FIGURE OF EIGHT

A simple figure of eight is defined by two conditions, an inner figure condition to follow a waypoint and an outer figure condition to turn with a set turn rate. Fig. 5.5 shows a descriptions of the trajectory for down loops. In the figure, it is seen that if the azimuth position of the kite is outside ϕ_+ and ϕ_- , the controller commands the kite to turn with the set steering rate, while if the azimuth position is inside P_+ and P_- the kite flies to the opposite direction [20].

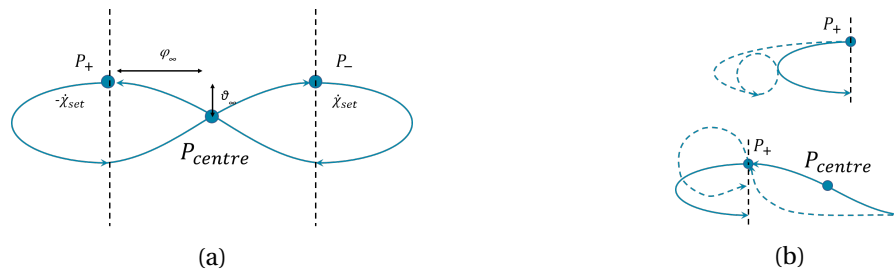


Figure 5.5: a) Waypoints and description of the figure of eight and b) problems of the simple description

This loose description of the figure has two main disadvantages. both are sketched in Fig. 5.5b). The upper figure shows that if the kite does not reach the inner position after turning, the kite will continue to turn indefinitely. The problem may arise due to a delay in communication with the kite, a slow reaction of the steering or due to an excessive heading rate. Furthermore, the lower figure shows that some heading angles can produce inconvenient turns, increasing the turning time or not following the desired path. The problem may arise by a slow controller or at low wind conditions when steering is limited.

To overcome the first condition the orientation of the kite is used to update the new waypoint after turning. Hence, when the kite is turning in the outer part of the figure, the waypoint is updated when the heading changes signs. Furthermore, to overcome the second condition, the turn action at the sides of the figure is started slightly before P_- and P_+ . In theory, the latter condition could also compensate for the first drawback, yet, in practice, some cases could occur when the problem persists. Fig. 5.6 left sketches the final figure of eight, while Tab. 5.2 presents a summary of the conditions.

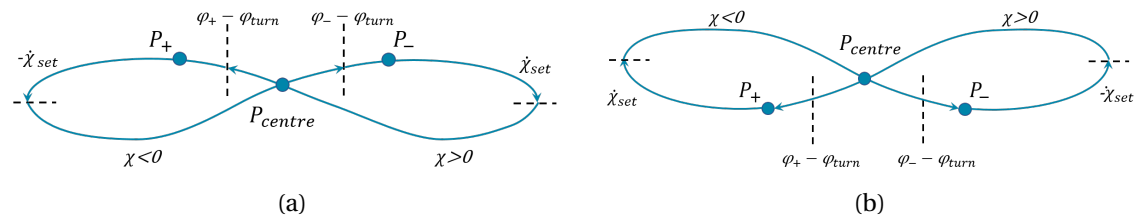


Figure 5.6: a) Down and b) up loop description for the figure of eight

In Fig. 5.6, the kite turns from $\phi_+ - \phi_{turn}$ until the change of heading, indicated with an horizontal line. Then the waypoint is updated to P_- , and the process is repeated on the opposite side. The same description can be implemented for up loops by changing the turn direction, as shown in Fig. 5.6 a).

Condition	Action
$\phi \geq \phi_+ - \phi_{turn}$ and $\psi > 0$	$-\dot{\chi}_{set}$
$\phi > \phi_- - \phi_{turn}$ and $\psi < 0$	P_-
$\phi \leq \phi_- - \phi_{turn}$ and $\psi < 0$	$\dot{\chi}_{set}$
$\phi < \phi_+ - \phi_{turn}$ and $\psi > 0$	P_+

Table 5.2: Description of the figure of eight

The final model is sketch on Fig. 5.7.

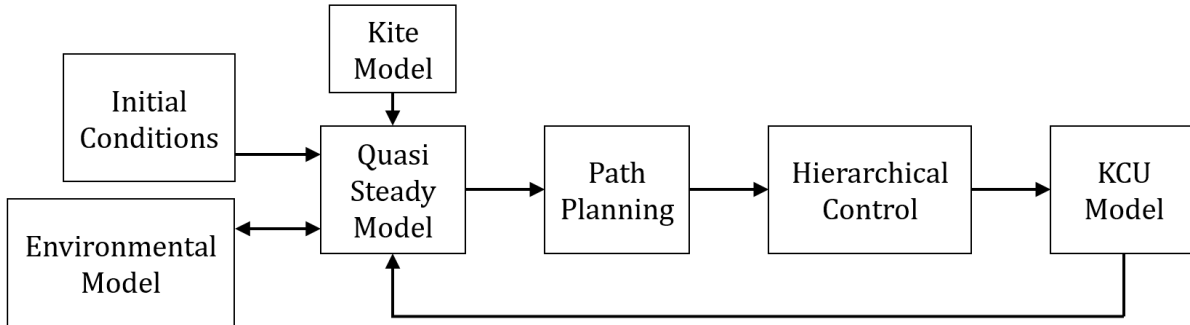


Figure 5.7: Sketch of the final model

5.3. KITE PROPERTIES AND SIMULATION RESULTS

Using the quasi-steady model, the discretized low fidelity model, the hierarchical controller, and the path planner strategy, the model is complete. The present section aims to demonstrate the capabilities of the simulation. The properties of the simulation can be seen in the following tables. The kite and tether characteristics have been taken from Fechner [21].

Property	Value	Property	Value
z_0	0.005 m	h_{ref}	6 m
v_{ref}	8 m/s	ρ_0	1.225 kg/m ³

Table 5.3: Environmental Conditions

Property	Value	Property	Value	Property	Value
Total area	14 m ²	Projected area	10.18 m ²	Kite mass	6.21 kg
α_0	10°	$\alpha_{d,max}$	35°	$K_{d,s}$	1.5
$u_{d,0}$	21.3 %	$u_{s,0}$	-0.0032 %	$u_{d,max}$	47.0 %
c_1	0.264 rad/m	c_2	6.27 rad m/s ²		

Table 5.4: Kite Properties

Property	Value	Property	Value	Property	Value
Diameter	4 mm	Mass per meter	0.013 kg/m	c_0	614600 N
d_0	473 Ns	r_{min}	250 m	r_{max}	400 m

Table 5.5: Tether Properties

Property	Value	Property	Value	Property	Value
KCU mass	8.4 kg	Max depower rate \dot{u}_d	0.2 s^{-1}	Max steering rate \dot{u}_s	0.3 s^{-1}

Table 5.6: KCU Properties

Property	Value	Property	Value	Property	Value
$u_{s,max}$	1	$\dot{\psi}_{max}$	$3.0^\circ/\text{s}$	P_{center}	$(25, 0)^\circ$
$(\theta_\infty, \phi_\infty)$	$(1.5, 10)^\circ$	P_R	$(90, 30)^\circ$	ϕ_{turn}	$0.25 \phi_\infty$
$v_{a,min}$	0.6 m/s	Δt	0.025 s	$K_{p,retraction}$	1.0
$K_{p,transition}$	1.0	$K_{p,traction}$	1.0	Set force traction	2000 N
Set force retraction	500 N	Max winch speed	10 m/s		

Table 5.7: Control Properties

The trajectory of the kite is shown in Fig. 5.8. The path corresponds to the second cycle of the simulation, using a constant θ_∞ and ϕ_∞ to generate the down figures of eight.

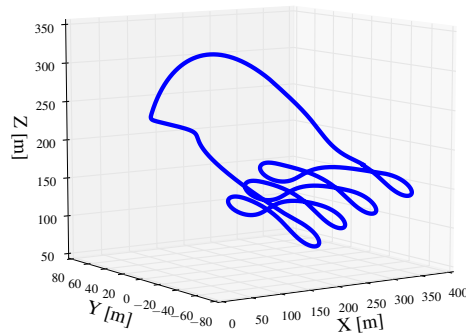


Figure 5.8: Trajectory of the kite

Fig. 5.9 shows a) the tether length, b) the path seeing from the side, and c) the elevation of the kite. From the Fig. a) it can be observed that i) the retraction started approximately at 400 m of tether length and maintained constant for approximately 10 seconds since the ground force is above the set retraction force. Moreover, when the cycle starts the transition phase, the tether length continues to decrease up to 240 meters. Hence, in both cases, less than 10 meters of overshoot is observed. ii) In Fig b) the distance covered by each figure became longer with higher radius. This is due to the greater reel out speed needed to maintain the tether force constant at higher wind speed. iii) In Fig. c) the elevation angle during traction respects fairly well the upper limit of $26.5^\circ (P_{center} + (\theta_\infty, \phi_\infty))$, while the minimum elevation increases since the kite can turn faster due to higher apparent velocities.

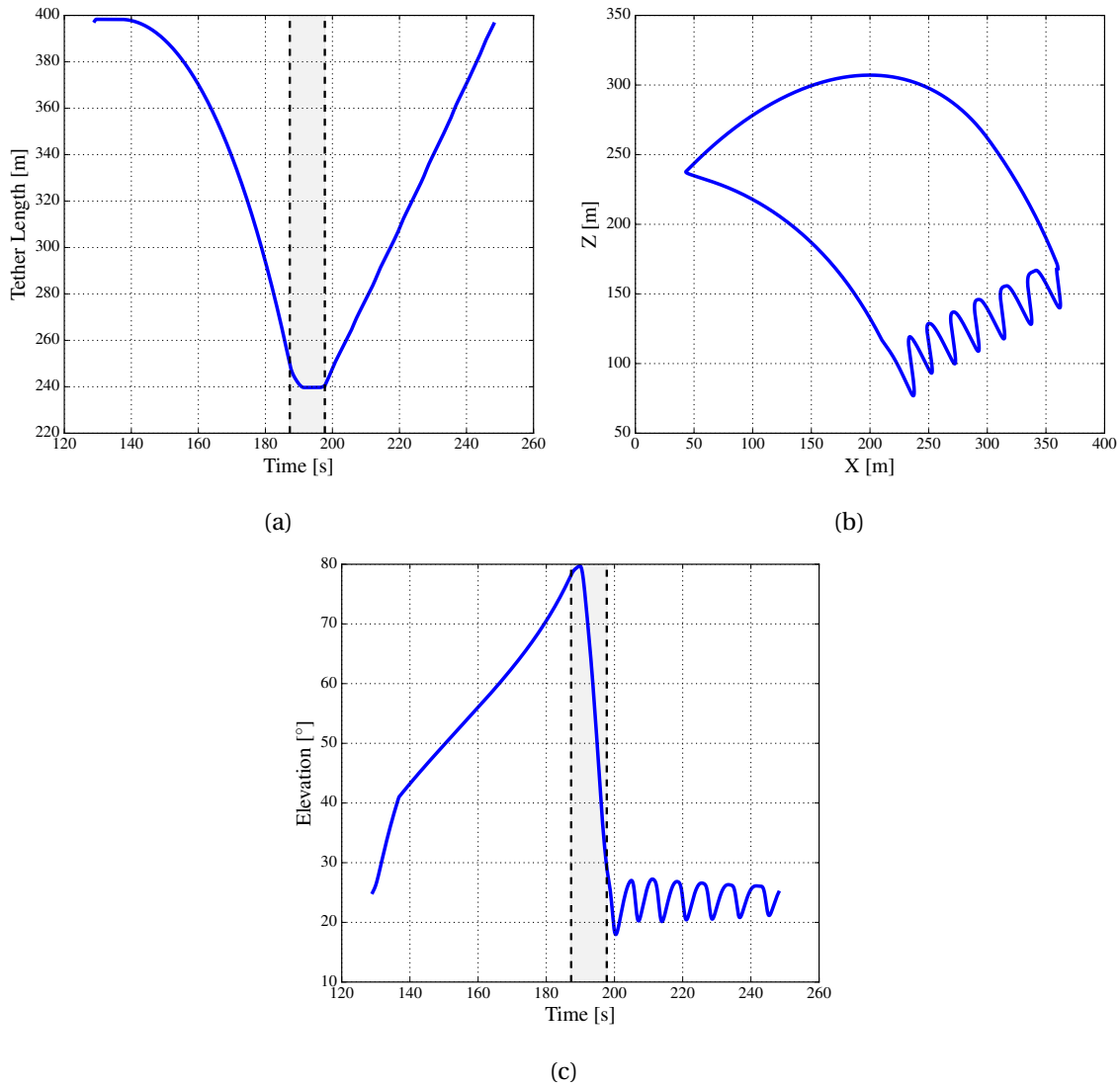


Figure 5.9: a) Tether length vs time, b) X vs Z, and c) elevation vs time. Transition phase in gray

Fig. 5.10 shows the a) apparent, b) tangential, and c) reel speed versus time. It is observed that i) the apparent and tangential speed are fairly similar, mainly differing during retraction. ii) The peak observed at around 190 seconds in the apparent and tangential speeds is due to the change in heading and the decrease of the reel in speed just after the transition starts. iii) The reel out velocity at around 130 and 195 seconds is zero, indicating that the force is between the predefined minimum and maximum values (see Fig. 5.11 a).

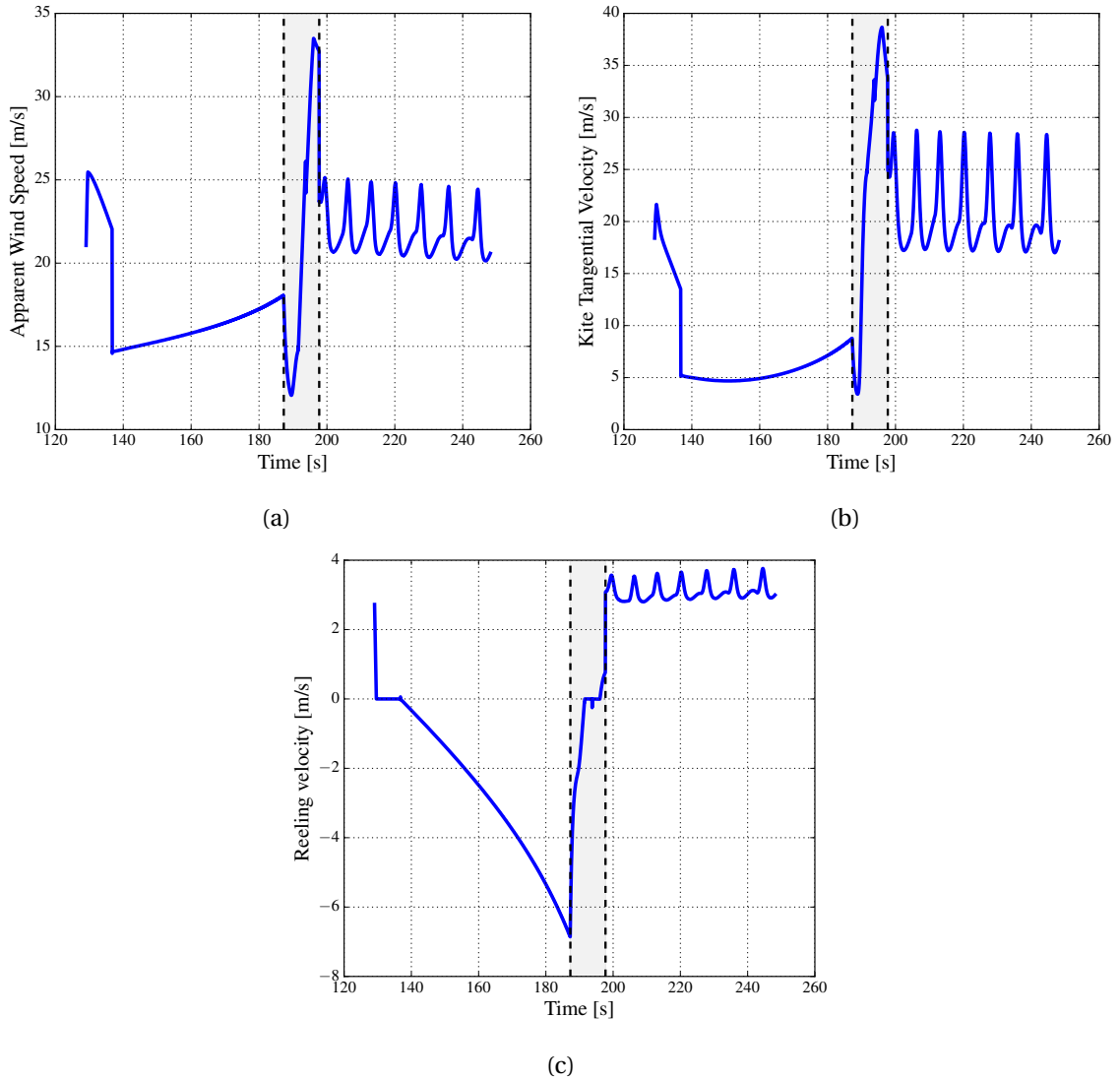


Figure 5.10: a) Apparent, b) tangential and c) reeling velocity over time

Fig. 5.11 shows a) the tether force, b) the mechanical power, and c) the angle of attack over time. As expected, i) the force is kept constant most of the time, except during the transition at around 190 seconds where it increases from the minimum to the maximum design value of 4000 N. ii) The mechanical power has the same shape as the reel velocity, given by eq. (3.46). iii) Fig. c) the inflow angle and the depower input are the main responsible for the behaviour of the angle of attack at the beginning of the retraction and transition, while along each phase the variation is solely produced by the first. iv) Two peaks can be observed in Fig c). The first occurs at the beginning of the cycle during retraction, and the second when the kite turns starts the transition phase. Both are produced by quick changes in the reel speed that influence the inflow angle.

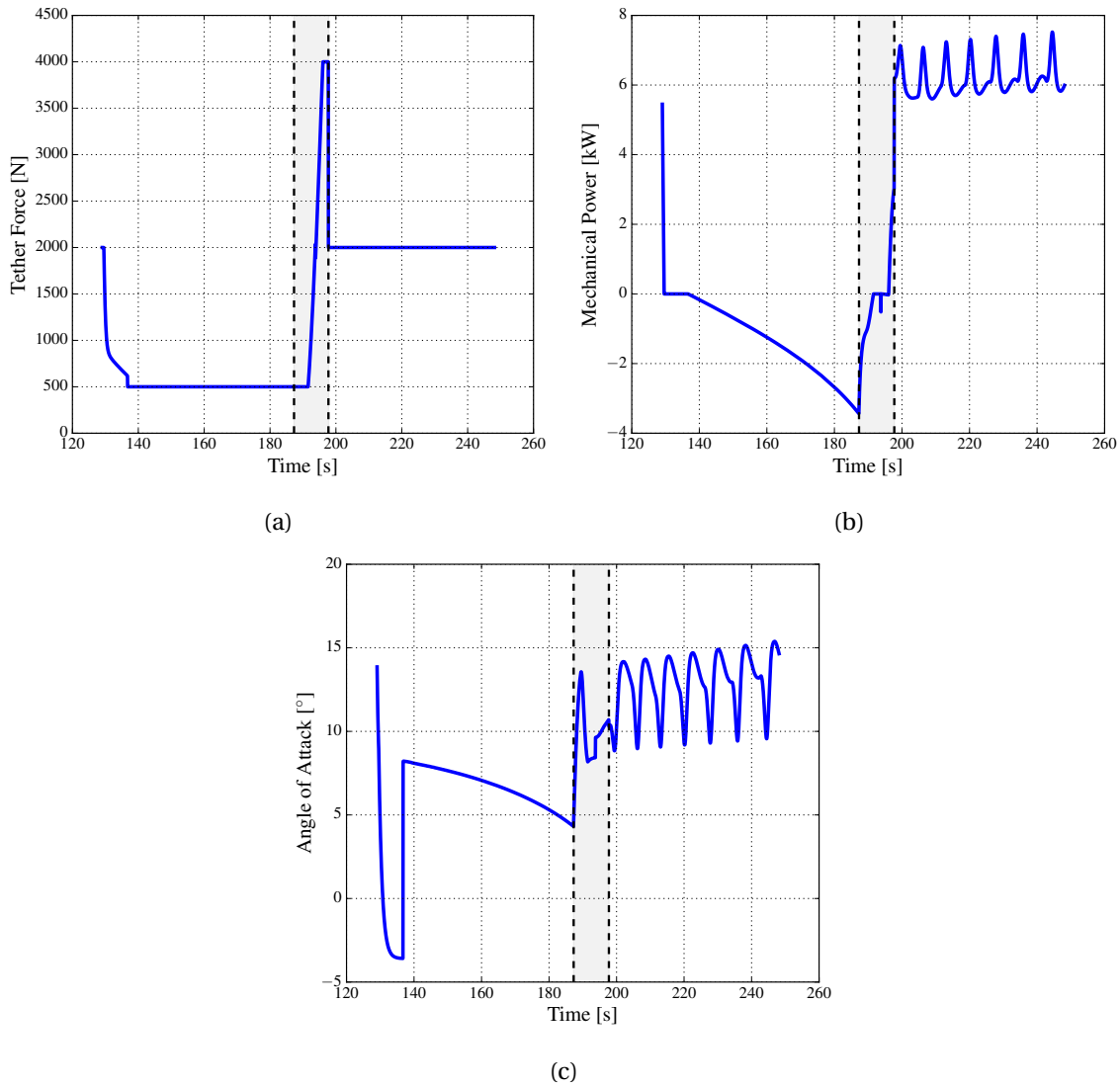


Figure 5.11: a) Force, b) mechanical power and c) angle of attack over time

Fig. 5.12 shows a) the lift to drag ratio, b) the steering input, and c) the depower input over time. i) Fig a) has the same behaviour as the angle of attack in Fig. 5.12 c), while the depower indicates the moments when the retraction and transition started. ii) Fig b) shows that the steering varies from, approximately, -0.4 to 0.4, given by the desired turning rate at the sides of the figure of eight.

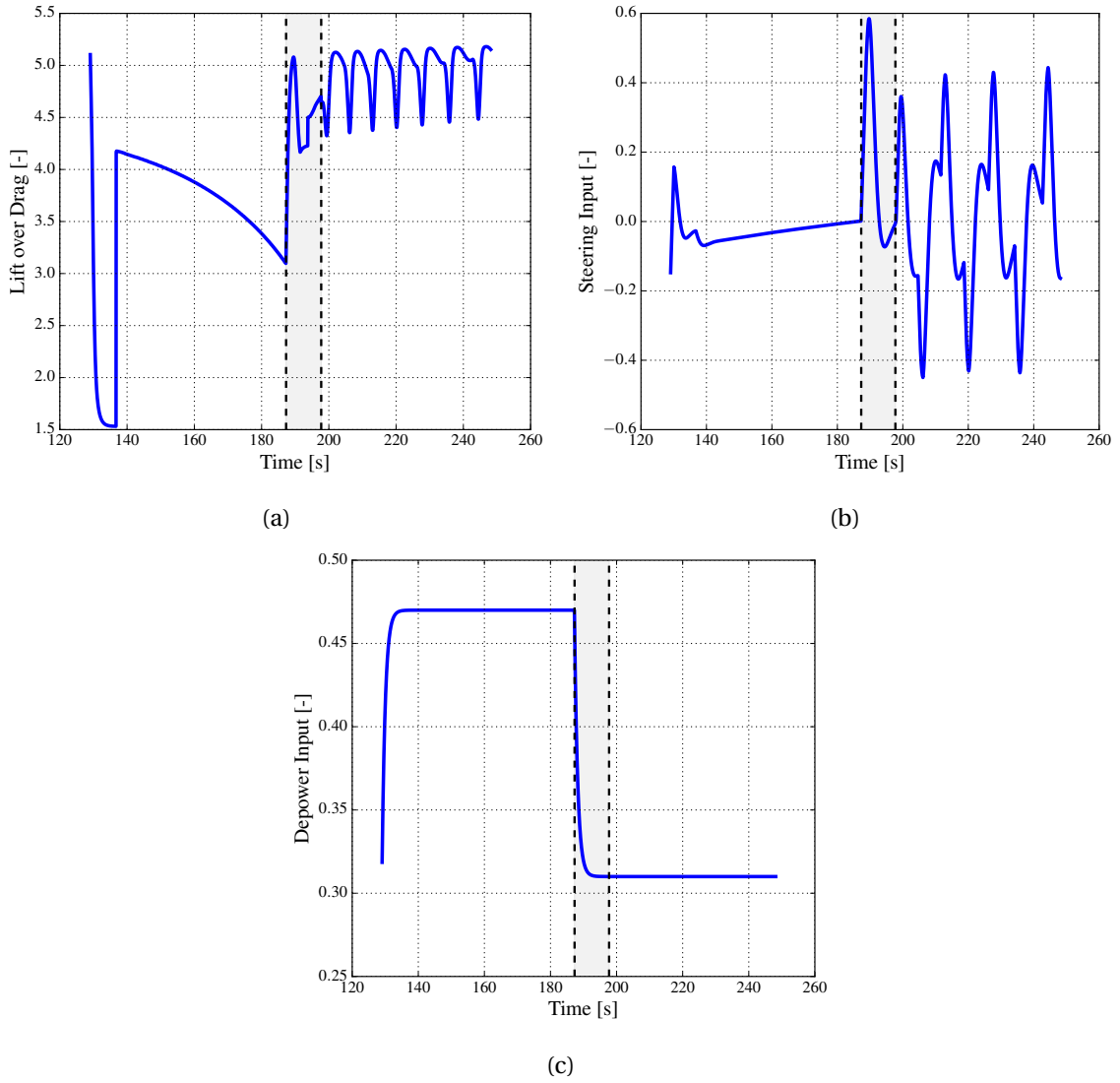


Figure 5.12: a) Lift to Drag, b) steering input and c) depower input over time

Finally, a summary of the mechanical power, required time, and energy produced during each phase has been included in Tab. 5.8.

Property	Value	Property	Value
Mean retraction power	-1.02 kW	Retraction time	77.48 s
Mean transition power	1.35 kW	Transition time	10.55 s
Mean traction power	8.76 kW	Traction time	37.69 s
Energy retraction	-78.74 kJ	Energy transition	14.14 kJ
Energy traction	330.0 kJ	Cycle net energy	265.46 kJ

Table 5.8: Mechanical power, duration and energy produced during the each phase

5.4. CHAPTER CONCLUSIONS

The control and path planning strategies were presented. i) For the control of the kite, the turn rate law has been used in a hierarchical control, relating the steering input with the heading rate of the kite. The controller was divided into three loops: bearing control, attitude control, and steering input. The first calculates the desired heading according to the set waypoint, the second calculates the difference between the current and the desired heading, while the third calculates the steering input. ii) The path planning was divided into three phases: traction, retraction, and transition. Each stage includes a start condition, a set force, a set depower, and at least one way-point. In total three waypoints are used to describe the full trajectory: a) the retraction way-point, b) the left and c) the right side of the figure of eight. Furthermore, iii) an improved description of the figure of eight was given using not only the azimuth position with respect to the centre of the figure but also the heading of the kite. Finally, iv) the first simulations of the developed were presented. The simulations show that if the constants that describe the steering capabilities of the kite are known, and the apparent speed is measured, the hierarchical controller can accurately and reliably manoeuvre the kite along the desired trajectory.

6

PATH OPTIMIZATION

Most of the path optimisation algorithms that have been described during the literature study create a specific trajectory depending on the wind speed. However, the direction and exact wind speed at the kite is, most of the times, unknown; limiting the performance of an offline optimisation. The online optimisation presented in this chapter aims to overcome these drawbacks by modifying the trajectory during flight. To do so, i) the measured power is used to optimise the traction phase and ii) the average power cycle is used to optimise the retraction phase. The chapter is organised into three main sections: i) traction mapping, ii) retraction mapping, and iii) the online optimisation. The first two sections are used to seek the desired characteristics that an optimal trajectory must have, while the third section describes the final optimizer. Throughout the chapter, the Hydra kite is used for the modelling, while the following common system and environmental conditions are used:

Condition	Value	Condition	Value
u_d	0.31/0.47	Minimum tether force	500
Maximum tether force	4000 N	Tether length	250 - 400 m
Reference wind	9 m/s	Reference Height	6 m
Roughness length	0.005 m		

Table 6.1: Flight conditions for the traction and retraction mapping

6.1. TRACTION PHASE MAPPING

To develop a reliable optimizer that can be used during flight, the desired characteristics and properties of the trajectory must be studied before hand. Hence, the present section aims to find the optimal path through the mapping of the power production in the wind window. The main advantage of mapping the wind window over other strategies, e.g. a genetic algorithm or a particle swarm, is that it allows to observe the sensitivity and the overall tendency of the results. Moreover, the offline mapping also serves as a benchmark to compare the final trajectory. The section is divided into four main subsections, aiming to analyse i) the instantaneous power production in the wind window, ii) the average power production in the wind window, iii) the shape of the figure itself and iv) the optimal force.

6.1.1. UNIDIRECTIONAL TRACTION MAPPING

Fig. 6.1 shows the instantaneous power production on a perfect crosswind flight, $\chi = 90^\circ$, at a radius of a) 250 m and b) 400 m. The figures have been obtained by modelling the crosswind flight with the quasi-steady model. Argatov et al. [5] produced similar results using an approximated power equation with constant aerodynamic properties. The tether force has been set equal to 3500 N.

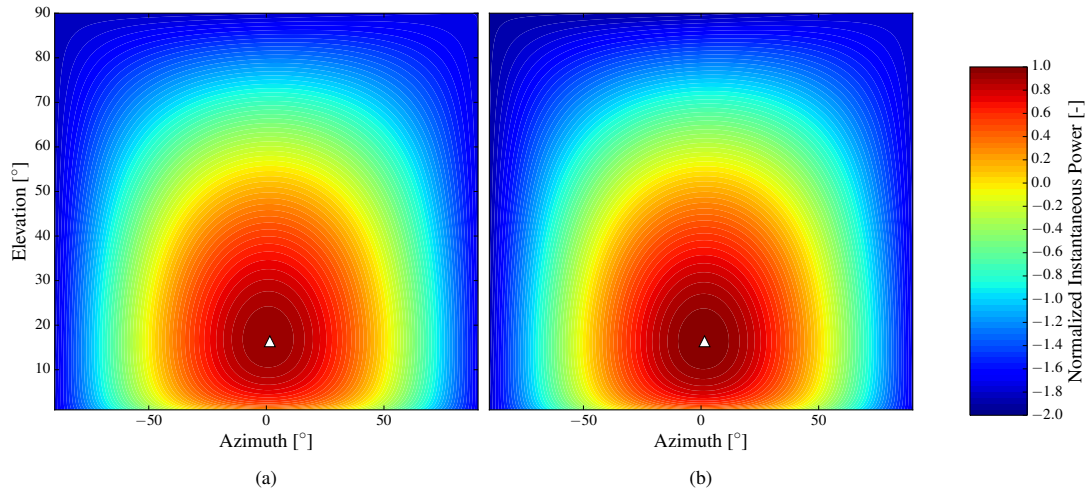


Figure 6.1: Instantaneous power production at a) 250 m and b) 400 m, the triangle shows the position of maximum power

Both figures show that i) there is an area in the wind window that maximised the instantaneous power. ii) The maximum instantaneous power is harvested when the kite is located at the centre of the wind window at a constant elevation of, roughly, 16° ; marked with a triangle. The elevation is produced due to the mass of the kite that misaligns the tether and aerodynamic forces [5, 38]. iii) The area of maximum power increases with the radius due to the increase in wind speed. iv) The area, however, is not symmetric to the centre of the wind window due to the wind direction w.r.t the kite. On one side the wind increases the apparent wind speed, while on the other it reduces it. This also explains the position of maximum power. v) Far from the centre, the instantaneous power becomes negative, indicating that the kite must be reeled in to maintain the force constant.

Finally, it can be inferred that a good power production is obtained if the trajectory of the kite is aligned with the wind direction and the elevation is kept constant. However, the figures do not provide any insights about the power production during the cycle since they only provide punctual information.

6.1.2. LISSAJOUS TRAJECTORY POWER MAPPING

To model the kite trajectory during the traction phase two options exist: 1) the control and path planning strategies developed in the previous chapter can be used or 2) the trajectory can be pre-define using, for example, the Bernoulli's lemniscate figure or the Lissajous' curve. The second option has been chosen, since by completely prescribing the trajectory possible limitations of the control strategy, the KCU, and the path planning can be avoided. Hence, the present section uses the Lissajous curve, defined as

$$\begin{aligned}\beta &= \beta_c \pm A_\beta \sin(2s), \quad \text{and} \\ \phi &= \phi_c + A_\phi \sin(s),\end{aligned}\tag{6.1}$$

where (β_c, ϕ_c) define the centre of the figure, (A_β, A_ϕ) define the height and the width, while $s = [0, 2\pi]$. A sketch of two trajectory can be observed in Fig. 6.2. The trajectories have been generated with $(\beta_c, \phi_c) = (16, \pm 10)^\circ$ and $(A_\beta, A_\phi) = (-1.5, 15)^\circ$.

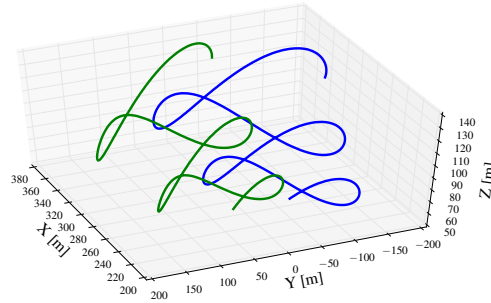


Figure 6.2: Quasi steady traction phase with Lissajous trajectory

Fig. 6.3 shows the normalized average power production given by

$$\bar{P} = \frac{1}{T} \sum_{i=0}^N P, \quad (6.2)$$

during traction phase. The trajectory has been prescribed with $(A_\beta, A_\phi) = (3.5^\circ, 20^\circ)$ and only the area close to the centre of the wind window is displayed.

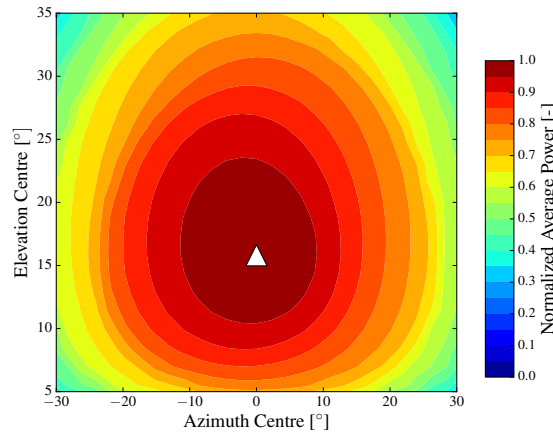


Figure 6.3: Traction phase average power using the Lissajous figure, $(A_\beta, A_\phi) = (3.5^\circ, 20^\circ)$

It can be seen that i) the maximum average power centre is located at zero azimuth and, roughly, 16° elevation. ii) The asymmetry between both sides is more notorious than in the unidirectional case. The reason is observed on Fig. 6.2: although both trajectories are identical, the left figure is perfectly aligned with the direction of the wind (X axis) during two and a half turns, while the right figure is only aligned during two turns.

To assess the sensitive along the maximum power centre, Fig. 6.4 shows the average power along the axis a) $\phi = 0$ and b) $\beta = 16^\circ$.

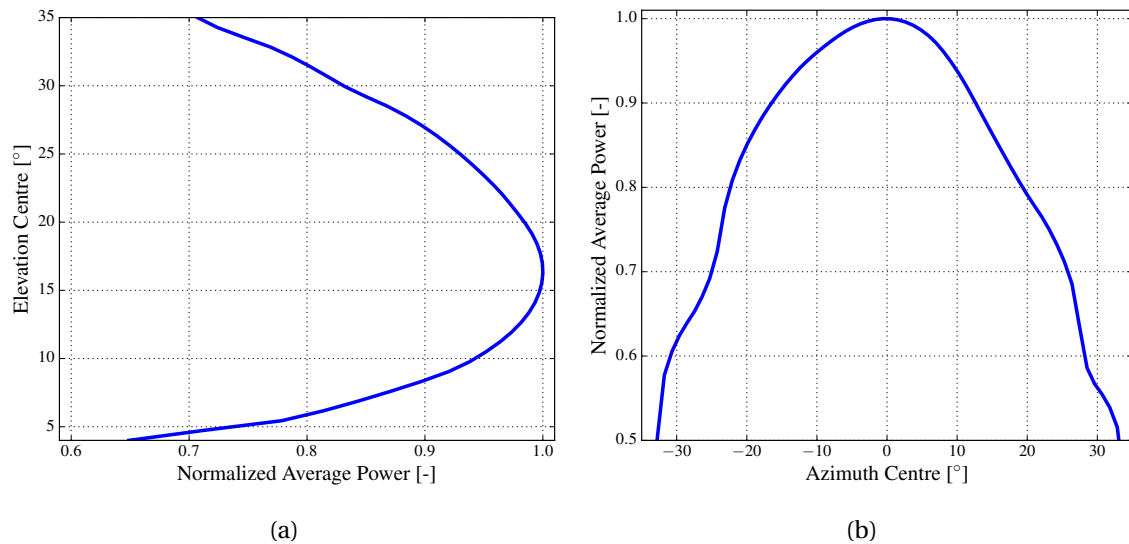


Figure 6.4: Variation of the average power along power centre in a) elevation and b) azimuth

The figures show that i) the misalignment in the elevation centre has an asymmetric effect, i.e. if the kite flights above the optimal elevation the power production will decrease slower than if the kite flights below it. ii) The misalignment in azimuth direction is also asymmetric. However, this is not only affected by the relative position with respect to the wind window, but also the width of the figure. iii) A misalignment of 5° , in the worst case, produces a 6% loss.

Finally, from the unidirectional power mapping and the average power mapping, it can be concluded that to maximise the power production, the online optimizer must seek the optimal azimuth and elevation angles.

6.1.3. LISSAJOUS TRAJECTORY LOOP ANALYSIS

The previous sections aimed to study the optimal location of the kite in the wind window. The present section aims to study the effects and the behaviour of the figure. In particular, four cases will be analysed: the width of the figure, the height of the figure, the direction of the turn, and a constant angle vs. constant width description of the Lissajous curve.

WIDTH OF THE FIGURE

To study the effect of the width A_ϕ , the traction phase has been mapped for four different cases. Fig. 6.5 shows the normalized average power for $A_\phi =$ a) 20, b) 15, c) 10 and d) 5° . The maximum value between the four cases has been used for the normalization.

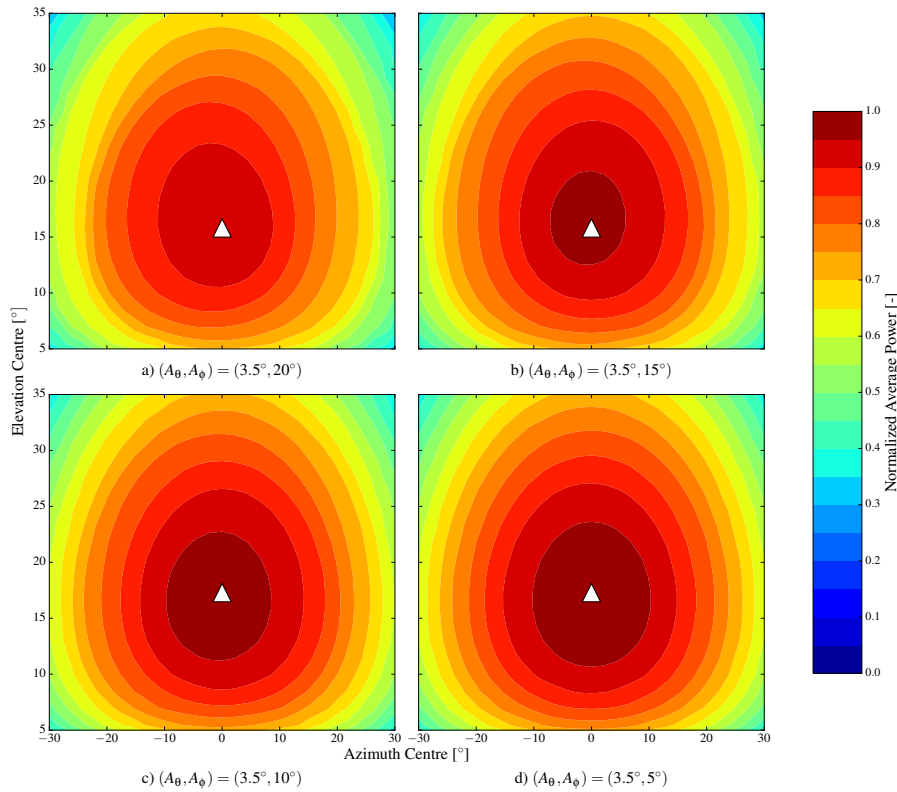


Figure 6.5: Normalized average power for $A_\phi =$ a) 20, b) 15, c) 10, and d) 5°

Three key findings can be stated. i) The power increases by decreasing the width of the figure since the kite spends more time aligned with the wind direction. Nevertheless, in reality, a limit given by the control unit, battery consumption, and steering capabilities of the kite must exist. This limit must be determined experimentally. ii) Narrower figures are less sensitive to the path itself, and its power production is more symmetric than wider figures. iii) The elevation of the maximum power centre decreases by reducing the width of the figure. This is driven by the instantaneous power production along the figure and the direction of the outer loops.

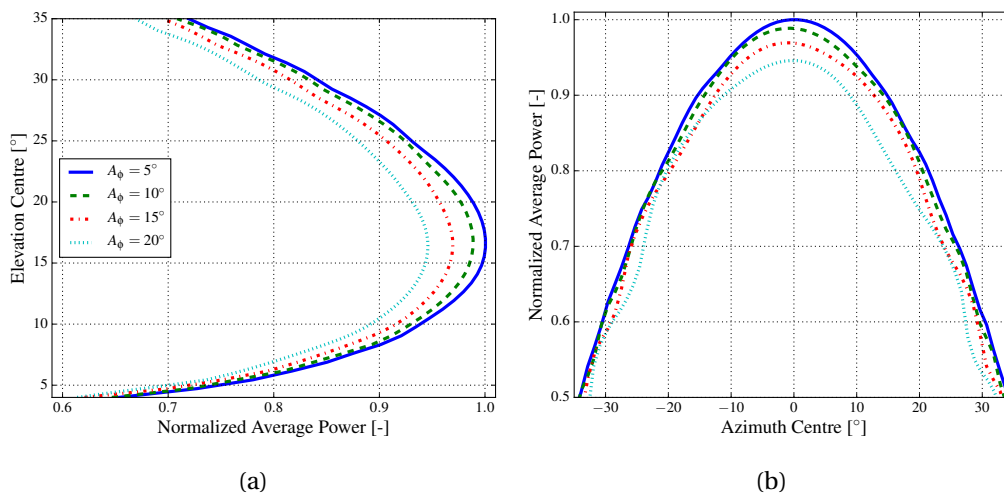


Figure 6.6: Variation of the average power along power centre in a) elevation and b) azimuth for different A_ϕ

Fig. 6.6 shows the average power along power centre for each trajectory. In Fig. a) it can be seen that the narrowest angle produces the highest power and the optimal elevation centre decreases along with the width angle. In Fig b) the variation over the elevation centre is still asymmetrical, yet less pronounced for smaller figures.

HEIGHT OF THE FIGURE

Similarly, as with the width, the wind windows has been mapped for four cases of A_β . Fig. 6.7 shows the normalized average power for a) 10, b) 7.5, c) 5 and d) 3.5° . Notice that the figures start at an elevation of 10.5° due to the ground clearance required for the first case.

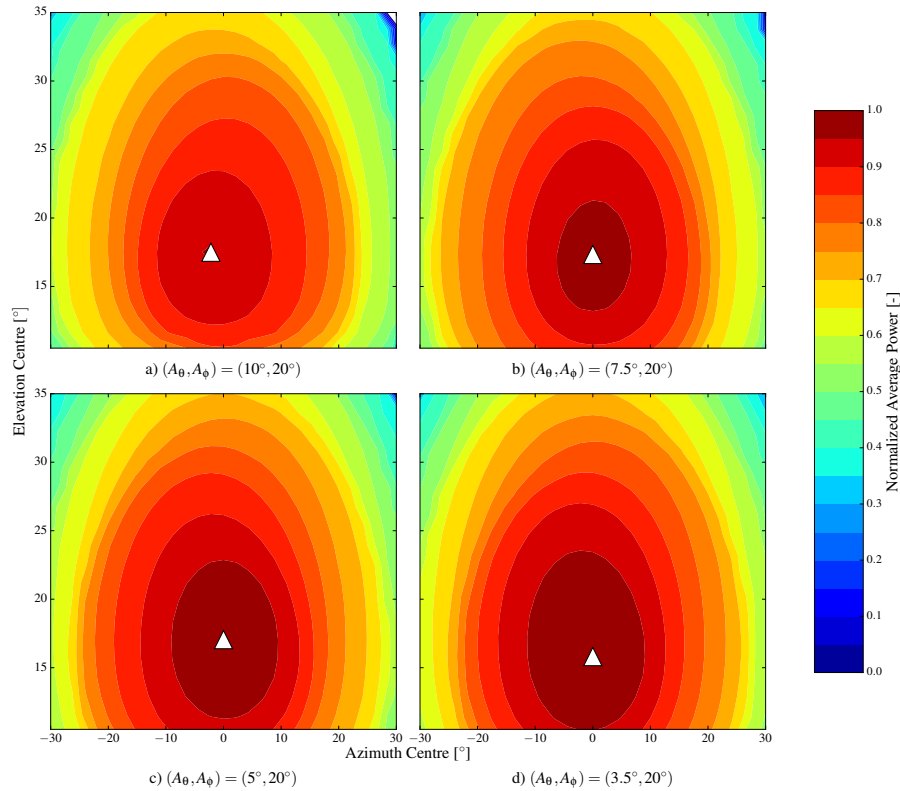


Figure 6.7: Normalized average power for $A_\beta =$ a) 10, b) 7.5, c) 5, and d) 3.5°

Similar conclusions as in the previous section can be obtained. i) An increase in the elevation height produces an increase in the elevation centre. Hence the shape of the figure affects the power centre. ii) The average power increases by decreasing the elevation height since the path is closer to the power centre. iii) The area of maximum average power increases by reducing the elevation height.

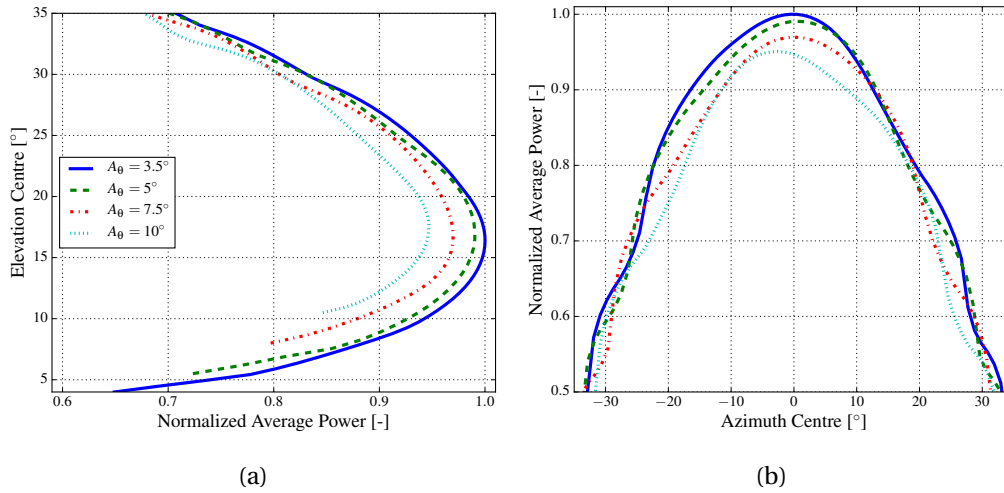


Figure 6.8: Variation of the average power along power centre in a) elevation and b) azimuth for different A_β

Fig. 6.8 shows the average power along the power centre for each trajectory. In Fig. a) the same behaviour as with the width is observed: the elevation centre decreases along with the height angle and a misalignment in the elevation centre has an asymmetrical behaviour. Differently, in Fig b) the average power does not become more symmetric by decreasing the size of the figure, this is due to the large width A_ϕ used for the modelling.

UP VS DOWN LOOPS

In addition to the height and width of the figure, the turn direction at the edges of the traction phase plays a major role in the manoeuvrability. Hence, it is important to study the difference between a down and an up loop. Two example traction phases have been simulated using $(\beta_c, \phi_c) = (16, 0)^\circ$ and $(A_\beta, A_\phi) = (3.5, 20)^\circ$. The flights only differ in the turn direction of the turning.

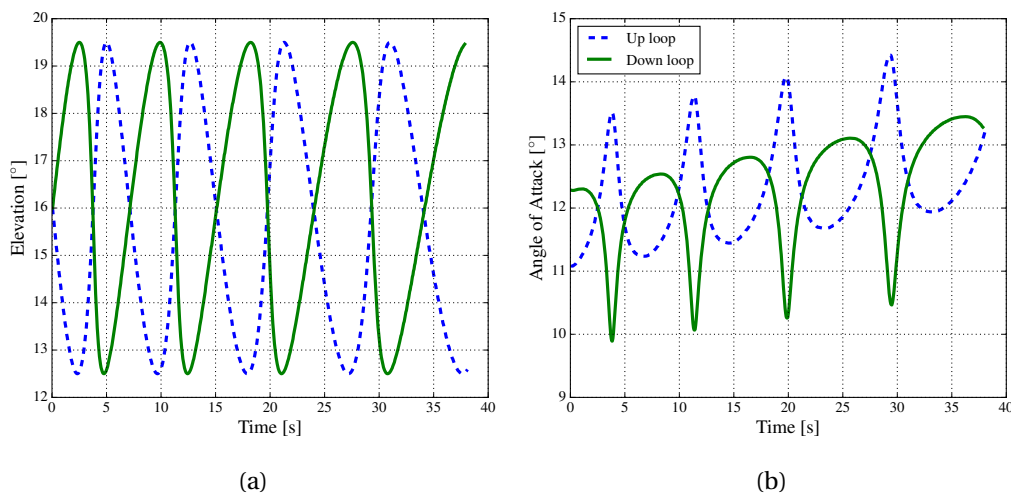


Figure 6.9: a) Elevation and b) angle of attack for up and down loops

Fig. 6.9 shows a) the elevation angle and the b) angle of attack of the kite versus time. It can be observed that i) in Fig. a) the elevation is periodic, yet the time required to perform a figure slightly increases over time. This is due to the angle definition of the Lissajous' curve that makes the kite fly longer distances at higher radius, as it can be seen in Fig. 6.2. ii) In Fig b) both angles

of attack increase each time the elevation increases. This is due to the gravity force that decreases the kite speed and increases the inflow angle [43]. As such, during the up cycles, the angle of attack increases by almost two degrees, while it decreases by the same quantity when flying down loops. Therefore, by flying down loops, the wing could fly at higher angles of attacks without reaching stall states.

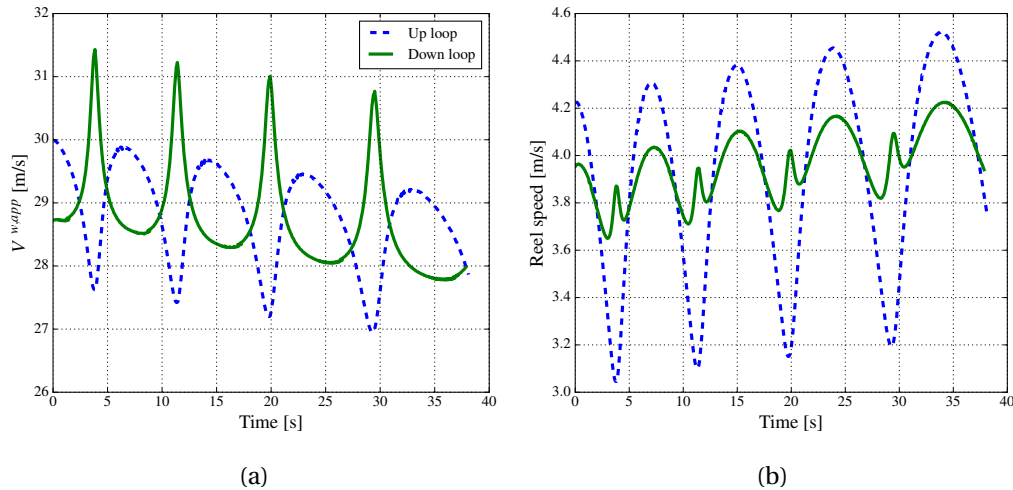


Figure 6.10: a) Apparent wind speed and b) reel speed for up and down loops

Fig. 6.10 shows a) the apparent wind speed and b) the reel speed of the kite versus time. It can be seen that i) as expected, the apparent wind speed decreases when flying up loops having the opposite effect of the angle of attack. As it has been explained in Section 5.1, the manoeuvrability of the kite is directly proportional to the apparent speed. Hence, the kite becomes less controllable when flying an up loop trajectory. ii) In order to maintain the force constant during the turn, the reel out speed for up loops decreases due to the increase in the angle of attack and aerodynamic forces. This is, however, highly dependent on the aerodynamic coefficients. iii) Finally, and as it can be seen in Fig. 6.11, the mechanical power fluctuates due to the reel out speed, increasing the wearing of the winch and generator.

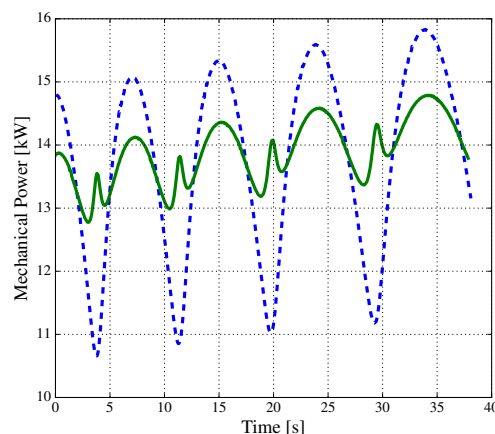


Figure 6.11: Mechanical power for up and down loops

It is worth mentioning that, by prescribing the figure, both cases finish the cycle at almost the same time, however, in a real flight this would not be the case. The lower apparent speeds reached during up loops tamper with the manoeuvrability of the kite, producing slower turns.

CONSTANT AZIMUTH ANGLE VS. WIDTH

The final information required to develop the online path optimizer is the width definition of the figure. Two options exist a) constant angle and b) constant width. To achieve a constant width, A_ϕ must be updated during flight such as to decrease the azimuth constant of the Lissajous figure. Fig. 6.12 shows an example traction path with constant azimuth angle and width.

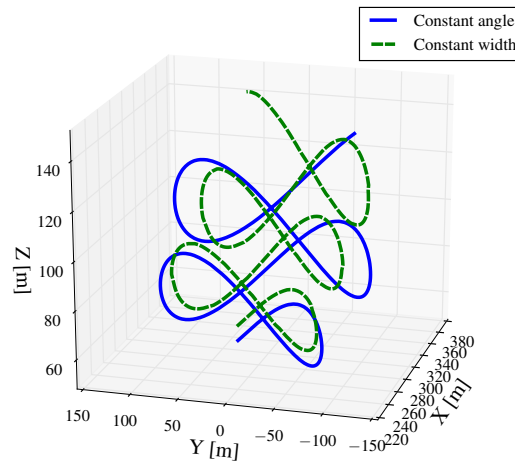


Figure 6.12: Constant azimuth angle and length for the traction trajectory

To compare similar trajectories, the width of the figure has been taken from the first loop of the constant angle definition. The mapping of normalised average power in the wind window is shown in Fig. 6.13.

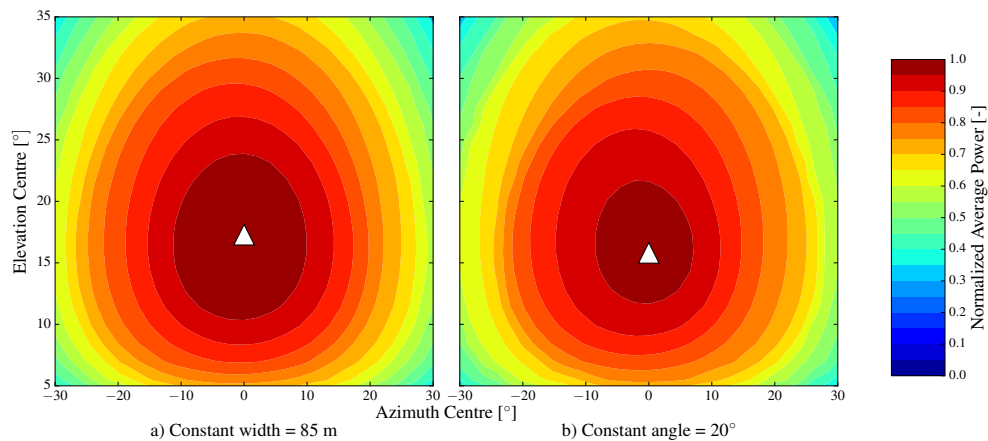


Figure 6.13: Normalized average power for a constant a) width and b) angle

Three main conclusions can be drawn. i) The optimal elevation moves up with a constant width, ii) the area of maximum power increases compared with to the constant angle, and iii) the power production slightly increases. The first is due to the shape that the trajectory takes with respect to the wind direction, while the latter two are due to the higher alignment between the high power zones and the flight path.

Fig. 6.14 shows the average power along the power centre of each case. Two additional cases of 10° and 43 m have been included. The three previous conclusions can still be seen, yet their influence decreases considerably if narrower figures are used.

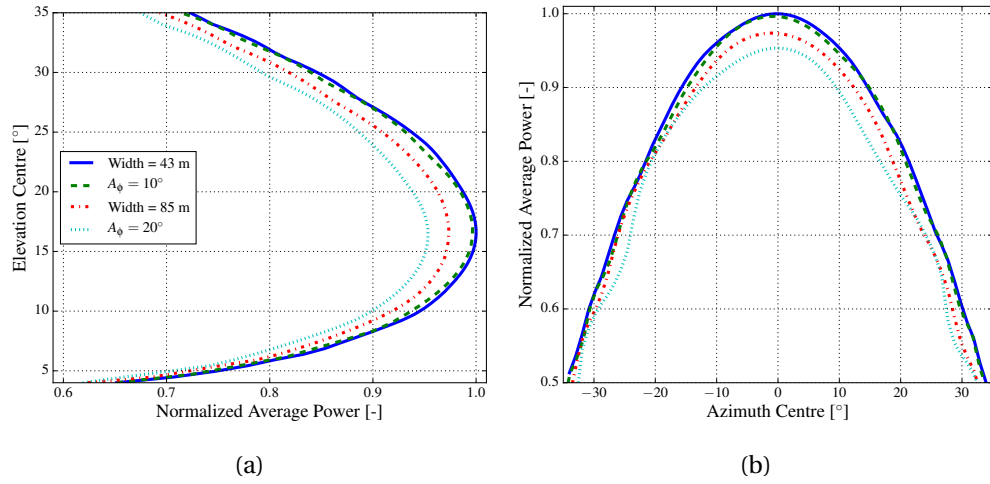


Figure 6.14: Variation of the average power along power centre in a) elevation and b) azimuth for different constant angle and width. $A_\beta = 3.5^\circ$ for all cases

6.1.4. TRACTION FORCE OPTIMIZATION

The optimal traction force has been previously studied by other authors as [11, 21, 49]. The optimal reel out force is obtained when the reel out speed is

$$v_{r,opt}^k = \frac{1}{3} v^w \sin \theta \cos \phi. \quad (6.3)$$

Fig. 6.15 shows the normalised mean mechanical power over a) force and b) reel out speed. The figure has been created using the Lissajous trajectory with $(\beta_c, \phi_c) = (16, 0)$ and $(A_\beta, A_\phi) = (1.5, 10)$. In addition, the dashed line shows the optimal reel out speed, calculated with the average elevation and azimuth. It can be observed that the maximum average power is obtained at 4500 N when the reel out speed is 4.1 m/s, same as the optimal reel out speed.

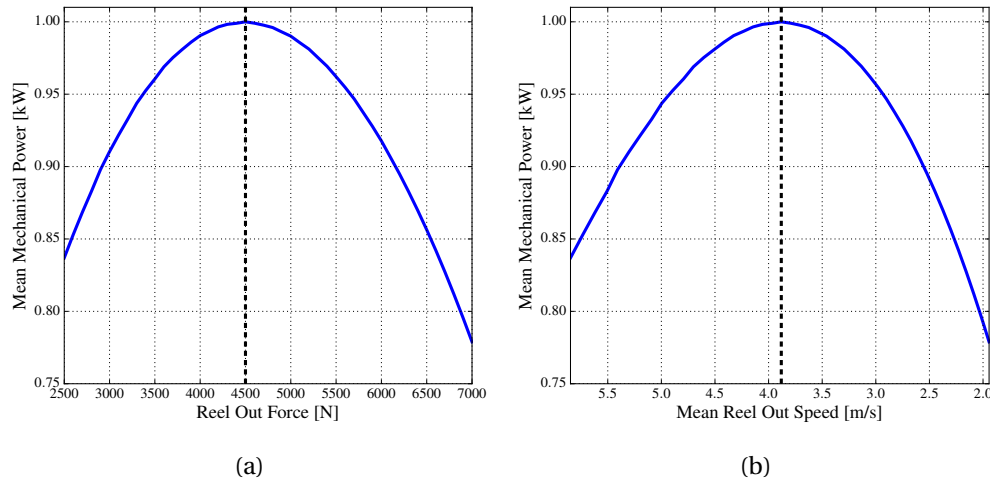


Figure 6.15: Normalized mean mechanical power over a) force and b) reel out speed. The dashed line is the optimal solution from eq. (6.3)

6.1.5. CONCLUSIONS OF THE OFFLINE TRACTION MAPPING

From the offline mapping, it can be concluded that i) the optimal path during traction phase is obtained when the figure is aligned with the azimuth direction of the wind at an elevation greater

than zero. ii) There is an optimal force that maximises the average power during traction. The maximum is obtained when the reel speed is approximately 1/3 the wind speed. iii) It is not possible to know a priori the exact location of the highest power zone nor the optimal force since it depends on the environmental conditions and the shape of the figure. iv) Smaller figures produce more power than wide figures. Thus, the size of the figure is determined by the steering capabilities of the kite, the controller, the motors and the battery consumption. Hence, they cannot be optimised during the simulation. v) It is beneficial for the path to fly down loops since it avoids temporary high angles of attack during the turns, large fluctuations of the power, and wearing of winch and generator. Finally, vi) a constant width figure has a slightly better performance than a uniform angle since the kite flies more time in high power zones, this advantage becomes less significant with narrower figures.

6.2. RETRACTION PHASE MAPPING

After a traction phase, the kite must be moved away from the high power zone to the edges of the wind window. For this, two main possibilities exist: retract to the zenith or the sides of the wind window. Both options will be presented in this section. First an unidirectional analysis will be shown, then the reeling force effect will be studied and, finally, a mapping of the retraction will be done.

6.2.1. UNIDIRECTIONAL RETRACTION MAPPING

In a similar manner as in Section 6.1.1, Fig. 6.16 shows an example of the power required to retract the kite at ψ equal to a) 180 and b) 90° at a radius of 400 m. The characteristics presented at the beginning of the chapter have been maintained, yet the retraction force has been set to 900 N and the depower input that has been increased to 0.47.

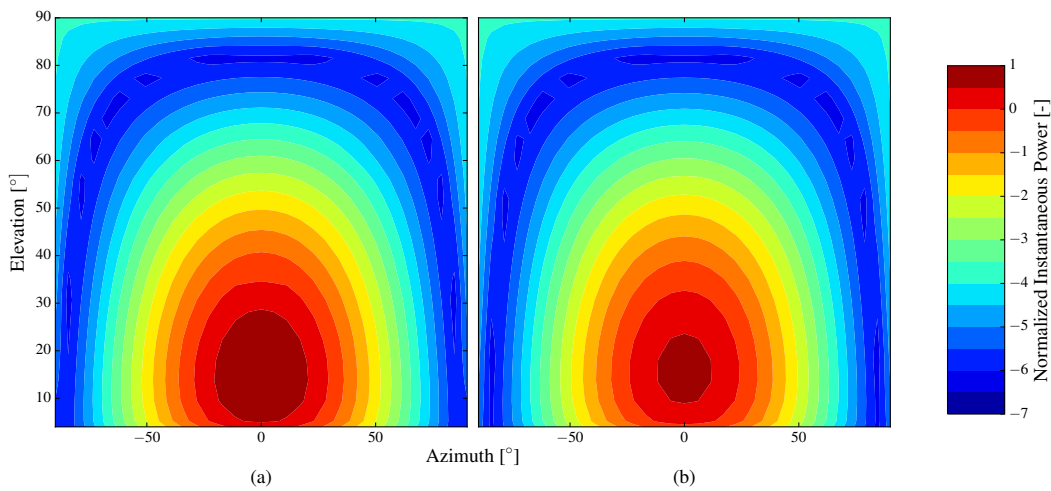


Figure 6.16: Power required for retraction at a) 180 and b) 90° at 400 m (left)

Both figures show that i) higher retraction rates are obtained by moving out of the wind window. However, ii) the great resemblance between both figures do not allow to conclude if the retraction should be in one direction or the other. Furthermore, the figures do not consider the reel in force as a variable, hence, the next section studies this effect.

6.2.2. RETRACTION FORCE DEPENDENCE

The reeling force plays a crucial role during the retraction. If the force is too high, the energy consumption will be high; yet if the force is too low, the time required for the retraction will be increased, decreasing the energy production of the cycle. To compare the effect of the retraction force, the average power cycle will be used, given by

$$\bar{P}_{\text{cycle}} = \frac{\sum P_{\text{traction}} + \sum P_{\text{retraction}} + \sum P_{\text{transition}}}{\Delta t_{\text{traction}} + \Delta t_{\text{retraction}} + \Delta t_{\text{transition}}} \quad (6.4)$$

Fig. 6.17 shows the normalised average power of the cycle versus the tether ground force for three reference wind speeds. The curves have been obtained using a hybrid model, using the predefined path for traction phase and the hierarchical control for retraction and transition. Hence, at the same reference wind speed, the traction power between the different curves is the same. In addition, the same conditions as in Section 5.3 have been used, considering a retraction from the zenith of the wind window and normalising the power with the maximum value at each wind speed. It can be observed that i) there is an optimal force to reel in the kite and ii) the optimal force increases with the wind speed. Hence, the online optimizer must be able to adjust the force during the retraction.

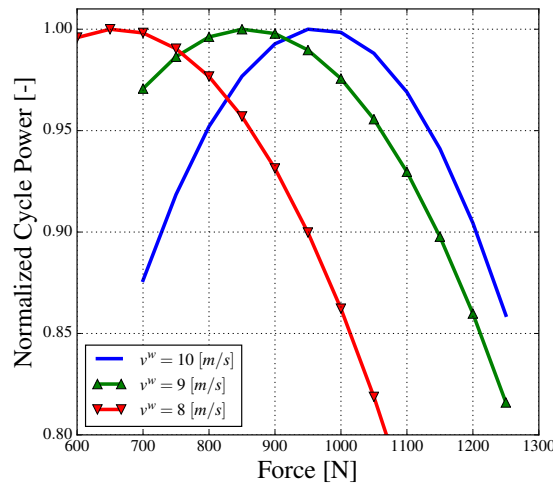


Figure 6.17: Normalized power per cycle for three reference speed. The retraction has been done from the zenith

6.2.3. RETRACTION MAPPING

To map the retraction phase, the retraction waypoint and the tether force must be considered. Fig. 6.18 shows the cycle using three different retraction way-points: $P_R =$ i) $(90, 0)$, ii) $(90, 90)$, and iii) $(30, 90)^\circ$. The first waypoint produces a retraction from the zenith, used as a reference to observe the behaviour of the other two. By changing ϕ_R the azimuth position of the retraction changes, while if β_R changes the elevation of the retraction waypoint is modified. Notably, if the elevation is below a certain threshold, the kite will hit the ground. This is a good example of a minimum height requirement for the online optimizer and the path planning strategy in general.

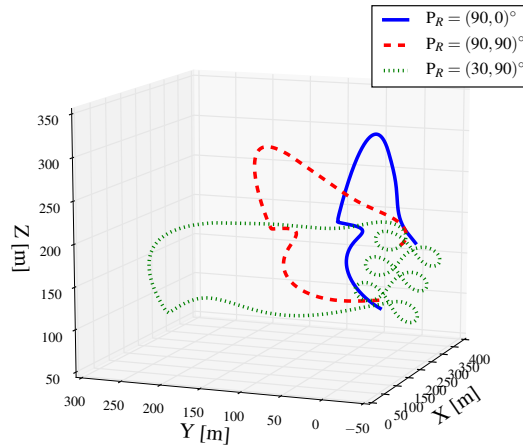
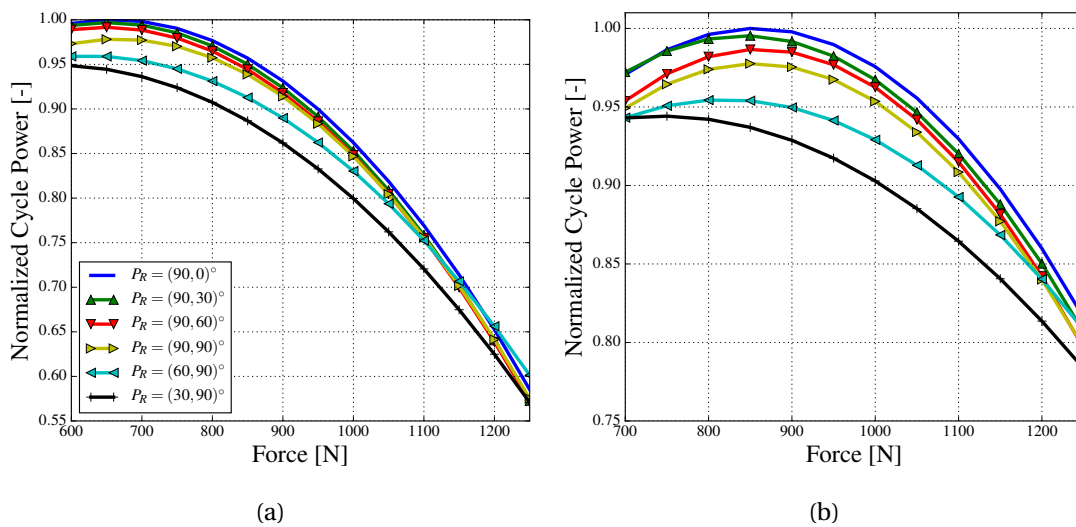


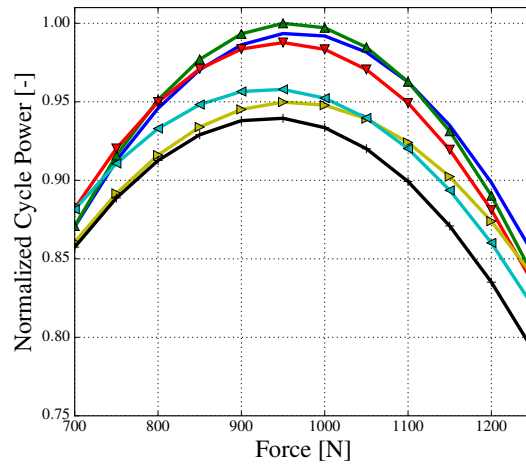
Figure 6.18: Retraction trajectory at different way-points $P_R = (\beta_R, \phi_R)$

Fig. 6.19 shows the average power per cycle over the tether ground force at three reference wind speeds: a) 8, b) 9, and c) 10 m/s for different retraction waypoints. It can be seen that i) there is a reel in force and a waypoint that maximises the average power cycle at each case. ii) The optimal position and reel in force depend on the wind speed, yet it is not possible to know the optimal value before hand. iii) Retracting through the sides of the wind window is beneficial at high wind speeds, while at low wind speed the zenith should be used. In Fig. a) and b) the power per cycle is reached when the retraction is at the zenith, while in Fig. c) the optimal retraction is obtained at the sides of the wind window. The main advantage of a zenith retraction is that the gravitational force is aligned with the radial direction and directly opposes the aerodynamic forces. Thus, to maintain the tether force constant, the reeling speed must increase to increase the required apparent speed. However, at high wind speeds, the apparent wind speed is enough to maintain the desired retraction, decreasing the reel speed. iv) If the maximum reel speed is reached during retraction, the force requirements will not be met, and the average cycle power will decrease. This explains the last curves of $P_R = (60, 90)^\circ$ & $(30, 90)^\circ$. v) If during the transition the force is over the maximum design force, the tether will be reel out, and the total tether for traction will decrease. This has not been included the simulation since the traction phase is common between wind speeds. Hence, the optimal retraction waypoint must not allow the forces to go above the maximum.



(a)

(b)



(c)

Figure 6.19: Normalized average power per cycle for different retraction way-points P_R . The reference wind speed is a) 8, b) 9 and c) 10 m/s

Notably, the curves should also be affected by the position at which retraction starts. Fig. 6.20 sketches two retraction trajectories aiming to the zenith. If the kite starts the retraction at an unfavourable moment w.r.t. the set waypoint, the retraction time will increase, and the cycle power will decrease.

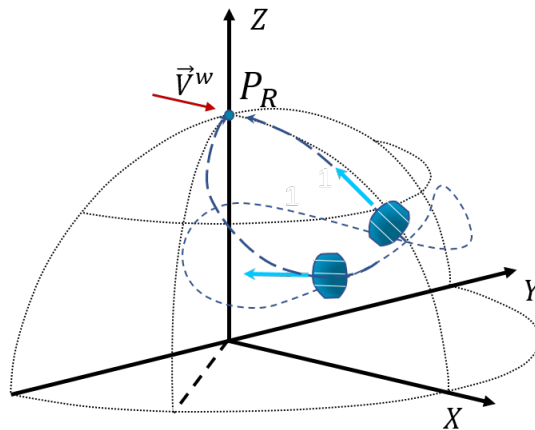


Figure 6.20: Traction to retraction path, the centered path is favourable for retraction

6.2.4. CONCLUSIONS OF THE OFFLINE RETRACTION MAPPING

Two main parameters must be optimised for the retraction phase: the reel in force and the way-point. To map both parameters the average cycle power was calculated at different wind speeds, retraction waypoints, and reel in forces. The following conclusions can be stated: i) An optimal way-point and reel in force exist for each wind speed. ii) It is not possible to determine a priori the optimal position nor the optimal retraction force. iii) At low wind speed, the optimal retraction is achieved at the zenith, while at high wind speeds the retraction should be performed on the sides. This is due to a balance between the alignment of the gravitational force and the contribution of the wind speed in the aerodynamic forces. Finally, iv) The optimal reel in force increases with the wind speed.

6.3. ONLINE OPTIMIZER

The online optimizer presented in this section is based on the conclusions obtained during the traction and retraction phase mapping. During traction, the algorithm aligns the path with the wind direction using the power measured on the ground, while the wind speed at the kite is used to estimate the optimal reel out speed. For retraction, the algorithm uses the average cycle power, aiming to maximise the ratio between energy consumption and retraction time. Traction and retraction algorithms use an adaptable coordinate search to decide each new force and position. The section has been divided into three parts: i) the description of the traction optimisation, ii) the description of the retraction optimisation, and iii) the full optimisation algorithm.

6.3.1. TRACTION OPTIMIZATION

The traction optimisation problem can be formulated as

$$\max_{\beta_c, \phi_c, F_{out}} \bar{P}(\Theta_T, \phi_w, v^w), \quad (6.5)$$

where v^w is the wind speed, ϕ_w the wind direction, and Θ_T is the description of the trajectory, given by

$$\Theta_T = (\beta_c, \phi_c, A_\beta, A_\phi, F_{out}, \dot{\psi}), \quad (6.6)$$

where A_β is half the height of the figure of eight, A_ϕ is half the width of the figure of eight, and $\dot{\psi}$ is the set turning rate at the corners of the figure. Hence, the aim of the optimizer is to find the azimuth centre, the traction force and the elevation centre that maximises the average power of the cycle described by Θ_T .

To determine the azimuth centre the power production on each side of the figure is used. The power at each side of the figure is given by

$$\bar{P}_{Left} = \frac{1}{N_L} \sum_0^{N_L} \{P(k) \mid \phi(k) \geq \phi_c\}, \quad \text{and} \quad (6.7)$$

$$\bar{P}_{Right} = \frac{1}{N_R} \sum_0^{N_R} \{P(k) \mid \phi(k) < \phi_c\}, \quad (6.8)$$

Where N is the number of time steps in a loop, P is the power, $\phi(k)$ is the current position of the kite, and ϕ_c is the centre of the figure. If the figure is misaligned with the wind window, a different power production will be produced on each side of the loops. Then, difference between both sides is

$$\Delta\bar{P} = \bar{P}_{Left} - \bar{P}_{Right}. \quad (6.9)$$

Algorithm 1 shows a pseudocode of the azimuth algorithm. For the convergence, a threshold $\Delta\bar{P}_{\min}$ is used. Notice that the index (i) indicates a loop, thus, one movement is taken at each loop.

Algorithm 1 Traction - Azimuth optimization, adapted from [57]

```

1 while true do
2   Calculate  $\Delta\bar{P}_i$ 
3   if  $|\Delta\bar{P}_i| > \Delta\bar{P}_{\min}$  then
4     seek min  $|\Delta\bar{P}|$ , update  $\phi_{c,i+1}$ 
5   end if
6 end while

```

Once the kite has been centred in the wind window, the average reel speed given by

$$\bar{r} = \frac{1}{T} \int_0^T \dot{r}_{out}(t) dt = \frac{1}{N\Delta T} \sum_0^N \dot{r}(k)\Delta T = \frac{1}{N} \sum_0^N \dot{r}(k), \quad (6.10)$$

is compared with the optimal reel speed

$$\bar{r}_{opt} = \frac{1}{3} \overline{v^w} \sin \bar{\theta}, \quad (6.11)$$

and the difference between is given by

$$\Delta \dot{r} = \Delta \bar{r}_{opt} - \Delta \bar{r}. \quad (6.12)$$

If the difference of the reel out is greater or smaller than a threshold, the force is adjusted. Notably, if the wind speed is not known, the power per cycle could have also been used to track the force. However, since the turn rate law requires the apparent speed, it has been assumed that the wind speed can be calculated with some level of accuracy. The average power per cycle has been used to track the force during retraction, and the procedure will be explained in the next section. Algorithm 2 shows the algorithm used to optimise the tether ground force. As before, $\Delta \dot{r}_{out,min}$ is used as a convergence criterion.

Algorithm 2 Traction - Tether ground force optimization

```

1 while true do
2   Calculate  $\Delta \dot{r}_{out,i}$ 
3   if  $\Delta \dot{r}_{out,i} > \Delta \dot{r}_{out,min}$  then
4     seek min  $\Delta \dot{r}_{out}$ , update  $F_{in,i+1}$ 
5   end if
6 end while
```

Finally, the algorithm aligns the elevation angle, seeking the maximum average traction power given by

$$\bar{P} = \frac{1}{T} \int_0^T P(t) dt = \frac{1}{N\Delta T} \sum_0^N P(k)\Delta T = \frac{1}{N} \sum_0^N P(k). \quad (6.13)$$

The pseudocode can be seen in algorithm 3.

Algorithm 3 Elevation optimization, adapted from [57]

```

1 while true do
2   Calculate  $\bar{P}_i$ 
3   seek max  $\bar{P}$ , update  $\beta_{c,i}$ 
4 end while
```

The final pseudocode is shown in algorithm 4. Two additional states have been included in line two and line 11, such as to consider more than one loop for each decision and to only start the retraction optimisation once the azimuth centre and the force have been aligned. The first aims to compensate for disturbances in the measurements due to turbulence or different paths taken by the controller, while the second aims to avoid wrong steps during the retraction optimisation.

Algorithm 4 Traction - Online Optimization, adapted from [57]

```

1 while true do
2   if  $N_{loops}$  flow then
3     Calculate  $\Delta \bar{P}_i$ ,  $\Delta \dot{r}_{out,i}$  and  $\bar{P}_i$ 
4     if  $|\Delta \bar{P}_i| > \Delta \bar{P}_{min}$  then
5       seek min  $|\Delta \bar{P}|$ 
6       update  $\phi_{c,i+1}$ 
```

```

7     else if  $\Delta \dot{r}_{out,i} > \Delta \dot{r}_{out,min}$  then
8       seek min  $\Delta \dot{r}_{out}$ 
9       update  $F_{in,i+1}$ 
10    else
11      Optimize Retraction True
12      seek max  $\bar{P}$ 
13      update  $\beta_{c,i+1}$ 
14    end if
15  end if
16 end while
```

6.3.2. RETRACTION OPTIMIZATION

To optimise the retraction the average power per cycle, given by eq. (6.4), has been used. The force and the retraction waypoint use the same coordinate search method; however, since both use the same parameter, a different approach than the traction optimisation must be taken. To chose which parameter to optimise, the traction algorithm uses a minimum difference between the desired and the current parameter. This is not possible for the retraction since the optimal power per cycle is not known and a relation between the optimal reel in and the wind speed does not exist. Hence, the most suitable option is to optimise each parameter until the minimum step is reached, slightly increasing the energy production at each cycle.

The retraction optimization is formulated as

$$\max_{\beta_R, \phi_R, F_{in}} \bar{P}_{\text{cycle}}(\Theta_R, \phi_w, v^w), \quad (6.14)$$

where Θ_R is the retraction trajectory, given by

$$\Theta_R = (\beta_R, \phi_R, F_{in}). \quad (6.15)$$

Thus, the algorithm aims to find the retraction waypoint and reel in force that maximises average power per cycle. The retraction algorithm is presented in algorithm 5. In the pseudocode, $\delta F_{in}/\delta \epsilon$ are the retraction force and way-point steps, $\delta F_{in,\min}/\delta \epsilon_{\min}$ are the minimum size step for the force and the way-point, N_R/N_ϵ is used to start the force optimization after reaching the minimum way-point step and N_{cycles} is used to average more than one retraction phase.

Algorithm 5 Retraction - Online Optimization

<pre> 1 while true do 2 if N_{cycles} flown then 3 Calculate \bar{P}_{cycle} 4 if $\delta F_{in} \neq \delta F_{in,\min}$ then 5 seek max E 6 update $F_{in,i+1}$ 7 else 8 seek max E 9 update $P_{R,i+1}$ </pre>	<pre> 10 if $\delta \epsilon = \delta \epsilon_{\min}$ then 11 $\delta F_{in} = N_{F_{in}} \delta F_{in,\min}$ 12 $\delta \epsilon = N_\epsilon \delta \epsilon_{\min}$ 13 end if 14 end if 15 end if 16 end while </pre>
--	--

The sequence in line 9: *update P_R* is also divided into two subsequent optimisations since it is composed by the elevation angle β_R and the azimuth angle ϕ_R . As it has been shown in Section 6.2.3, the retraction point completely describes the upper part of quarter sphere when $\beta_R = \pi/2$ and $\phi_R = [0, \pi/2]$, while the bottom of the quarter sphere is described by $\beta_R = [0, \pi/2]$ and $\phi_R = \pi/2$. Both cases are sketch in Fig. 6.21. Thus, the coordinate search algorithm is arranged to modify one or the other, depending on the current position and the common step angle $\delta \epsilon$.

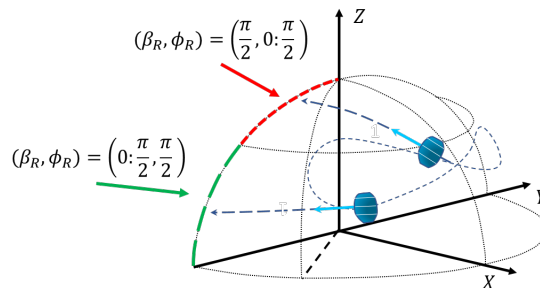


Figure 6.21: Retraction waypoint sketch

Algorithm 6 shows the pseudo-code to update the waypoint P_R . It can be seen that the algorithm decides to update the elevation or the azimuth angle, depending on which angle is equal to $\pi/2$. Lines 3 to 6 and 9 to 12 are used for the intersection between the upper and lower quarter sphere.

Algorithm 6 Update P_R

```

1  if  $\beta_{R,i} = \pi/2$  then
2    update  $\phi_{R,i+1}$ 
3    if  $\phi_{R,i+1} = \pi/2$  then
4       $\beta_{R,i+1} = \pi - \phi_{R,i+1}$ 
5       $\phi_{R,i+1} = \pi/2$ 
6    end if
7  else
8    update  $\beta_{R,i+1}$ 
9    if  $\beta_{R,i+1} = \pi/2$  then
10      $\phi_{R,i+1} = \pi - \beta_{R,i+1}$ 
11      $\beta_{R,i+1} = \pi/2$ 
12   end if
13 end if

```

6.3.3. FINAL OPTIMIZATION ALGORITHM

The final algorithm for the traction cycle optimization is shown in algorithm 7. In the algorithm, $\delta\phi$, δF_{out} , and $\delta\beta$ are the time steps for the elevation, the force and the azimuth; $\delta\phi_{\min}$, $\delta\beta_{\min}$ and $\delta F_{out,\min}$ are the minimum steps for each variable; $\delta\phi_{\max}$, $\delta\beta_{\max}$, and $\delta F_{out,\max}$ are the maximum steps for each variable; c_{\exp} and c_{con} are constants used to increase or decrease the steps; F_{out}^{\min} and F_{out}^{\max} are the minimum and maximum force constrains, and β_c^{\min} is the minimum elevation constrain.

Algorithm 7 Traction Cycle Optimization

```

1  while true do
2    if  $N_{loops}$  flown then
3      if  $|\Delta\bar{P}(i)| > \Delta\bar{P}_{\min}$  then
4        if  $\Delta\bar{P}(i) > 0$  then
5          if  $\Delta\bar{P}(i-1) > 0$  then
6             $\delta\phi = \min\{\delta\phi_{\max}, c_{\exp}\delta\phi\}$ 
7          else
8             $\delta\phi = \max\{\delta\phi_{\min}, \frac{1}{c_{\text{con}}}\delta\phi\}$ 
9          end if
10          $\phi_c(i+1) = \phi(i) + \delta\phi$ 
11        else
12          if  $\Delta\bar{P}(i-1) < 0$  then
13             $\delta\phi = \min\{\delta\phi_{\max}, c_{\exp}\delta\phi\}$ 
14          else
15             $\delta\phi = \max\{\delta\phi_{\min}, \frac{1}{c_{\text{con}}}\delta\phi\}$ 
16          end if
17          $\phi_c(i+1) = \phi_c(i) - \delta\phi$ 
18        end if
19      else if  $|\Delta\dot{r}(i)| > \Delta\dot{r}_{out,\min}$  then
20        if  $\Delta\dot{r}(i) < 0$  then
21          if  $\Delta\dot{r}(i-1) < 0$  then
22             $\delta F_{out} = \min\{\delta F_{out,\max}, c_{\exp}\delta F_{out}\}$ 
23          else
24             $\delta F_{out} = \max\{\delta F_{out,\min}, \frac{1}{c_{\text{con}}}\delta F_{out}\}$ 
25          end if
26           $F_{out}(i+1) = F_{out}(i) + \delta F_{out}$ 

```

```

27     else                                                                                                     ▷ /* Δṙ(i) > 0 */
28         if Δṙ(i - 1) < 0 then
29             δFout = min{δFout,max, cexpδFout}
30         else
31             δFout = max{δFout,min,  $\frac{1}{c_{con}}$ δFout}
32         end if
33         Fout(i + 1) = Fout(i) - δFout
34     end if
35     Fout(i + 1) = min(Foutmax, Fout(i + 1))
36     Fout(i + 1) = max(Foutmin, Fout(i + 1))
37 else
38     if  $\bar{P}(i - 1) < \bar{P}(i)$  then
39         δβ = min(δβ,max, cexpδβ)
40         if βc(i - 1) > βc(i) then
41             βc(i + 1) = βc(i) - δβ
42         else
43             βc(i + 1) = βc(i) + δβ
44         end if
45     else                                                                                                     ▷ /*  $\bar{P}(i - 1) \geq \bar{P}(i)$  */
46         δβ = max{δβ,min,  $\frac{1}{c_{con}}$ δβ}
47         if βc(i - 1) > βc(i) then
48             βc(i + 1) = βc(i) + δβ
49         else
50             βc(i + 1) = βc(i) - δβ
51         end if
52         βc(i + 1) = max{βcmin, βc(i + 1)}
53     end if
54 end if
55 end if
56 end while

```

Similarly, the complete retraction algorithm is shown in algorithm 8. $\delta_{F_{in}}$ and δ_{ϵ} are the reel in force and waypoint angle steps; $\delta_{F_{in},min}$ and $\delta_{\epsilon,min}$ are the minimum steps; $\delta_{F_{in},max}$ and $\delta_{\epsilon,max}$ are the maximum steps; F_{in}^{min} and F_{in}^{max} are the minimum and maximum force constrains; and β_R^{min} is the minimum elevation constraint for retraction.

Algorithm 8 Retraction Cycle Optimization

```

1  while true do
2      if Ncycles flown then
3          if |δFin| > δFin,min then
4              if  $\bar{P}_{cycle}(i - 1) < \bar{P}_{cycle}(i)$  then
5                  δFin = min(δFin,max, cexpδFin)
6                  if Fin(i - 1) < Fin(i) then
7                      Fin(i + 1) = Fin(i) + δFin
8                  else
9                      Fin(i + 1) = Fin(i) - δFin
10                 end if
11             else                                                                                             ▷ /*  $\bar{P}_{cycle}(i - 1) > \bar{P}_{cycle}(i)$  */
12                 δFin = max(δFin,min,  $\frac{1}{c_{con}}$ δFin)
13                 if Fin(i - 1) < Fin(i) then
14                     Fin(i + 1) = Fin(i) - δFin
15                 else
16                     Fin(i + 1) = Fin(i) + δFin
17                 end if
18             end if
19             Fin(i + 1) = min(Finmax, Fin(i + 1))
20             Fin(i + 1) = max(Finmin, Fin(i + 1))

```

```

21  else
22    if  $\beta_R(i) = \pi/2$  then
23      if  $\bar{P}_{\text{cycle}}(i-1) < \bar{P}_{\text{cycle}}(i)$  then
24         $\delta_\epsilon = \min(\delta\epsilon_{\text{max}}, c_{\text{exp}} \delta_\epsilon)$ 
25        if  $\phi_R(i-1) < \phi_R(i)$  then
26           $\phi_R(i+1) = \phi_R(i) + \delta_\epsilon$ 
27        else
28           $\phi_R(i+1) = \phi_R(i) - \delta_\epsilon$ 
29        end if
30      else
31         $\delta_\epsilon = \max(\delta\epsilon_{\text{min}}, \frac{1}{c_{\text{con}}} \delta_\epsilon)$ 
32        if  $\phi_R(i-1) < \phi_R(i)$  then
33           $\phi_R(i+1) = \phi_R(i) - \delta_\epsilon$ 
34        else
35           $\phi_R(i+1) = \phi_R(i) + \delta_\epsilon$ 
36        end if
37      end if
38      if  $\phi_R > \pi/2$  then
39         $\beta_R(i+1) = \pi - \phi_R(i+1)$ 
40         $\phi_R(i+1) = \pi/2$ 
41      end if
42    else
43      if  $\bar{P}_{\text{cycle}}(i-1) < \bar{P}_{\text{cycle}}(i)$  then
44         $\delta_\epsilon = \min(\delta\epsilon_{\text{max}}, c_{\text{exp}} \delta_\epsilon)$ 
45        if  $\beta_R(i-1) < \beta_R(i)$  then
46           $\beta_R(i+1) = \beta_R(i) + \delta_\epsilon$ 
47        else
48           $\beta_R(i+1) = \beta_R(i) - \delta_\epsilon$ 
49        end if
50      else
51         $\delta_\epsilon = \max(\delta\epsilon_{\text{min}}, \frac{1}{c_{\text{con}}} \delta_\epsilon)$ 
52        if  $\beta_R(i-1) < \beta_R(i)$  then
53           $\beta_R(i+1) = \beta_R(i) - \delta_\epsilon$ 
54        else
55           $\beta_R(i+1) = \beta_R(i) + \delta_\epsilon$ 
56        end if
57      end if
58       $\beta_R(i+1) = \max(\beta_R^{\text{min}}, \beta_R(i+1))$ 
59      if  $\beta_R > \pi/2$  then
60         $\phi_R(i+1) = \pi - \beta_R(i+1)$ 
61         $\beta_R(i+1) = \pi/2$ 
62      end if
63    end if
64    if  $\delta_\epsilon = \delta\epsilon_{\text{min}}$  then
65       $\delta_{F_{in}} = N_{F_{in}} \delta_{F_{in}}$ 
66       $\delta_\epsilon = N_\epsilon \delta_\epsilon$ 
67    end if
68  end if
69 end if
70 end while

```

6.4. CHAPTER CONCLUSIONS

The desired characteristics of an optimal path were studied using a prescribed trajectory and, based on them; an online optimizer was developed. The traction and retraction phases were mapped seeking for the highest manoeuvrability, and power production. From the offline mapping, it can be concluded that: i) there is a centre point for the figure of eight and a waypoint for retraction that maximizes the power/energy production; ii) six variables define the optimal conditions: the forces, the centre of the figure and the retraction way-point; iii) the variables depend on the wind speed and cannot be known a priori; iv) narrow figures with down loops present several advantages over wide figures with up loops; and v) the shape of the figure during traction must be determined a priori according to the capabilities of the kite. Furthermore, the online optimizer was presented. The algorithm is divided in traction and retraction phases. For traction, the coordinate search method optimises one parameter per loop, while for retraction it optimises one parameter per cycle. Two thresholds are used to decide which parameter must be optimised during traction, while for retraction since no threshold can currently be used, a parameter is optimised until the minimum step is reached. Finally, the next chapter presents the capabilities of the optimizer.

7

CASE STUDY

The present sections aim to show the capabilities of the optimisation algorithm. The case study used for this purpose is the flight test considered for the validation of the quasi-steady model in chapter 4. Two cases will be presented: i) the trajectory from the 7th cycle of the flight test and ii) the optimised trajectory under the same system and environmental conditions. Three considerations will be taken. 1) Since the real aerodynamic coefficients from the V3 kite are unknown, the latter case uses the same generic aerodynamic coefficients presented in Fig. 4.3. 2) A constant wind profile described by Tab. 7.1 will be used. Finally, 3) it is assumed that the centre of reference trajectory is aligned with the wind window.

Property	Value	Property	Value	Property	Value
Reference height	6 m	z_R	0.0058 m	v_w^R	7 m/s

Table 7.1: Wind profile test case

7.1. RESULTS

The following graphs show the convergence of the six parameters used for the optimisation. The traction parameters are displayed against the number of loops, while the retraction parameters are shown against the number of cycles. The initial conditions of the path for both cases are presented in Tab. 7.2. The initial conditions have been chosen such as to demonstrate the convergence rate of the algorithm for each parameter.

Property	Case 1	Case 2	Property	Case 1	Case 2
Retraction Force	500 N	600 N	Traction Force	3500 N	3500 N
Elevation Centre	13.5°	20°	Azimuth Centre	0°	14°
Retraction Elevation	90°	90°	Retraction Azimuth	0°	40°
Figure Half Width	20°	7.5 °	Figure Eight	4°	1.5°
Side turn rate	-	2 rad/s	Loop direction	up	down

Table 7.2: Flight parameters for the flight test and initial conditions for the optimization

Fig. 7.1 shows the test and optimized trajectories. Notice that no force constraints are enforced to prove the effectiveness and convergence rate of the optimizer, yet a minimum elevation angle has been implemented. The optimization constants are presented in Tab. A.1. The dotted black line in

the following figures shows the seventh cycle of the test flight, while the continues blue line shows the convergence of the different parameters over the loops and cycles.

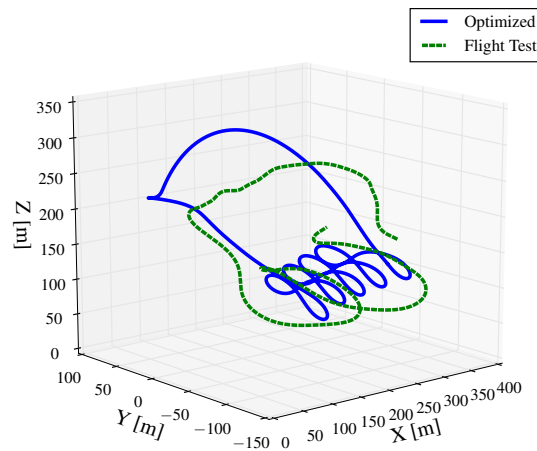


Figure 7.1: Trajectory of the optimized, and reference cases

Fig. 7.2 shows a) the azimuth centre, b) the reel out force, and c) the elevation centre over loop number. It can be stated that i) the azimuth centre in Fig a) reaches one degree of difference from the centre of the wind window after 10 loops, these are approximately 3 cycles or 6 minutes. ii) The azimuth centre does not achieve a complete alignment with the wind window due to the force threshold and asymmetric shape of the figure. As it can be seen Fig. 7.1, the loops of the optimized trajectory are not symmetric w.r.t the P_{centre} . This is due to the freedom of the controller to align the kite heading with the desired waypoint. For the force to be the same on both sides, the figure must be symmetric, which can be achieved by a) narrower figures or b) an extra waypoint between the turning and the side set point. Nevertheless, iii) the misalignment has a negligible effect since, according to the traction mapping of Section 6.1.2, the power curve is flat close to the azimuth centre. iv) The reel out force in Fig. b) increased from 3500 to 4500 N in 10 loops (3 cycles, 6 minutes). iv) In Fig. c) the elevation requires 21 loops (7 cycles, 14 minutes) to adapt from 20 to 16.0°. Small fluctuations still persist after, yet their influence is neglectible. v) In total, the traction phase is optimised in 13 cycles (approximately 26 minutes) from the initial state.

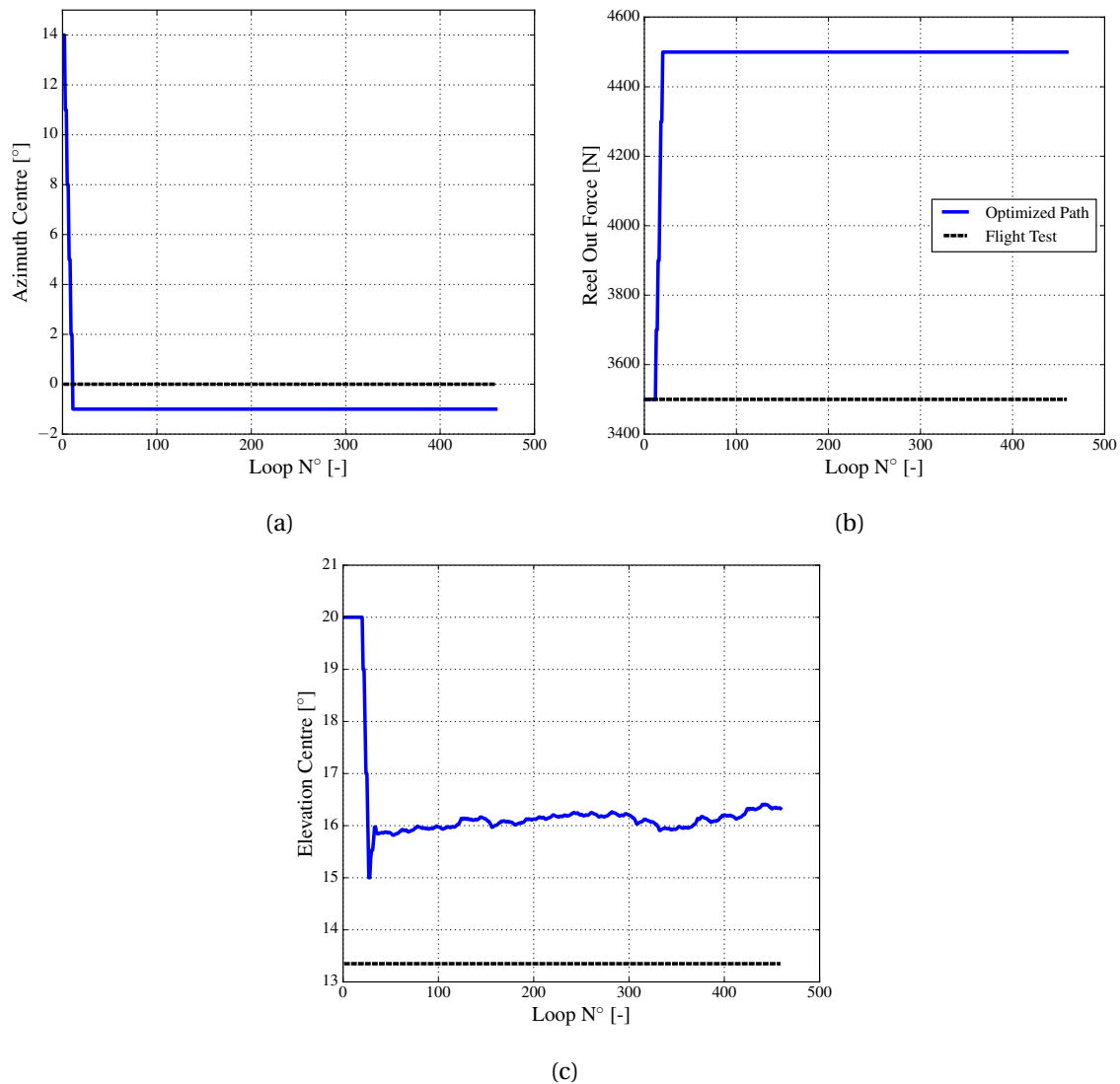


Figure 7.2: a) Azimuth centre, b) reel out force, and c) elevation centre over loop number

Fig. 7.3 shows a) the reel in force, b) the retraction azimuth, and c) the retraction elevation over the cycle number. It can be seen that i) the retraction optimisation starts at the 10th cycle along with the elevation centre optimisation. ii) The reel in force in Fig a) increases rapidly converging to 1200 N after 10 cycles, only mild adjustments are observed afterwards. iii) In Fig b) the azimuth decreases from 40 to 10° in 13 cycles. iii) Due to the low wind speed, no change in the elevation is required. Finally, iv) If a relation for the retraction force or reel in speed is found, the algorithm can be improved even further.

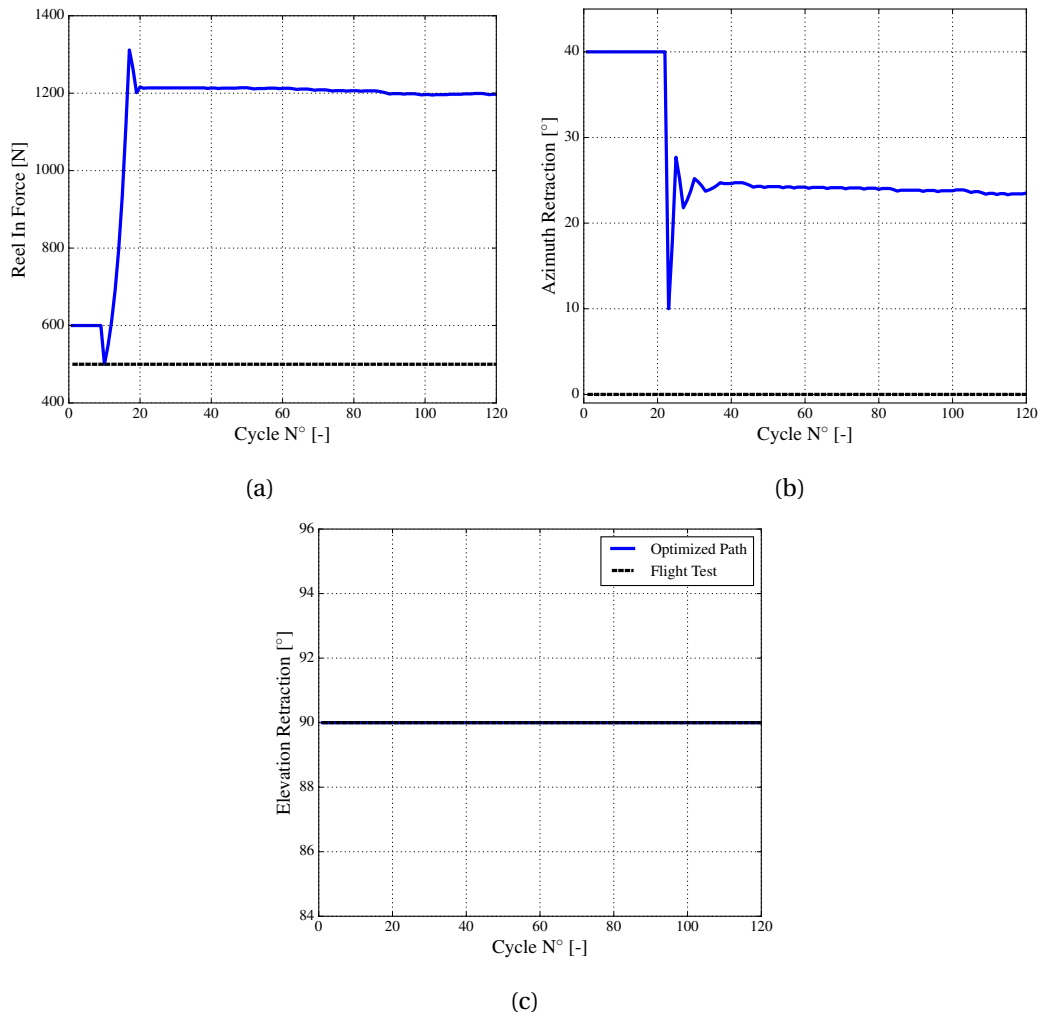


Figure 7.3: a) Reel in force, b) retraction azimuth and c) retraction elevation over the cycle number

Fig. 7.4 shows a) the instantaneous power over time, b) the average mechanical power over cycle number, and c) the average power per cycle over cycle number. From the instantaneous power in Fig a) it can be stated that: i) The optimised cycle time is almost 30 seconds faster than the reference flight, decreasing by 23%. ii) Lower power fluctuations during traction phase are achieved by flying narrower and accurate figures with down loops. iii) The retraction power has a different shape since the flight test has been performed with a constant reel in speed, while the optimisation has been carried out with a uniform reel in force. From the mean mechanical power in Fig b) it can be stated that i) the traction power of case 2 is almost four times higher than the test flight. ii) An increased from 12 to 14 kW (16%) has been obtained in 13 cycles. iii) The sharp increase in the first three cycles is due to the azimuth alignment, the next 7 cycles are produced by the reel out force, while the last increase is due the elevation. iv) A peak is observed at cycle N°11, yet it decreases over time, this is due to the non-linear effects in the system since even if the same waypoints are used in different cycles, the path may differ between them. Finally, from the average power per cycle in Fig. c) it can be stated that i) the optimisation increased the power cycle from 47 to 94 kW/s, this is 100% increase from the initial trajectory and a 40% increase from the flight test. ii) The traction phase is responsible for a 55% increase in power cycle, while the rest is due to the increase in retraction force (decrease in cycle time). iii) At low wind speeds, the retraction point plays a minor role in the power production.

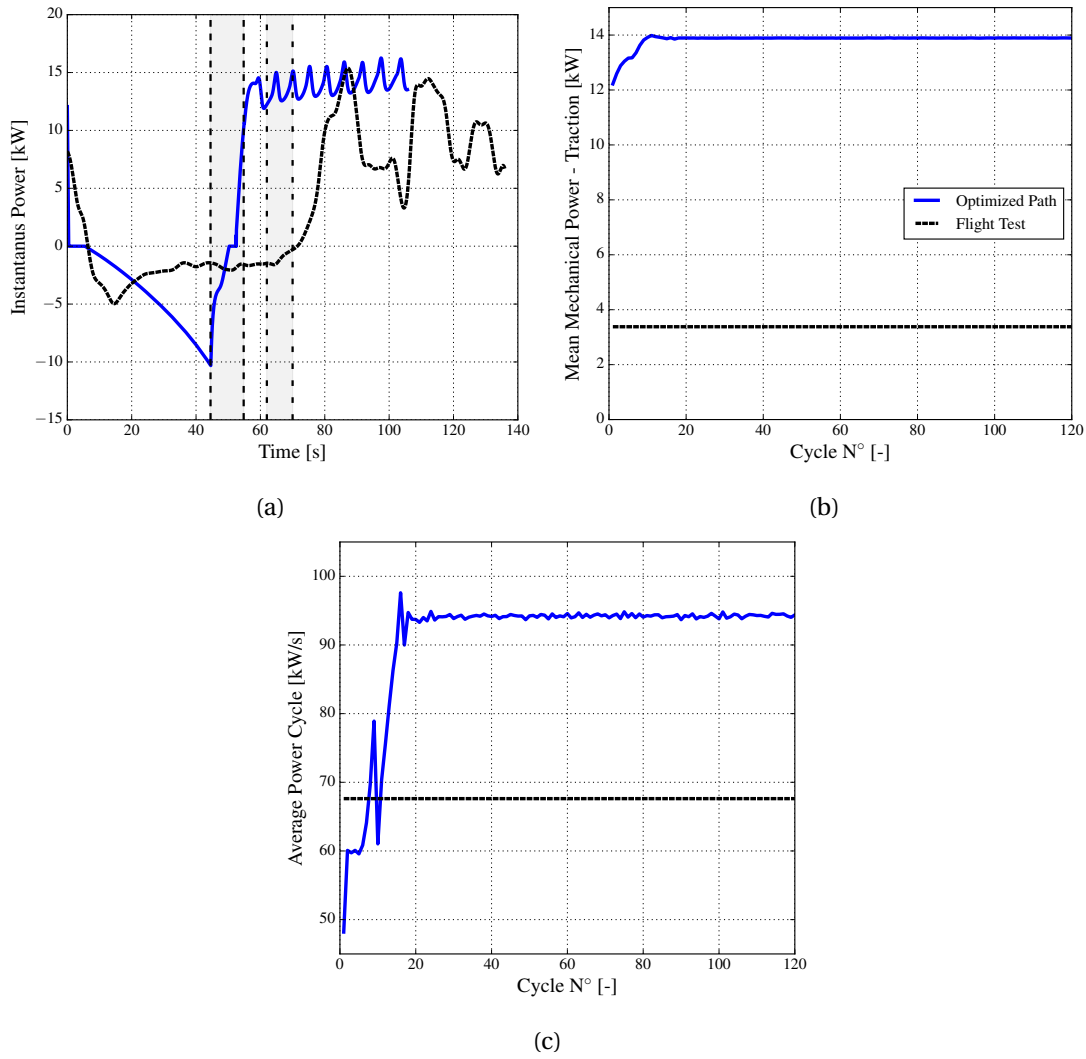


Figure 7.4: a) Instantaneous power over time, b) mean mechanical power over cycle number, and c) average power per cycle over cycle number. The transition phase is shown as a gray area in a). Short spaced dashes: optimized trajectory. Long space dashes: flight test.

Finally, the optimized values are presented in Tab. 7.3. Furthermore, the optimal results have also been obtained by mapping the wind window. It can be concluded that i) the optimisation obtain similar results as the mapping, proving its effectiveness. ii) The highest difference between the optimisation and mapping is obtained at the retraction elevation. However, as it was seen in Fig. 6.19, the retraction waypoint plays a minor role in the power production at low wind conditions. iii) The final traction power is less than 2% lower than the mapped result, while the difference for the power cycle is 3%.

Property	Optimisation	Mapping	Property	Optimisation	Mapping
Retraction Force	1200 N	1250 N	Traction Force	4500 N	4475 N
Elevation Centre	16.1°	16.5°	Azimuth Centre	0°	-1°
Retraction Elevation	90°	90°	Retraction Azimuth	23.8°	0°
Traction Power	13.9 kW	14.1 kW	Cycle Power	94.3 kW/s	96.4 kW/s
Cycle Time	105 s	104 s			

Table 7.3: Final parameters from the optimization and mapping

7.2. CHAPTER CONCLUSIONS

The path optimisation algorithm was used in a case study. The flight test used for validation has been used as a reference. Thus, the V3 kite with the derived environmental conditions of the flight data was considered. The optimisation run for 120 cycles, optimising the six parameters explained in the previous chapter: the reel out force, the reel in force, the azimuth centre, the retraction azimuth, the elevation centre, and the retraction elevation. The convergence of each parameter was demonstrated using their values against the number of loops or cycles. From the convergence, it can be concluded that i) all the parameter converged to the optimal value. ii) The optimisation required 40 cycles to reach the convergence of all the parameters; this is approximately 40 minutes. iii) If the figure is not completely symmetric, the azimuth centre does not converge to the centre of the wind window. iv) The retraction optimisation can be improved if a relation for the optimal traction force or reel in speed is found. Moreover, from the results, it can be concluded that i) a narrow and reliable figure with down loops decreases the power fluctuations and increases the average power of the cycle. ii) The average power during traction increased 16% from the initial trajectory and four times from the reference test flight. iii) The cycle power increased 100% from the original trajectory and 40% from the reference trajectory. Finally, iv) at this environmental conditions, the traction optimisation is responsible for 55% of the increase in energy production, while the rest is mainly due to the decrease in retraction time produced by a higher retraction force.

8

CONCLUSIONS AND RECOMMENDATIONS

The trajectory of an airborne wind energy wing has been studied and optimized. To do so, the complete system has been simulated using an aerodynamic model, a tether model, a kite controller and a path planning strategy. For the optimization, the wind window has been mapped for traction and retraction phases. Then, the conclusions from the mapping have been used to develop the optimization algorithm, and the optimizer has been used in a case study. The following conclusions have been reached:

1) The quasi-steady model was used to model the aerodynamic forces at the kite. The model is based on three assumptions i) the kite surface to mass ratio is relatively large, ii) the accelerations of the system are low, and iii) the flight is dominated by the aerodynamic and tether forces. The model is flexible, accepting a wide range of inputs depending on the desired outputs. During this research, the kite characteristics, position and desired tether force were used to determine the velocities, aerodynamic forces and power production along the path.

2) The quasi-steady model was validated against experimental data. The quasi-steady model can accurately predict the transition, traction and retraction phases if the correct geometry, aerodynamic coefficients and wind conditions are provided. If the exact aerodynamic coefficients are not known, the use of generic coefficients can still provide a reasonable estimate of the performance of the system. The aerodynamic coefficients and the angle of attack of the kite are the most sensitive parameters and should be studied in depth in future studies.

3) Three tether models have been presented: i) the high fidelity model, ii) the low fidelity model and iii) the lumped model. Of the three, the discretized low fidelity model is the best option for optimisation purposes. The high fidelity model, despite being the most accurate of the three, has high computational costs that makes it unsuitable for optimisation. The lumped model creates a fictional radial component since it assumes that the tether and kite drag act in the same direction. The discretized low fidelity model and its approximation are feasible options for optimisation purposes. Nevertheless, due to the profile of the apparent wind speed, the approximation underestimates the tether drag.

4) A hierarchical controller was used to manoeuvre the kite. The controller was divided into three loops: bearing control, attitude control and steering input. The first calculates the desired heading according to the set waypoint, the second calculates the difference between the current and the desired heading, while the third calculates the steering input using the turn rate law. The simulations show that if the constants that describe the steering capabilities of the kite are known and the apparent speed is measured, the hierarchical controller can accurately and reliably manoeuvre the kite along the desired trajectory.

5) The path planning was divided into three phases: traction, retraction and transition. Each phase includes a start condition, a set force, a set depowers and at least one way-point. The starting condition of each phase is important since it avoids poor behaviours of the controller, affecting the power production and the duration of each phase. Thus, the transition phase starts when the tether is completely reeled in, the traction when the kite is close to the centre of the figure, and the retraction when the heading of the kite aims in the desired direction. In total three waypoints have been used to describe the full trajectory: i) the retraction way-point, ii) the left and iii) the right side of the figure of eight. A more reliable description of the figure of eight has been given using the heading and the azimuth position.

6) To study the traction phase, the power production along the wind window was mapped using a prescribed path. It was determined that there is an area in which the power production is maximised. This area is obtained when the centre of the traction phase is aligned with the wind window and at elevation bigger than zero. The exact location of this area cannot be known a priori, it depends on the wind speed, the shape of the figure and the reel out speed. Smaller figures produce more power than wide figures and they are less sensitive to power fluctuations. Thus, the size of the figure should be determined according to the steering capabilities of the kite, the controller, the motors and the battery consumption. Down loops have less force and power fluctuations than up loops. Therefore, they are less wearing on the components. Additionally, they are more manoeuvrable since the apparent speed does not decrease as in up loops. A constant width description of the figure of eight has a slightly better performance than a constant angle since the kite flies more time in high power zones, this advantage becomes less significant with narrower figures.

7) To study the retraction phase the average power per cycle was used. It was determined that there is a point in which the energy of the cycle is maximised. The exact location of the point cannot be known a priori, it varies with the wind speed, the reel in force and the retraction way-point. At low wind speed, the optimal retraction is obtained at the zenith, while at high wind speeds the retraction should be performed at the sides. This is due to a balance between the alignment of the gravitational force and the contribution of the wind speed in the aerodynamic forces.

8) Based on the path characteristics obtained during the mapping, an online optimizer was developed. The main parameters to be optimised are the reel in and reel out force, the retraction waypoint and the centre of the figure of eight. The algorithm was divided in traction and retraction phases. For traction, the coordinate search method optimises one parameter per loop seeking to maximise the average power, while for retraction it optimises one parameter per cycle seeking to maximise the average power per cycle. Two thresholds are used to decide which parameter must be optimised during traction, while for retraction since currently no threshold can be used, a parameter is optimised until the minimum step is reached.

9) A case study comparing the flight test used for validation and an optimised trajectory has been presented. The algorithm found the optimal trajectory, resulting in a 16% increase in traction power and a 100% increase in the power per cycle. The traction optimisation was responsible for 55% of the increase in cycle power, while the rest was obtained by increasing the retraction force and decreasing the retraction time. If the figure of eight is not completely symmetric the optimizer does not achieve the zero azimuth location, yet the power difference is negligible. Both phases converged quickly to the optimal values, yet the retraction phase could be improved even further if a relation for the optimal reel in speed or retraction force is found.

Finally, for future work it is recommended to i) fully characterise the geometry and performance of the kites. This includes their aerodynamic coefficients, the shape at different forces, and the relation between the depower and the angle of attack. ii) A system to accurately measure the apparent wind speed is indispensable for a yaw steering wing since its manoeuvrability depends on it. If the apparent wind speed is not known, the controller will have a poor behaviour. iii) The position where

the traction phase changes to retraction phase should be studied further since it severely affects the retraction time. v) To further optimise the retraction phase a relation between the reel in speed and the wind speed must be derived.

A

OPTIMIZATION PARAMETERS

Tab. A.1 includes the optimization constants used in chapter 7.

Property	Value	Property	Value	Property	Value
$\delta F_{out,min}$	5 N	$\delta F_{out,max}$	200 N	$\delta \phi_{min}$	0.01°
$\delta \phi_{max}$	3.0°	$\delta \beta_{min}$	0.01°	$\delta \beta_{max}$	1.0°
$\Delta \bar{P}_{min}$	0.1 kW	$\Delta \dot{r}_{out,min}$	0.2 m/s	c_{exp}	1.3
c_{con}	2.6	$\delta F_{in,min}$	1 N	$\delta F_{in,max}$	200 N
$\delta \epsilon_{min}$	0.1°	$\delta \epsilon_{max}$	30°	β_c^{min}	12°
$N_{F_{in}}$	2.0	N_{F_c}	2.0	β_R^{min}	30°
F_{in}^{max}	4000 N	F_{in}^{min}	500 N		

Table A.1: Wind profile test case

BIBLIOGRAPHY

- [1] Ampyx-Power, 2008. <https://www.ampyxpower.com/> [Accessed: 19 January 2017].
- [2] J. Andersson, J. Åkesson, and M. Diehl. Casadi – a symbolic package for automatic differentiation and optimal control. In *Recent Advances in Algorithmic Differentiation*, pages 297–307. Springer, 2012. ISBN 978-3-642-30022-6. URL http://dx.doi.org/10.1007/978-3-642-30023-3_27.
- [3] C. L. Archer and M. Z. Jacobson. Evaluation of global wind power. *J. Geophys. Res.*, 110(D12): 1–20, 2005. ISSN 0148-0227. doi: 10.1029/2004JD005462.
- [4] I. Argatov, P. Rautakorpi, and R. Silvennoinen. Estimation of the mechanical energy output of the kite wind generator. *Renewable Energy*, 34(6):1525–1532, 2009. ISSN 09601481. doi: 10.1016/j.renene.2008.11.001. URL <http://dx.doi.org/10.1016/j.renene.2008.11.001>.
- [5] I. Argatov, P. Rautakorpi, and R. Silvennoinen. Apparent wind load effects on the tether of a kite power generator. *Journal of Wind Engineering and Industrial Aerodynamics*, 99(10):1079–1088, 2011. doi: 10.1016/j.jweia.2011.07.010.
- [6] H. A. Bosch. Finite element analysis of a kite for power generation. Master’s thesis, Delft University of Technology, Kluyverweg 1, 2629 HS Delft, Netherlands, 4 2012.
- [7] BP. BP Statistical Review of World Energy. Technical Report June, BP P.L.C., 2016.
- [8] J. Breukels. *An Engineering Methodology for Kite Design*. PhD thesis, Delft University of Technology, 2011. URL http://repository.tudelft.nl/assets/uuid:cdece38a-1f13-47cc-b277-ed64fdda7cdf/Thesis_{_}jeroen_{_}breukels.pdf.
- [9] C2ES. Outcomes of the U.N. climate change conference in Paris. Technical report, Center for Climate and Energy Solutions, Arlington, 2015.
- [10] M. Canale, L. Fagiano, and M. Milanese. Power kites for wind energy generation: Fast predictive control of tethered airfoils. *IEEE Control Systems Magazine*, 27(6):25–38, 2007. ISSN 08880611.
- [11] A. Cherubini, A. Papini, R. Vertechy, and M. Fontana. Airborne Wind Energy Systems: A review of the technologies. *Renewable and Sustainable Energy Reviews*, 51:1461–1476, 2015. ISSN 18790690. doi: 10.1016/j.rser.2015.07.053.
- [12] S. Costello, G. Fracois, and D. Bonvin. Real-time optimization for kites. In *IFAC Proceedings Volumes (IFAC-PapersOnline)*, volume 5, pages 64–69, 2013. ISBN 9783902823380. doi: 10.3182/20130703-3-FR-4039.00004.
- [13] S. G. C. De Groot, J. Breukels, R. Schmehl, and W. J. Ockels. Modeling Kite Flight Dynamics Using a Multibody Reduction Approach. *Journal of Guidance, Control, and Dynamics*, 34(6), 2011. doi: 10.2514/1.52686. URL <http://arc.aiaa.org>.
- [14] M. Deaves. An Investigation of the Non-Linear 3D Flow Effects Relevant for Leading Edge Inflatable Kites. Master’s thesis, Delft University of Technology, Kluyverweg 1, 2629 HS Delft, Netherlands, 9 2015.

- [15] M. Diehl. Airborne Wind Energy: Basic Concepts and Physical Foundations. In *Airborne Wind Energy*, chapter 1, pages 403–25. Springer, Delft, 2013.
- [16] M. Diehl, H. G. Bock, and J. P. Schlöder. a Real-Time Iteration Scheme for Nonlinear Optimization in Optimal Feedback Control. *SIAM Journal on Control and Optimization*, 43(5):1714–1736, 2005. doi: 10.1137/s0363012902400713.
- [17] E-kite, 2013. <http://www.e-kite.com/> [Accessed: 19 January 2017].
- [18] Enerkite, 2010. <http://www.enerkite.de/en/> [Accessed: 19 January 2017].
- [19] L. Fagiano. *Control of Tethered Airfoils for High Altitude Wind Energy Generation*. PhD thesis, Politecnico di Torino, 2009.
- [20] L. Fagiano and C. Novara. Automatic crosswind flight of tethered wings for airborne wind energy: modeling, control design and experimental results. *IFAC Proceedings Volumes (IFAC-PapersOnline)*, 19(4):4927–4932, 2014. ISSN 14746670. doi: 10.1109/TCST.2013.2279592.
- [21] U. Fechner. *A Methodology for the Design of Kite-Power Control Systems*. PhD thesis, Technische Universiteit Delft, 2016.
- [22] U. Fechner, R. Van Der Vlugt, E. Schreuder, and R. Schmehl. Dynamic model of a pumping kite power system. *Renewable Energy*, 83:705–716, 2015. doi: 10.1016/j.renene.2015.04.028.
- [23] L. Fingersh, M. Hand, and A. L. Nrel. Wind Turbine Design Cost and Scaling Model. Technical Report December, National Renewable Energy Laboratory, 2006.
- [24] A. Furey and I. Harvey. *Evolution of Neural Networks for Active Control of Tethered Airfoils*, pages 746–755. Springer Berlin Heidelberg, 2007. ISBN 978-3-540-74913-4. doi: 10.1007/978-3-540-74913-4_75.
- [25] N. Geschiere. *Dynamic modelling of a flexible kite for power generation*. PhD thesis, Delft University of Technology, 2014.
- [26] G. Horn, S. Gros, and M. Diehl. *Numerical Trajectory Optimization for Airborne Wind Energy Systems Described by High Fidelity Aircraft Models*, pages 205–218. Springer Berlin Heidelberg, Berlin, Heidelberg, 2013. ISBN 978-3-642-39965-7. doi: 10.1007/978-3-642-39965-7_11. URL http://dx.doi.org/10.1007/978-3-642-39965-7_11.
- [27] B. Houska and M. Diehl. Optimal control for power generating kites. In *Proceedings of the 9th European Control Conference, Kos, Greece*, page 35603567, 2007.
- [28] IEA. Renewable Energy: Medium-Term Market Report 2016. Technical report, International Energy Agency, Paris, 2016.
- [29] A. Ilzhofer, B. Houska, and M. Diehl. Nonlinear MPC of kites under varying wind conditions for a new class of large-scale wind power generato. *International Journal of Robust and Nonlinear Control*, 17(17):1590–1599, 2007. ISSN 10498923. doi: 10.1002/rnc. URL <http://onlinelibrary.wiley.com/doi/10.1002/rnc.1553/abstract>.
- [30] IRENA. Renewable Power Generation Costs in 2014 : An Overview. Technical Report January, International Renewable Energy Agency, 2015. URL http://www.irena.org/DocumentDownloads/Publications/IRENA_{_}RE_{_}Power_{_}Costs_{_}2014_{_}report.pdf.

- [31] M. Z. Jacobson and C. L. Archer. Saturation wind power potential and its implications for wind energy. *Proceedings of the National Academy of Sciences*, 2012. doi: 10.1073/pnas.1208993109.
- [32] C. Jehle and R. Schmehl. Applied Tracking Control for Kite Power Systems. *Journal of Guidance, Control, and Dynamics*, 37(4):1–12, 2014. ISSN 0731-5090. doi: 10.2514/1.62380. URL <http://arc.aiaa.org/doi/abs/10.2514/1.62380>.
- [33] Kitegen, 2007. <http://www.kitegen.com/> [Accessed: 19 January 2017].
- [34] Kitemill, 2008. <http://www.kitemill.com/> [Accessed: 19 January 2017].
- [35] Kitepower, 2016. <http://kitepower.net/> [Accessed: 19 January 2017].
- [36] J. Lago Garcia. Periodic Optimal Control and Model Predictive Control of a Tethered Kite for Airborne Wind Energy. Master’s thesis, Delft University of Technology, Kluyverweg 1, 2629 HS Delft, Netherlands, 7 2016.
- [37] J. Langley, C. L. Archer, and K. Caldeira. Note Go, Fly a Kite: The Promises (and Perils) of Airborne Wind-Energy Systems *. *Texas Law Review*, 94(2009), 2015.
- [38] M. L. Loyd. Crosswind Kite Power. *Journal of Energy*, 4(3):106–111, 1980.
- [39] Makani, 2006. <https://x.company/makani/> [Accessed: 19 January 2017].
- [40] K. Marvel, B. Kravitt, and K. Caldeira. Geophysical limits to global wind power. *Nature Climate Change*, 3(2):118–121, 2012. ISSN 1758-678X. doi: 10.1038/nclimate1683. URL <http://dx.doi.org/10.1038/nclimate1683>.
- [41] E. Michael and S. Hans. A simple comprehensible model of tethered kite dynamics. In *Airborne Wind Energy*, chapter 8, pages 141–65. Springer, Delft, 2013.
- [42] M. Noom. *Theoretical Analysis of Mechanical Power Generation by Pumping Cycle Kite Power Systems*. Masters, Delft University of Technology, 2013.
- [43] J. Oehler. Measuring Apparent Wind Vector on a Flexible Wing Kite. Master’s thesis, University of Stuttgart, KeplerstraSse 7, 70174 Stuttgart, Germany, 5 2017.
- [44] D. Rancourt. *Method for the flight path optimization of the electric-powered reconfigurable rotor vtol concept*. PhD thesis, Georgia Institute of Technology, 2016.
- [45] REN21. Renewables 2016 Global Status Report. Technical report, REN21 Secretariat, 2016.
- [46] R. Schmehl, M. Noom, and R. van der Vlugt. Traction Power Generation with Tethered Wings. In *Airborne Wind Energy*, chapter 23, pages 23–45. Springer, Delft, 2013.
- [47] Twingtec, 2013. <http://twingtec.ch/> [Accessed: 19 January 2017].
- [48] R. van der Vlugt. Aero- and Hydrodynamic Performance Analysis of a Speed Kiteboarder. Master’s thesis, Delft University of Technology, Kluyverweg 1, 2629 HS Delft, Netherlands, 10 2009.
- [49] R. van der Vlugt, J. Peschel, and R. Schmehl. Design and Experimental Characterization of a Pumping Kite Power System. In *Airborne Wind Energy*, chapter 23, pages 403–25. Springer, Delft, 2013.
- [50] R. van der Vlugt, A. Bley, M. Noom, and R. Schmehl. Quasi-Steady Model of a Pumping Kite Power System. *ArXiv e-prints*, May 2017.

- [51] A. Wachter and L. T. Biegler. On the implementation of an interior-point filter line-search algorithm for large-scale nonlinear programming. *Mathematical Programming*, 106(1):25–57, 2006. ISSN 1436-4646. doi: 10.1007/s10107-004-0559-y. URL <http://dx.doi.org/10.1007/s10107-004-0559-y>.
- [52] P. Williams, B. Lansdorp, and W. Ockels. Modeling and Control of a Kite on a Variable Length Flexible Inelastic Tether. In *AIAA Modeling and Simulation Technologies Conference and Exhibit*, 2007. doi: 10.2514/6.2007-6705.
- [53] P. Williams, B. Lansdorp, and W. Ockels. Optimal Crosswind Towing and Power Generation with Tethered Kites. *Journal of Guidance, Control, and Dynamics*, 31(1):81–93, 2008. ISSN 0731-5090. doi: 10.2514/1.30089.
- [54] P. Williams, B. Lansdorp, R. Ruitenkamp, and W. Ockels. Modeling, Simulation, and Testing of Surf Kites for Power Generation. In *AIAA Modeling and Simulation Technologies Conference and Exhibit*, Guidance, Navigation, and Control and Co-located Conferences. American Institute of Aeronautics and Astronautics, aug 2008. doi: doi:10.2514/6.2008-6693. URL <http://dx.doi.org/10.2514/6.2008-6693>.
- [55] Windlift, 2006. <http://windlift.com/> [Accessed: 19 January 2017].
- [56] T. A. Wood, H. Hesse, A. Zraggen, and R. S. Smith. Model-Based Flight Path Planning and Tracking for Tethered Wings. In *IEEE Conference on Decision and Control*, pages 6712–6717, Osaka, Japan, Dec. 2015.
- [57] A. U. Zraggen, L. Fagiano, and M. Morari. Real-time optimization and adaptation of the crosswind flight of tethered wings for airborne wind energy. *IEEE Transactions on Control Systems Technology*, 23(2):434–448, 2015. ISSN 10636536. doi: 10.1109/TCST.2014.2332537.
- [58] A. U. Zraggen, L. Fagiano, and M. Morari. Automatic Retraction and Full-Cycle Operation for a Class of Airborne Wind Energy Generators. *IEEE Control Systems Magazine*, 24(2):594–608, 2016.